Solid-State NMR Spectroscopic Investigation of Structural and Chemical Defects in Minerals

A Dissertation Presented

by

Harris Edward Mason

to

The Graduate School

In Partial Fulfillment of the

Requirements

for the Degree of

Doctor of Philosophy

in

Geosciences

Stony Brook University

August 2009

Stony Brook University

The Graduate School

Harris Edward Mason

We the dissertation committee for the above candidate for the
Doctor of Philosophy degree, herby recommend
acceptance of this dissertation

Dr. Brian L. Phillips – Dissertation Advisor
Associate Professor, Department of Geosciences

Dr. Martin A.A. Schoonen– Chairperson of Defense
Professor, Department of Geosciences

Dr. John B. Parise
Professor, Department of Geosciences

Dr. Hanna Nekvasil
Professor, Department of Geosciences

Dr. George D. Cody
Senior Scientist, Geophysical Laboratory,
Carnegie Institution of Washington

This dissertation is accepted by the Graduate School

Lawrence Martin
Dean of the Graduate School

Abstract of the Dissertation

Solid-State NMR Spectroscopic Investigation of Structural and Chemical Defects in Minerals

by

Harris Edward Mason

Doctor of Philosophy

in

Geosciences

Stony Brook University

2009

In the laboratory the chemical and structural composition minerals can often be carefully controlled. In nature, minerals can incorporate chemical and structural defects which do not affect the overall mineralogy. It is these defects which make particular minerals or mineral groups ideal for usage in a wide variety of geochemical applications. Phosphate defects in the carbonate minerals calcite and aragonite have been studied for applications in environmental remediation and for the development of paleorainfall and paleonutrient proxies. Defect incorporation in minerals of the apatite group has implications for the stability of bones and teeth as well as for using these minerals to remediate heavy metals.

This work focuses on the analysis of mineral defects using solid-state nuclear magnetic resonance (NMR) spectroscopy. The first studies involve the investigation of phosphorous (P) incorporation into calcite speleothems and aragonitic deep-sea coral skeletons as it relates to paleo-proxy development. By tracking P paleo moisture records can be divined from calcite speleothems and paleo-nutrient record can be obtained from aragonitic coral skeletons. In both cases ^{31}P NMR spectroscopic results indicate the majority

of P incorporates as incompatible phosphate defects in the carbonate mineral lattice, but associated crystalline calcium phosphate phases are seen in each. These observations have bearing on the applicability of geochemical models based on incompatible incorporation of phosphate to the development of these paleo-proxies.

The second set of studies focuses on defect incorporation into the apatite structure. Carbonate incorporation into hydroxylapatite (HAp), and fluorapatite (FAp) is investigated and how this relates to their use in remediation stratigies. In HAp the proton bearing defects and sodium play important roles in accomdating the carbonate defects, but in FAp it is clear that F has a clearer role. Additionally, the lead containing apatite pyromorphite is also investigated due to their importance in remediation of Pb contaminated sites. These materials were studied as a function of Ca incorporation using ^{207}Pb NMR spectroscopic methods and illustrate some of the limitation of NMR spectroscopy in the study of environmentally relevant systems.

Table of Contents

List of Tables

Chapter III.

Chapter IV.

Chapter V.

List of Figures

Chapter I.

Chapter II.

Chapter III.

Chapter VI.

Chapter V.

Acknowledgements

I would like to thank…

…My advisor Dr. Brian L. Phillips for the support, guidance, insight, and patience he has given during my time at Stony Brook...
…My collaborators on the projects presented in this dissertation…
Dr. Silvia Frisia, Dr. Yuanzhi Tang, and Dr. Richard J. Reeder for their contributions to the calcite speleothem project…
…Dr. Paolo Montagna for providing coral samples and Dr. Marco Taviani and Dr. Malcolm McCulloch who also provided help on the coral project…
…Dr. Francis M. McCubbin, Dr. Alexander Smirnov, Wenquin Xu, and Dr. John Parise for their appetite for apatite…
…And the two dedicated students I had the privilege of advising as summer scholars Andrew Kozlowski, and Joshua J. Hirner…
…The reviewers both named and unnamed who provided valuable assistance in improving portions of the chapters which have been previously published…
…Andrea Illausky who helped me so much during her time at Stony Brook with her constant smile and helpful guidance…
…The Center for Environmental Molecular Science, the GAANN fellowship, and NSF which provided financial support during my graduate career…
…My labmates and the multitudes of the Grey Group both past and present that have helped me tune, pulse, or just listen to me curse the NMR…
…My friends and graduate students at Stony Brook who still laugh at my bad jokes and listen when I need help with a problem…
…All of my friends from my time at Marietta: Thanks for all your support and friendship
…My family: Without their support and love my PhD and maintained sanity would not have been possible.
…Finally, my wonderful wife Lisa who has been a source of love, kindness, and support through these last years of my PhD.

I. Introduction

1. Introduction

A mineral is a naturally occurring substance with a definite ordered arrangement of atoms, and a definite chemical composition. In the laboratory the arrangement of atoms and the chemical composition of a synthetic mineral can be carefully controlled. In nature, however, minerals can exhibit complex solid solutions and contain multiple chemical and structural defects. These properties of minerals can make studies of geochemical processes in natural systems challenging. It is also these properties that allow minerals to incorporate trace elements interesting for applications in environmental remediation, paleoclimatology, medicine, and a wide range of other applications. Therefore, it is important to understand how minerals incorporate and accommodate trace elements.

Chemical defects, structural defects, and inclusions are relevant to trace element incorporation and defined as follows for the purpose of this dissertation. A chemical defect will be defined as a minor or trace occurrence of an element or compound which does not normally occur in a mineral's stoichiometric chemical formula. A structural defect is a localized distortion of the crystal structure due to chemical defect incorporation or vacancy substitution. This type of structural defect can induce long-range changes in the crystal structure such as lengthening or contraction of unit cell dimensions without changing the overall crystal symmetry. This definition excludes macroscopic or long-range structural defects such as dislocations along crystal lattice planes. An inclusion will be defined as a macroscopic crystal impurity which occurs as an incongruity within the crystal such as an apatite grain hosted in feldspar or fluid water inclusion in calcite.

Solid-state nuclear magnetic resonance (NMR) spectroscopy provides a valuable method for investigating mineral defects present at minor to trace amounts. However, much of its past application in geosciences has been limited to the investigation of major rock forming silicates. The potential to expand its use in geosciences is significant. It can be used in many systems where defect concentrations (1 wt% or less) impede detection with methods such as X-ray diffraction (XRD) or X-ray adsorption spectroscopy (XAS). XRD provides long-range structural information and changes in mineral cell parameters as a function of defect incorporation can be investigated. The local bonding environment surrounding these defects is difficult to constrain with XRD methods. XAS can be used to provide elementally specific information on the local environment of defects, but often lacks sensitivity when observing some light elements such as P or Al. Vibrational spectroscopies such as Raman and Infrared (IR) spectroscopy can provide information about light element speciation at lower abundances. However, this technique does not discriminate amongst species or elements and spectra contain vibrational modes from all species present. The consequence being that vibrational modes often overlap hiding important spectral features. NMR spectroscopy is elementally specific, sensitive to light elements (^{1}H being the most NMR sensitive nucleus), and able to probe atomic structure on the scale of 5 Å or less allowing. These properties illustrate the suitability of NMR spectroscopic methods for defect characterization.

This dissertation focuses on solid-state NMR spectroscopic analyses of members of two different mineral groups where the incorporation of minor and trace elements is of significant geochemical importance. The first portion of the dissertation (Chapters 2 and 3) focus on the role of phosphate incorporation into the calcium carbonate minerals calcite (Chapter 2) and aragonite (Chapter 3), and the implications of the incorporated P speciation have on the development of paleo-rainfall and paleo-nutrient proxies, respectively. The second portion of the thesis (Chapters 4 – 5) focuses on the apatite group of minerals. Solid-state NMR is used to investigate how carbonate defects are accommodated in hydroxylapatite (Chapters 4) and fluorapatite (Chapter 5). Finally, a short concluding chapter (Chapter 6) focuses on the common role of H-bearing species in balancing the defects investigated in the prior chapters.

2. Substitutions Important in Representative Low-Temperature Geochemical Systems

2.1 Chemical Defects in Calcium Carbonate

2.1.1. Crystal Structures and Stability of Calcite and Aragonite

Calcite and aragonite are the two most common polymorphs of calcium carbonate. Calcite crystallizes in the rhombohedral space group, $R\bar{3}c$ (Figure 1.1). The structure is relatively simple with six-coordinate Ca ions occupying the octahedral sites in a face centered cubic lattice of carbonate carbons. The cubic symmetry is broken by the three-fold rotation of the carbonate oxygens about the carbon in alternating layers. Aragonite crystallizes in the orthorhombic space group Pmcn (Figure 1.2). Ca in this structure is in a 9 coordinate configuration, and the carbonate oxygens are bonded to three Ca instead of two as in the calcite structure. The larger cation site of the aragonite structure allows for the easier incorporation of larger cations such as Sr, Ba, and Pb. The thermodynamically stable forms at standard temperature and pressure (25 °C, 1 atm) of $SrCO_3$, $BaCO_3$, and $PbCO_3$ (strontianite, witherite, and cerussite, respectively) all have the aragonite structure whereas the thermodynamically stable forms of smaller cation carbonates such as $MgCO_3$, $ZnCO_3$, and $CdCO_3$ (magnesite, smithsonite, and otavite, respectively) all have the calcite structure.

Calcite is the thermodynamically stable phase of $CaCO_3$ at ambient surface temperatures and pressure, while aragonite is metastable. Aragonite can be precipitated from supersaturated Ca^{2+}/CO_3^{2-} solutions at higher temperatures (~60° to 100° C) and pure calcite can be transformed to aragonite at high pressures [1]. Other methods can be used to stabilize aragonite. In supersaturated solutions at ambient conditions (1 atm, 25° C), accessory cations such as Mg can be used to favor precipitation of aragonite over calcite [1]. Mg poisons the growth of calcite crystals and aragonite, which crystallizes more rapidly than calcite, will preferentially precipitate.

2.1.2 Trace Element Modeling in Calcium Carbonate

Trace element incorporation into calcium carbonate can occur through various processes, but in this dissertation coprecipitation, and surface precipitation will be considered. Coprecipitation of a trace element occurs when the trace element incorporates simultaneously with mineral precipitation. During coprecipitation, the trace element can congruently substitute for a structural component of the crystal structure, or incongruently as a chemical defect. In either case, the trace element does not form a separate crystalline phase. Surface precipitation is the process of a trace element forming a separate crystalline phase from that of the matrix mineral. A surface precipitate can be encased within the growing matrix crystal, but still retain a different mineralogy and crystal chemistry from the matrix. These processes can occur separately or in tandem during growth of the matrix crystal. Geochemical methods utilized to measure trace element concentrations in carbonates such as secondary ion mass spectrometry (SIMS) or lasar ablation inductively coupled mass spectrometry (LA-ICPMS) provide only concentration, but cannot differentiate between these two modes of trace element incorporation.

Traditional models of trace element incorporation typically assumed a simple relationship between the concentration of trace elements in solution and that of the bulk crystal. In equilibrium the incorporation of a trace element can be described using a distribution coefficient defined as:

$$K_d = \frac{c_s}{c_w} \tag{1}$$

where K_d is the distribution coefficient of the trace element, c_s is the trace element concentration in the solid, and c_w is the trace element concentration in the solution [2]. If the distribution coefficient for the system is known then the concentration of the trace element in the solid can be related directly back to its solution concentration. However, this simple model does not account for differences in K_d due to kinetic effects and numerous additional models for deriving this value for carbonates have been proposed [3].

Kinetic effects on apparent K_d values could be taken into account by applying models that explicitly consider the effects of surface adsorption, such as Watson [4]. In this model differences in the surface structure, chemistry, and trace element transport mechanisms of the host crystal with respect to the bulk are taken into consideration. The surface can have a different structure from that of the bulk, significantly affecting the surface absorption properties. The concentration of a trace element in solution and in the surface layer may also vary with respect to distance from the point at which the host crystal adopts the bulk structure and the concentration at any point can be related back to the equilibrium solution concentration through the equation:

$$c_t = c_w F^{\exp(x/l)} \tag{2}$$

where c_t is the trace element concentration in solution at a distance x from the surface, c_w is the equilibrium trace element concentration (assumed to be at an infinite distance from the surface), F is a partition coeffficent, and l is the length of the distinct surface layer. In this model trace elements absorbed and transported within the surface layer can diffuse to the bulk structure as the crystal grows.

The above models can explain coprecipitation of trace elements, but they cannot be applied to surface precipitate formation. It is difficult to constrain the amount of a trace element contained in a surface precipitate. The formation of surface precipitates depends upon nucleation and crystal growth rates which involve high kinetic barriers. The processes of coprecipitation can also occur simultaneously with surface precipitation removing trace elements from the solution. Since there is not way to differentiate between the two with bulk geochemical methods, most studies of trace element incorporation in carbonate assume that unless surface precipitate formation is blatantly present that it does not occur. This assumption may not hold in all cases and methods for differentiating between coprecipitated trace elements and surface precipitates must be developed.

2.1.3 Occurence of Phosphate in Calcium Carbonate

Various trace elements such as Ba, Sr, Mg, S, or P can occur in natural calcites and aragonites and have been studied for potential use as paleo-indicator proxies. Recent interest in the calcite/phosphate and aragonite/phosphate systems has been sparked by the potential of phosphorus contained in calcite speleothems [5-9] and aragonitic coral skeletons [10-12] to be used as paleo-rainfall and paleo-nutrient proxies. The tracing of annual growth bands define the growth rates of these samples, and the abundances of trace elements have been shown to track as a function of environmental indicators such as temperature, or pH. LA-ICPMS and SIMS can be used to measure variations in P-content of speleothems and corals in the 10 to 100 ppm range with micron to submicron resolution and correlated with time [5-7, 13, 14].

Phosphate interactions with calcite and aragonite have been extensively studied due to the role of excess-P in fresh and ocean water eutrophication. Since P is a limiting nutrient, an explosion in the growth of algae and other microorganisms occurs in the presence of excess levels of P leading to the depletion of oxygen from surface waters. With this problem as their focus, numerous geochemical studies have focused on the macroscopic uptake of phosphate by calcite and aragonite. These studies have all observed that phosphate retards the growth of calcite and aragonite [15-20]. The variation of adsorption and coprecipitation rates of phosphate with calcite and aragonite is known, and various geochemical models have been proposed that predict the P speciation in these systems [15, 20-22]. However, few studies have directly measured in what forms the P is present. Hinedi et al. [23] investigated the speciation of P sorped onto calcite samples using solid-state nuclear magnetic resonance

(NMR) techniques. The majority of P was present as phosphate incorporated in the calcite structure at low P loadings (0.002 to 1.0 P nm^{-2}). The crystalline calcium phosphate phase brushite ($CaHPO_4 \cdot 2H_2O$) was able to form at slightly higher P loadings (1.9 to 3.5 P nm^{-2}). Surface precipitates can and do form under certain conditions. For example, epitaxial precipitation of hydroxylapatite on calcite has been observed [24].

2.2. Defects and Solid Solution in Apatite Family Minerals

2.2.1. The Apatite Structure

The apatite family of minerals is characterized by a common topology accommodating a variety of both anionic and cationic defects, and allowing for extensive solid solution. The space groups adopted by minerals with the apatite structure can vary depending on the substitutions involved but the majority have the hexagonal $P6_3/m$ space group and can be described by the general chemical formula $A_5(BO_4)_3X$. A is typically a divalent cation (eg, Ca^{2+}, Pb^{2+}, Cd^{2+}), BO_4 is a trivalent oxyanion (eg. PO_4^{3-}, AsO_4^{3-}, VO_4^{3-}), and X is monovalent anion (F^-, Cl^-, OH^-). A structural representation of the apatite structure is shown in Figure 1.3. The main characteristic of the apatite structure is a large channel occupied by the X anions parallel to the c-axis. In fluorapatite, this site is fully occupied by F at the (0, 0, 0) position In hydroxylapatite and chlorapatite, this site is split, half-occupied by OH or Cl (for hydroxylapatite or chlorapatite, respectively), and slightly displaced above or below the (0, 0, 0) position. The apatite structure contains two A sites in a 2:3 ratio denoted A1 and A2 respectively. The A2 sites are arranged in alternating trigonal planes surrounding the X anion and can be 7- or 8-coordinate, bonding to 6 oxyanion oxygens and either one or two X anions in a distorted polyhedron. The A1 site lies in the middle of two alternating triangular arrangements of BO_4 tetrahedra and is 9-coordinate, bonding to 6 closest oxygens in a twisted trigonal prism and three further removed equatorial oxygens. The apatite structure is flexible and can adapt to accommodate cations and anions of varying charge and size to substitute. This property makes members of the apatite family good candidates for use in remediation strategies where they can incorporate metal cations such as Zn^{2+}, Cd^{2+}, or Pb^{2+} and polyatomic anions such as AsO_4^{3-}, CrO_4^{3-}, or VO_4^{3-}.

2.2.2. Carbonate-rich Apatite

Carbonate substitution is one of the most commonly studied anionic substitutions in apatite. Carbonate-rich apatites are important in a wide range of fields including medicine, dentistry, materials science, and geology. Carbonate apatites containing to 6 wt% carbonate are the major mineral component in bones and teeth, and carbonate fluorapatites are important for the geochemical cycling of P in marine sediments [25-27]. The carbonate content also affects reactivity and solubility when apatite is applied in remediation schemes. Since the incorporation of carbonate into apatite invokes charge and structural imbalances it is important to understand how carbonate substitution can be accommodated by the apatite structure.

There are two sites in which carbonate substitutes into the apatite structure, denoted as A and B type substitutions. Apatites can contain pure A-type, pure B-type or mixed AB-type substitutions. In A-type substitutions, carbonate substitutes for hydroxyl, or fluorine channel ions creating carbonate hydroxylapatite (CHAp) and carbonate fluorapatite (CFAp), respectively. XRD and polarized IR studies have shown that A-type carbonate orients with its plane parallel to the c-axis [28-32]. A secondary A-type substitution denoted A2-type substitution has been reported for Na-free CHAp synthesized at high temperature and pressure. In this mineral, the carbonate occupies a “stuffed” channel position where the carbonate lies closer to the edges of the apatite channel [29]. B-type substitution occurs when the carbonate replaces phosphate in the structure. In this substitution the carbonate orients with its plane slightly sub-parallel to one of the faces of the missing phosphate tetrahedron [28, 33]. Recently, an additional B-type substitution denoted “B2-type” has been observed in IR spectra of CFAp [34], but the structural role of this substitution has not been determined.

Additional substitutions and vacancies may balance both charge and structural defects in carbonate bearing apatites. In CFAp, the amount of Na, Mg, Sr, and other monovalent or divalent cations substituting for Ca provides insight into the diagenetic history of a sample [25, 27]. Substitution of monovalent cations such as Na^+ or Ca vacancies have been proposed as methods of correcting charge imbalances from carbonate substitution [35-37]. Fleet and Liu suggested that AB-type substitution can occur where carbonate substitutes into adjacent A and B sites coupled with a Na^+ substitution [35]. The incorporation of F in excess of one per formula unit (pfu) in CFAp directly correlates with B-type carbonate content. This observation led to the proposal of a tetrahedral CO_3F^{3-} complex as the substituting species, however, direct evidence is lacking. Since all these additional substitutions may be present in carbonate-rich apatites, complete understanding of carbonate substitution must include an understanding of the role of these contaminant defects.

3. Solid-State NMR Spectroscopic Methods

3.1. Basic Principles of NMR Spectroscopy

When a nucleus with a non-zero nuclear spin is placed in a static magnetic field (B_0, in practice the field generated by the superconducting magnet), the energy levels between spin states are split (Figure 1.4). For spin ½ nuclei, the splitting results in energy levels +½ and -½. The difference in energy between these levels is:

$$\Delta E = \gamma \hbar B_0 , \tag{3}$$

where γ is a property of the nucleus called the gyromagnetic ratio measured in $\mathrm{rad s^{-1} T^{-1}}$, $\hbar$ is Planck's constant divided by 2π, and B_0 is the static magnetic field in T. Using the Bohr relation:

$$\Delta E = h\upsilon = \hbar\omega , \tag{4}$$

combined with Equation 3 the equation defining the Larmor frequency (typically in the radio frequency (rf; MHz) range) can be derived.

$$\omega_0 = \gamma B_0 \tag{5}$$

The nuclei in the full system at equilibrium distribute between these levels based on the Boltzmann distribution. For example, consider a system where there is 1 mol of ^{1}H present. Using the high temperature approximation of the Boltzmann distribution the difference in population is:

$$\Delta N = N_{tot} \frac{\hbar \gamma B_0}{2k_B T} , \tag{6}$$

where ΔN is the population difference in energy levels ($\Delta N = N_{high} - N_{low}$), N_{tot} is the total population, k_B is the Boltzmann constant, and T is the temperature in Kelvin. The difference in ^{1}H populations is only 47 μmol at room temperature (25° C). Since the magnitude of this difference determines the sensitivity of the NMR experiment, the NMR experiment is much less sensitive than other spectroscopies.

When describing NMR spectroscopic experiments, the frame of reference of the physical descriptions is important. The molecular frame is simply any axis system based on the physical characteristics of the material being studied. A representative molecular frame could be based on the unit cell axes, an apex of a coordination polyhedra or an internuclear vector. In the laboratory frame (Figure 1.5A) the z-axis is parallel to B_0. In this frame, individual spins precess about B_0 at the Larmor frequency but with variable magnetic moment orientations in the plane perpendicular to the z-axis (xy-plane). The net magnetic moment of all the spins is defined as M_0, and at equilibrium M_0 will be the same as the magnetization along the z-axis (M_z). When performing an NMR experiment, rf pulses (B_1 in Figure 1.5) at or near the Larmor frequency are applied to the system. In the laboratory frame, these pulses rotate at the Larmor frequency. A rotating frame (Figure 1.5B) can be defined where the xy-plane rotates at the Larmor frequency, making B_1 appear static in this frame.

3.2. Single Pulse NMR

The fundamentals of NMR signal origination and observation can be understood by analyzing the basic single pulse (SP) NMR experiment. The sequence of applied rf pulses (pulse sequence) for the SP NMR experiment is presented in Figure 1.6. As the name implies, the most basic SP NMR experiment consists of a single short polarized rf pulse tuned to the Larmor frequency of the nucleus under observation. In the rotating frame, the applied pulse (denoted B_1) is static and can be administered along either axis in the xy-plane. This pulse causes M_0 to precess in the plane perpendicular to B_1 at the angular frequency:

$$\omega_1 = \gamma B_1 \tag{7}$$

If the following condition is met:

$$\omega_1 \cdot t_p = \frac{\pi}{2}, \tag{8}$$

where t_p is the length of the applied pulse in μs at the end of the pulse $M_y = M_0$ and the applied pulse is called a "90° pulse." Similarly, if the pulse is applied such that the solution to Equation 9 equals π this pulse is called a "180° pulse" and M_0 will reside along –z. After the "90° pulse" is turned off the individual magnetic moments (the sum of which is equal to M_0) will dephase in the xy-plane such that their sum (M_0) decays with the characteristic relaxation time T_2. Concurrently the magnetization will return to its equilibrium position along the z-axis with the characteristic relaxation time T_1. The precession of the transverse magnetization induces an oscillating current in a wire coil recorded as a function of decay time called a Free Induction Decay (FID). The FID is converted to a frequency spectrum by Fourier Transformation. This experiment is repeated and the signals co-added to improve the signal to noise ratio. In solid-state NMR the time needed to wait between additional experiments (pulse delay) is dependent upon T_1 and the length of the pulse applied.

3.3. The Chemical Shift

The most important interaction measured in the single pulse experiment is the NMR chemical shift. If an isolated nucleus is excited by an rf pulse, it will produce a signal which resonates at its Larmor frequency. However, nuclei are never isolated but surrounded by electrons, some of which interact with other electrons and neighboring atoms to form atomic bonds shielding the nuclei and changing the NMR frequency. The resulting shift in frequency away from the Larmor frequency called the chemical shift (δ) is defined as:

$$\delta = \frac{\nu_{obs} - \nu_0}{\nu_0}, \tag{9}$$

where υ_{obs} is the measured frequency of the peak, υ_0 is the Larmor frequency. The chemical shift is defined as the frequency shift of a peak with respect to a reference compound. Since the shift is typically very small, it is measured in parts per million frequency (ppm) because of the relationship in Equation 11.

$$\left(\nu_{obs} - \nu_0\right) \propto B_0 \tag{10}$$

For example, ^{31}P NMR uses 85% $H_3PO_4(aq)$ as a reference compound by assigning the single peak in its spectrum a chemical shift of 0 ppm. A ^{31}P spectrum of HAp will contain a single peak at the chemical shift of 2.65 ppm from 85% H_3PO_4. A sample where the chemical shift is known (such as HAp) can be used as a secondary chemical shift reference.

3.4 Magic Angle Spinning

The NMR spectrum of a solution typically contains sharp peaks located at the chemical shifts defined by the characteristic bonding environment of that molecule. In a solution, the free rotation of the molecule averages out interactions such as dipole - dipole coupling. In a solid, no such motional averaging typically occurs. The participation of valence electrons in bonding distorts the electron current density around the nucleus. Depending on the orientation of a bond with regard to B_0, the chemical shift can vary significantly in frequency. This variation with bond orientation is referred to as chemical shift anisotropy (CSA) and is described mathematically by a second rank tensor. Measurements of the principle vectors of the CSA can be performed on single crystals using a goniometer probe. In powders all possible orientations of a given bond with respect to B_0 may be present. The resulting spectrum of a powdered sample is a sum of the spectra arising from all possible crystallite orientations weighted according to the probability of their occurrence. The main tool used to provide higher resolution to solid-state NMR spectroscopy is magic-angle spinning (MAS). MAS is the technique where powdered samples are spun about an axis inclined 54.74° to B_0 during the acquisition of NMR spectra since it is the solution to the equation:

$$3\cos^2(\theta)-1=0 \tag{11}$$

Many NMR interactions such as dipole coupling have a $3\cos^2(\theta)-1$ dependence so MAS averages θ to 54.74° over a rotor period for any crystallite orientation. If the frequency of spinning is large compared to the CSA, the powder pattern is broken into sharp peaks spaced at the spinning frequency, and the lineshape appears more solution-like. The main peak is then located at the average trace value of the CSA tensor, and defined as the isotropic chemical shift. The isotropic peak can alternately be named the centerband and can be easily differentiated from the other peaks (spinning sidebands) since it will not change its position with changes in spinning rate.

3.5. Dipole Coupling in Solids

The detection of dipole – dipole coupling allows direct measurement of spatial proximity between NMR active nuclei. Dipole coupling arises from the interaction of two NMR-active nuclei in a static magnetic field (Figure 1.7). In this case, the total magnetic field (B(*I*)) experienced by the *I* nucleus is:

$$B(I)=B_0+B_L, \tag{12}$$

where B_0 is the static magnetic field and B_L is the local magnetic field created by the *S* nucleus. If the magnitude of B_L changes from $+B_L$ to $–B_L$, this change affects the total magnetic field experienced by *I*. The strength of B_L is given by:

$$B_L \approx \pm D(3\cos^2\theta - 1), \tag{13}$$

where *D* is the dipole coupling constant and θ is the angle between B_0 and the internuclear vector between *I* and *S*.

The total dipole coupling of the spin system (all NMR active nuclei being observed in the system i.e. all ^{1}H, all ^{31}P, or both) is broken into the coupling between nuclei of the same type (homonuclear dipole coupling) and the coupling between nuclei of differing types (heteronuclear dipole coupling). Since the NMR experiments discussed in the following sections rely on the interactions between two unlike nuclei, heteronuclear dipole coupling will be discussed. When the first-order approximations of the heteronuclear dipole coupling spin Hamiltonian are derived a coefficient called the dipole couple constant (*D*) is defined as the following:

$$D = \frac{\hbar\mu_0}{4\pi}\frac{\gamma_I\gamma_s}{r^3}, \tag{14}$$

where γ_I and γ_S are the gyromagnetic ratios of the *I* and *S* nuclei, μ_0 is the magnetic permeability of free space, and *r* is the *I* – *S* internuclear distance. *D* determines the strength of the heteronuclear dipole coupling between two spins and depends directly on r^{-3}, providing the structural information sought in the following chapters. The magnitude of *D* also depends upon the two nuclei under consideration. For example, consider a PO_4 defect substituting into the calcite at the CO_3 site. The nearest ^{13}C to ^{31}P would be approximately 4 Å and produce a ^{31}P – ^{13}C dipole coupling (D_{CP}) of 1.2 kHz. A ^{31}P – ^{1}H spin pair located at the same internuclear distance will experience a 4.8 kHz dipole coupling, and a ^{13}C – ^{15}N spin pair will experience a 0.2 kHz dipole coupling. Dipole correlations between heteronuclei not only depend upon the internuclear distances, but also on the two nuclei of interest.

3.6. NMR Methods for Measuring Dipole Coupling

As mentioned previously, most modern solid-state NMR spectroscopic experiments employ MAS as a means to achieve better spectral resolution. The process of motional averaging employed by MAS also averages out other NMR interactions, like dipole coupling.

Since dipole coupling provides the most direct distance information in a solid-state NMR experiment, methods have been determined which can measure dipole coupling while still benefiting from enhanced MAS resolution.

3.6.1. Cross Polarization

One method of exploiting the dipole coupling between heteronuclei is the cross polarization (CP) experiment. The CP/MAS NMR pulse sequence is shown in Figure 1.8. The experiment proceeds by applying a 90° excitation pulse on the indirect channel (^{1}H in Figure 1.8) and afterward applying a simultaneous "spin locking" pulse (also called the contact pulse) on the directly and indirectly observed channels. This sequence induces magnetization transfer via dipole coupling between the indirectly observed nuclei and the directly observed nuclei if their precession rates are equal ($\gamma_I B_{1,I} = \gamma_S B_{1,S}$). The spectrum is then observed in the direct dimension (^{31}P in Figure 1.8). The resulting spectrum produced by the pulse sequence in Figure 1.8 would be of the ^{31}P species associated with ^{1}H in the sample.

The relative strength of the dipole coupling constant between heteronuclei can be estimated qualitatively through analysis of the CP kinetics. Varying the length of the "spin locking" pulse (the contact time, CT) results in distinct peak intensity changes in the CP spectra (Figure 1.9). The intensity variations can be simulated using various CP kinetics models [38] where the characteristic intensity build-up and decay are fit. A review of CP experiment and associated kinetics models can be found in Kolodziejski and Klinowski [38]. While various CP kinetics models can be applied in geochemical systems, the "classical" is most relevant here. The "classical" model of CP intensity (I) as a function of time (CT) is:

$$I(t) = I_0 \left(1 - \frac{T_{IS}}{T_{1\rho}^{I}}\right)^{-1} \left[\exp\left(-\frac{CT}{T_{1\rho}^{I}}\right) - \exp\left(-\frac{CT}{T_{IS}}\right)\right] \tag{15}$$

where I_0 is the initial intensity, T_{IS} is the time constant for the magnetization exchange, and $T_{1\rho}^{I}$ is the time constant for I magnetization decay. Relaxation is from the doubly titled rotating frame, and not longitudinal relaxation. The classical model assumes that the number of I spins is much greater than the number of S spins and $T_{1\rho}^{S} >> T_{IS}, T_{1\rho}^{I}$. While these assumptions are valid for many geochemical systems, they must be reevaluated for each set of experimental conditions. The $T_{1\rho}$ decay constants are related to complex couplings between the *I* nuclei and the total lattice of nuclear spins. The T_{IS} is related to the dipole coupling between the *I* and *S* nuclei.

Under the ideal experimental conditions, T_{IS} can be used to directly estimate internuclear distances [39]. In a many-spin, rigid system the following relationship can be observed:

$$T_{IS}^{-1} \propto M_2 \propto \sum_i r_i^{-6} \tag{17}$$

where T_{IS}^{-1} is the CP rate (the inverse of T_{IS}), M_2 is the second moment of the heteronuclear dipole coupling, and r_i is the internuclear distance between the *i*th *I* and *S* nuclei. However, in most cases the system or the experimental conditions do not permit direct calculation of internuclear distances. Other interactions such as homonuclear spin-spin diffusion, homonuclear dipole coupling, and molecular scale motions can also complicate the direct use of measured T_{IS} values. Instead it is often useful to qualitatively compare T_{IS} values for multiple peaks to get a sense of the association between the two nuclei in a sample. The typical trend is the correspondence of short relative T_{IS} values with shorter relative internuclear distances and vice vesra.

3.5.2. Heteronuclear Correlation

Despite the power of CP to clearly identify the association between two nuclei such as ^{31}P with ^{1}H, this experiment lacks the ability identify with which ^{1}H the ^{31}P is most closely associated. For example, in the case of brushite ($CaHPO_4 \cdot 2H_2O$), ^{1}H magnetization can transfer from either the ^{1}H on HPO_4 or structural H_2O, but the relative contributions at each contact time are lost in the standard CP/MAS experiment. Since the bonding interactions involving H may be critical to mineral reactivity and stability, a method for determining which ^{1}H species is closely associated with the directly detected nucleus is desirable.

The NMR experiment best suited for these types of analyses is heteronuclear correlation (HetCor) spectroscopy. For the purpose of the following discussion, the indirectly detected nucleus is ^{1}H and the directly observed nucleus is ^{31}P (other nuclei can be easily substituted in both discussion and experimentation). The simplest HetCor pulse sequence (Figure 1.10) is a modification of the CP/MAS pulse sequence with the inclusion of an incremented delay *t1* after the 90° pulse on the ^{1}H channel. Since the 90° pulse moves the ^{1}H magnetization to the transverse plane the effect of the *t1* delay is to allow the ^{1}H magnetization to evolve according to the chemical shifts in this plane before the magnetization is transferred to ^{31}P through the CP contact pulse. The experiment is 2-dimenisonal in the sense that spectra are collected for a series of *t1* delay times. Time is encoded in two dimensions, the increment *t1* and the acquisitions time *t2*. HetCor produces individual ^{31}P spectra whose intensity modulations with *t1* map FIDs in the ^{1}H dimension at each subsequent point in the ^{31}P dimension. These FIDs can then be Fourier transformed to produce ^{1}H spectra that correlate to points in the ^{31}P spectra. The resulting contour plots show the degree of correlation between ^{1}H and ^{31}P species (Figure 1.11).

Alternately, modifying the HetCor pulse sequence by adding two additional 90° pulses will increase ^{1}H spin-spin diffusion (Figure 1.12). The addition of a -90° pulse after the incremented *t1* period moves the magnetization from the transverse plane back along the z-axis. The following t_{mix} is a set delay period where ^{1}H magnetization diffuses to a bulk ^{1}H reservoir which may or may not be coupled directly to ^{31}P. The second 90° pulse immediately before the contact time shifts the magnetization to the transverse plane where it can then be transferred to ^{31}P during the CP contact pulse. In certain cases, the CP kinetics of ^{1}H species can be affected by magnetization loss from spin-spin diffusion, which can be detected by this experiment. In the absence of homonuclear ^{1}H decoupling during *t1*, spin diffusion can occur among ^{1}H, so that cross peaks can be observed not only from the H directly coupled to P, but from other H in contact by spin diffusion as well.

3.5.3. Rotational Echo Double Resonance

The CP/MAS and HetCor NMR experiments rely upon dipole coupling between the two nuclei to mediate the transfer of magnetization yielding qualitative proximity information. However, other influences such as spin-spin diffusion, homonuclear coupling, and oscillatory or "non-classical" CP kinetics can prevent quantitative derivation of internuclear distances (except in the case of isolated spin pairs). Therefore, another NMR tool which relies on the heteronuclear dipole coupling between two heteronuclei, but not affected by such phenomena is necessary.

Investigating the close proximity of two heteronuclei and the dipole coupling between them is possible with the rotational echo double resonance (REDOR) NMR experiment. The REDOR experiment consists of two separate NMR experiments as showed in Figure 1.13. The first is a standard spin-echo (a 90° pulse followed by a delay and then a 180° pulse) on the observe channel (Figure 1.13A). In the second, the same spin-echo is applied on the observe channel, but a series of 180° pulses are applied on the indirect channel (Figure 1.13B). The sequences are "rotor synchronized" where the time between the 90° and 180° pulses on the observe channel must be an integer multiple (n) of the rotor period (τ_{rot}). This synchronization is necessary because MAS averages heteronuclear dipole coupling to zero over the rotor period. The evolution of the local magnetic field at the ^{1}H nucleus arising from dipole coupling to ^{31}P ($B_{L,H}$) is illustrated in the bottom panel of Figure 1.13A. The field experienced by the ^{1}H crosses through zero at every half rotor period and returns to zero by the end of the spin-echo experiment. By placing 180° pulses on the ^{31}P channel at the half rotor periods (Figure 1.13B), the $B_{L,\ H}$ is inverted, and the effect of dipole coupling is reversed. The disparity in the average local field before and after the ^{1}H 180° pulse results in incomplete refocusing of the ^{1}H spin-echo (dephasing) and a reduction in signal intensity that depends on the length of the experiment (dephasing time) and the magnitude of the dipole coupling.

The REDOR experiment involves the collection of two separate spectra. In the example presented in Figure 1.13, the first is a ^{1}H spin-echo (S_0) with no pulses applied on the ^{31}P channel which produces a spectrum where all ^{1}H species are represented. The second spectrum (S) is the $^{1}H\{^{31}P\}$ REDOR spectrum where any ^{1}H peaks associated with ^{31}P are reduced in intensity. A difference spectrum (S_0-S) shows only the ^{1}H peaks associated with ^{31}P.

Similar to CP/MAS, a series of REDOR spectral sets can be collected where the number of rotor periods (dephasing time) is increased or decreased, and the resulting REDOR fractions ($(S_0-S)/S$) can be plotted as function of dephasing time. The variation of the REDOR fraction can be fit using dipole coupling models to derive quantitative information on internuclear distances. Curves produced by isolated pairs of heteronuclei are the simplest to fit and interpret. Software packages such as SIMPSON [40] can be used to simulate and fit REDOR curves. Figure 1.14 shows a typical REDOR dephasing curve calculated for a ^{13}C – ^{31}P spin pair at an internuclear distance of 4 Å. However, systems in geochemistry often involve dipole interactions between many spin pairs. Data for multiple spin pairs are easily interpreted if the different pairs have different chemical shifts, but many sources may contribute to the total dipole coupling of a single peak. Bertmer and Eckert [41] presented a series of "multi-spin" approximations, which fit the initial increase of the REDOR curve well and can be used to extract the average dipole coupling for the entire system.

4. Summary of the Chapters

This dissertation focuses on systems where minor substitutions in minerals are critical to the understanding of the underlying geochemistry. Chapters 2 and 3 investigate the incorporation of phosphate defects into natural and synthetic samples of calcite and aragonite. In Chapter 2, the incorporation of phosphate in calcite speleothems is studied to examine P content as a potential paleorainfall proxy [2-4]. An unidentified crystalline calcium phosphate phase and monetite ($CaHPO_4$) are identified in calcite speleothems as well as occluded inorganic phosphate defects in calcite. In Chapter 3, deep sea coral skeletal aragonite P content is investigated. In this system, P content is used in the development of a paleonutrient proxy for ocean environments [10]. The NMR data show that majority of P is present as occluded inorganic phosphate in aragonite, but in some samples, crystalline hydroxylapatite can occur. Both studies explore the implications of the determined speciation as they relate to the geochemistry of paleorainfall and paleonutrient proxies. Since the incorporation of crystalline inclusions into these minerals is not well understood, careful screening of samples before applying these proxies is advocated.

Chapters 4 and 5 examine carbonate-rich apatites to understand the chemical and structural basis for carbonate accommodation in hydroxylapatite and fluorapatite. Several compensation schemes have been developed explaining carbonate incorporation in these systems. In Chapter 4, investigation of CHAp identifies charge and structural compensation of carbonate ions as coupled A and B-type substitution of hydrogen carbonate ions with Na^+. Chapter 5 investigates a natural CFAp and the different compensation roles of F and H in carbonate substitution. This study shows that an extra peak occurs in the ^{19}F spectrum, which is not associated with differences in ^1H or ^{31}P dipole coupling, but correlates with the amount of F in excess of 1 per formula unit. Additionally, structural water is identified and shown to serve a role in balancing structural defects resulting from carbonate substitution.

Chapter 6 presents a brief summary of the results presented in the previous chapters and discusses the apparent importance that H-bearing species play in accommodating all the defect substitutions studied. In the studied systems H-bearing species are all important in the charge and structural balancing of chemical and structural defects. Using double resonance NMR spectroscopic techniques yields data on chemical and structural defects in these systems unobtainable with XRD and vibrational spectroscopic techniques alone. In particular, it is shown that double resonance methods are instrumental in identifying the types of hydrogen environments associated with the defect and the strength of hydrogen bonding.

This dissertation focuses on the application of double resonance solid-state NMR spectroscopic methods to the study of substitution phenomena in minerals. The studies differ significantly in the mineralogy and types of specimens investigated, but all illustrate the efficacy of NMR methods at determining the local chemistry and structure of minor and trace defects. Exploiting dipole coupling between nuclei allows investigation of the relative proximity of nuclei such as ^{31}P, ^{13}C, ^{1}H, and ^{19}F. This work demonstrates how to extend these techniques to natural and synthetic geochemical systems of varying complexity.

5. References

[1] F. Lippmann, Sedimentary carbonate minerals, Springer-Verlag, Berlin, New York,, 1973, vi, 228 p. pp.

[2] W. Stumm, L. Sigg, B. Sulzberger, Chemistry of the solid-water interface : processes at the mineral-water and particle-water interface in natural systems, Wiley, New York, 1992, x, 428 p. pp.

[3] J.D. Rimstidt, A. Balog, J. Webb, Distribution of trace elements between carbonate minerals and aqueous solutions, Geochimica Et Cosmochimica Acta 62(1998) 1851-1863.

[4] E.B. Watson, A conceptual model for near-surface kinetic controls on the trace-element and stable isotope composition of abiogenic calcite crystals, Geochimica Et Cosmochimica Acta 68(2004) 1473-1488.

[5] J.U.L. Baldini, F. McDermott, I.J. Fairchild, Structure of the 8200-year cold event revealed by a speleothem trace element record, Science 296(2002) 2203-2206.

[6] I.J. Fairchild, A. Baker, A. Borsato, S. Frisia, R.W. Hinton, F. McDermott, A.F. Tooth, Annual to sub-annual resolution of multiple trace-element trends in speleothems, Journal of the Geological Society 158(2001) 831-841.

[7] H.M. Huang, I.J. Fairchild, A. Borsato, S. Frisia, N.J. Cassidy, F. McDermott, C.J. Hawkesworth, Seasonal variations in Sr, Mg and P in modern speleothems (Grotta di Ernesto, Italy), Chemical Geology 175(2001) 429-448.

[8] P.C. Treble, J. Chappell, J.M.G. Shelley, Complex speleothem growth processes revealed by trace element mapping and scanning electron microscopy of annual layers, Geochimica Et Cosmochimica Acta 69(2005) 4855-4863.

[9] P.C. Treble, J.M.G. Shelley, J. Chappell, Comparison of high resolution sub-annual records of trace elements in a modern (1911-1992) speleothem with instrumental climate data from southwest Australia, Earth and Planetary Science Letters 216(2003) 141-153.

[10] P. Montagna, M. McCulloch, M. Taviani, C. Mazzoli, B. Vendrell, Phosphorus in cold-water corals as a proxy for seawater nutrient chemistry, Science 312(2006) 1788-1791.

[11] M. LaVinge, M.P. Field, E. Anagnostou, A.G. Grottoli, G.M. Wellington, R.M. Sherrell, Skeletal P/Ca tracks upwelling in Gulf of Panama coral: Evidence for a new seawater phosphate proxy, Geophysical Research Letters 35(2008) L05604.

[12] E. Anagnostou, R.M. Sherrell, J.F. Adkins, A.C. Gagnon, Phosphorus, barium and boron in the deep-sea coral Desmophyllum dianthus: Preliminary calibrations, Geochimica Et Cosmochimica Acta 71(2007) A22.

[13] I.J. Fairchild, A. Borsato, A.F. Tooth, S. Frisia, C.J. Hawkesworth, Y.M. Huang, F. McDermott, B. Spiro, Controls on trace element (Sr-Mg) compositions of carbonate cave waters: implications for speleothem climatic records, Chemical Geology 166(2000) 255-269.

[14] S. Frisia, A. Borsato, I.J. Fairchild, J. Susini, Variations in atmospheric sulphate recorded in stalagmites by synchrotron micro-XU and XANES analyses, Earth and Planetary Science Letters 235(2005) 729-740.

[15] A. Mucci, Growth-Kinetics and Composition of Magnesian Calcite Overgrowths Precipitated from Seawater - Quantitative Influence of Ortho-Phosphate Ions, Geochimica Et Cosmochimica Acta 50(1986) 2255-2265.
[16] J. deKanel, J.W. Morse, Chemistry of Ortho-Phosphate Uptake from Seawater on to Calcite and Aragonite, Geochimica Et Cosmochimica Acta 42(1978) 1335-1340.
[17] F. Millero, F. Huang, X.R. Zhu, X.W. Liu, J.Z. Zhang, Adsorption and desorption of phosphate on calcite and aragonite in seawater, Aquatic Geochemistry 7(2001) 33-56.
[18] R.J. Reeder, M. Nugent, G.M. Lamble, C.D. Tait, D.E. Morris, Uranyl incorporation into calcite and aragonite: XAFS and luminescence studies, Environmental Science & Technology 34(2000) 638-644.
[19] M.M. Reddy, Crystallization of Calcium-Carbonate in Presence of Trace Concentrations of Phosphorus-Containing Anions .1. Inhibition by Phosphate and Glycerophosphate Ions at pH 8.8 and 25ºC, Journal of Crystal Growth 41(1977) 287-295.
[20] W.A. House, Inhibition of Calcite Crystal-Growth by Inorganic-Phosphate, Journal of Colloid and Interface Science 119(1987) 505-511.
[21] W.A. House, L. Donaldson, Adsorption and Coprecipitation of Phosphate on Calcite, Journal of Colloid and Interface Science 112(1986) 309-324.
[22] D.J. Sinclair, M.J. Risk, A numerical model of trace-element coprecipitation in a physicochemical calcification system: Application to coral biomineralization and trace-element 'vital effects', Geochimica Et Cosmochimica Acta 70(2006) 3855-3868.
[23] Z.R. Hinedi, S. Goldberg, A.C. Chang, J.P. Yesinowski, A P-31 and H-1 MAS NMR-Study of Phosphate Sorption onto Calcium-Carbonate, Journal of Colloid and Interface Science 152(1992) 141-160.
[24] P.G. Koutsoukos, G.H. Nancollas, Crystal-Growth of Calcium Phosphates - Epitaxial Considerations, Journal of Crystal Growth 53(1981) 10-19.
[25] J.M. McArthur, Francolite Geochemistry - Compositional Controls during Formation, Diagenesis, Metamorphism and Weathering, Geochimica Et Cosmochimica Acta 49(1985) 23-35.
[26] G.H. McClellan, J.R. Lehr, Crystal Chemical Investigation of Natural Apatites, American Mineralogist 54(1969) 1374-&.
[27] J.D. Schuffert, M. Kastner, G. Emanuele, R.A. Jahnke, Carbonate-Ion Substitution in Francolite - a New Equation, Geochimica Et Cosmochimica Acta 54(1990) 2323-2328.
[28] Y. Suetsugu, I. Shimoya, J. Tanaka, Configuration of carbonate ions in apatite structure determined by polarized infrared spectroscopy, Journal of the American Ceramic Society 81(1998) 746-748.
[29] M.E. Fleet, X.Y. Liu, Carbonate apatite type A synthesized at high pressure: new space group (P(3)over-bar) and orientation of channel carbonate ion, Journal of Solid State Chemistry 174(2003) 412-417.
[30] M.E. Fleet, X.Y. Liu, P.L. King, Accommodation of the carbonate ion in apatite: An FTIR and X-ray structure study of crystals synthesized at 2-4 GPa, American Mineralogist 89(2004) 1422-1432.
[31] R.M. Wilson, S.E.P. Dowker, J.C. Elliott, Rietveld refinements and spectroscopic structural studies of a Na-free carbonate apatite made by hydrolysis of monetite, Biomaterials 27(2006) 4682-4692.

[32] R.M. Wilson, J.C. Elliott, S.E.P. Dowker, R.I. Smith, Rietveld structure refinement of precipitated carbonate apatite using neutron diffraction data, Biomaterials 25(2004) 2205-2213.

[33] M.E. Fleet, X.Y. Liu, Location of type B carbonate ion in type A-B carbonate apatite synthesized at high pressure, Journal of Solid State Chemistry 177(2004) 3174-3182.

[34] M.E. Fleet, Infrared spectra of carbonate apatites: v(2)-Region bands, Biomaterials 30(2009) 1473-1481.

[35] M.E. Fleet, X. Liu, Coupled substitution of type A and B carbonate in sodium-bearing apatite, Biomaterials 28(2007) 916-926.

[36] S.M. Nokhrin, Y. Pan, M.J. Nilges, Electron paramagnetic resonance spectroscopic study of carbonate-bearing fluorapatite: New defect centers and constraints on the incorporation of carbonate ions in apatites, American Mineralogist 91(2006) 1425-1431.

[37] R. Astala, M.J. Stott, First principles investigation of mineral component of bone: CO_3 substitutions in hydroxyapatite, Chemistry of Materials 17(2005) 4125-4133.

[38] W. Kolodziejski, J. Klinowski, Kinetics of cross-polarization in solid-state NMR: A guide for chemists, Chemical Reviews 102(2002) 613-628.

[39] J. Feng, Y. Lee, J.D. Kubicki, R.J. Reeder, B.L. Phillips, NMR Spectroscopy of Citrate in Solids: Cross-Polarization Kinetics in Weakly Coupled Systems, Magnetic Resonance in Chemistry 46(2008) 408-417.

[40] M. Bak, J.T. Rasmussen, N.C. Nielsen, SIMPSON: A general simulation program for solid-state NMR spectroscopy, Journal of Magnetic Resonance 147(2000) 296-330.

[41] M. Bertmer, H. Eckert, Dephasing of spin echoes by multiple heteronuclear dipolar interactions in rotational echo double resonance NMR experiments, Solid State Nuclear Magnetic Resonance 15(1999) 139-152.

6. Figures and Captions

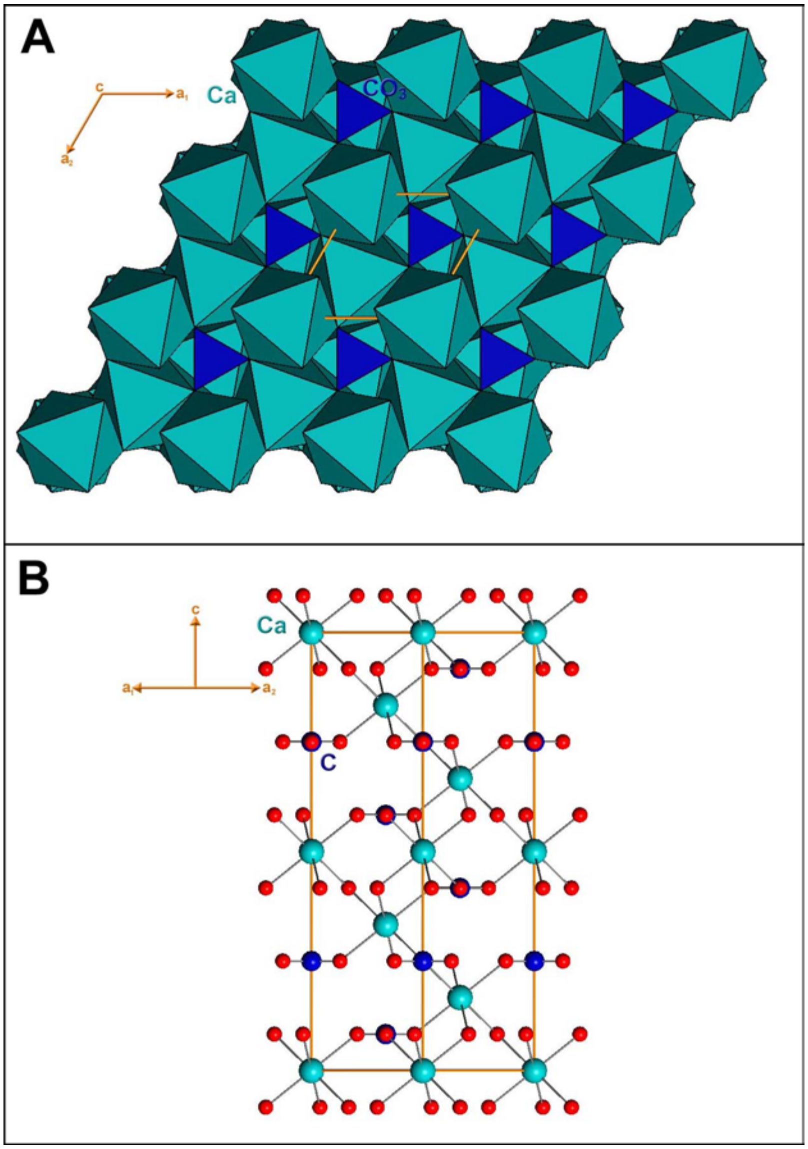

Figure 1.1. Structural representations of the calcite structure represented in the hexagonal unit cell. **A**. Polyhedral representation viewed along the c-axis, and **B.** Ball and stick representation viewed midway between the a-axes. Orange boxes represent the outline of the unit cell.

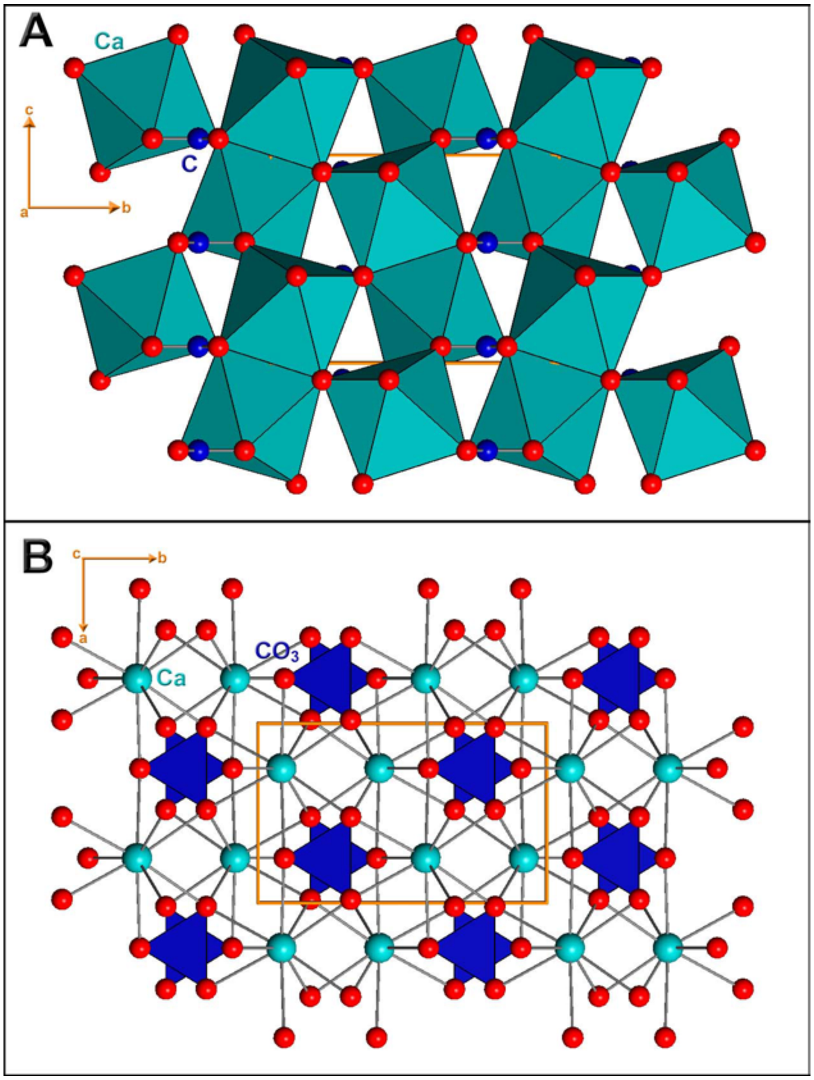

Figure 1.2. Structural representations of the aragonite crystal structure. A. Structure viewed along the a-axis. Ca are represented as polyhedra and carbons are represented as spheres to emphasize their arrangement. B. Structure viewed along the c-axis. Ca polyhedra are represented as balls and sticks to emphasize the bonding environment. CO3 is represented as polyhedra. Orange boxes outline the unit cell.

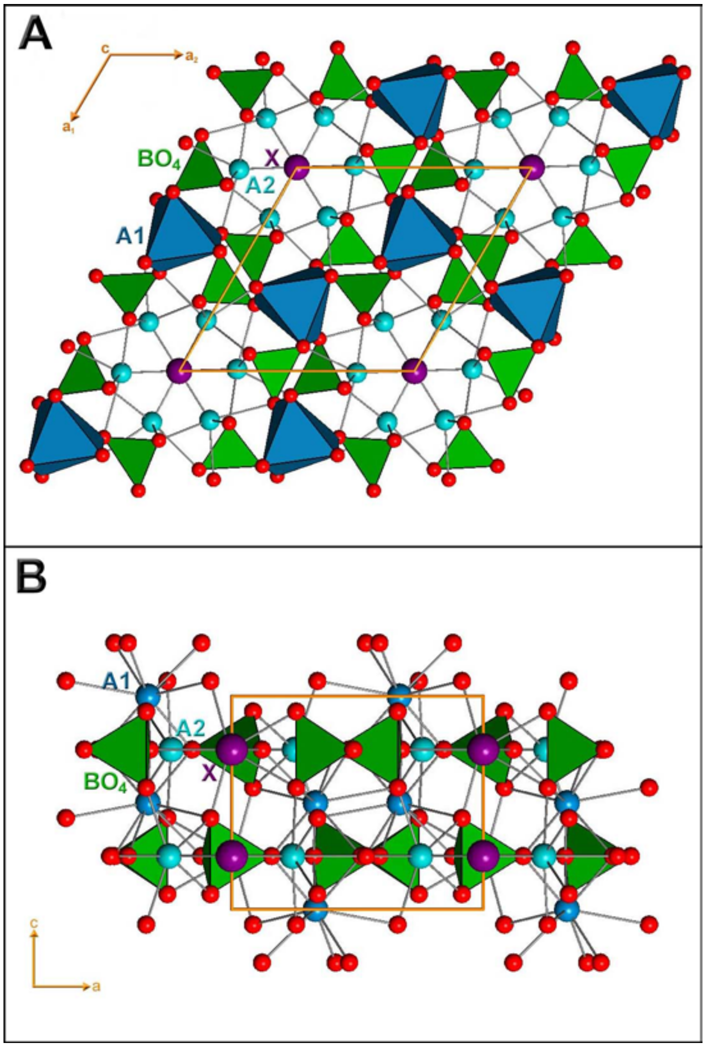

Figure 1.3. Structural representations of the apatite structure. **A**. Structure viewed along the c-axis, A1 site is represented as a polyhedra containing only the six nearest oxygens to emphasize the metaprism twist. B. Structure viewed along the a-axis. The A1 site is represented by ball and stick model to emphasis the bonding environment. Orange boxes outline the unit cell.

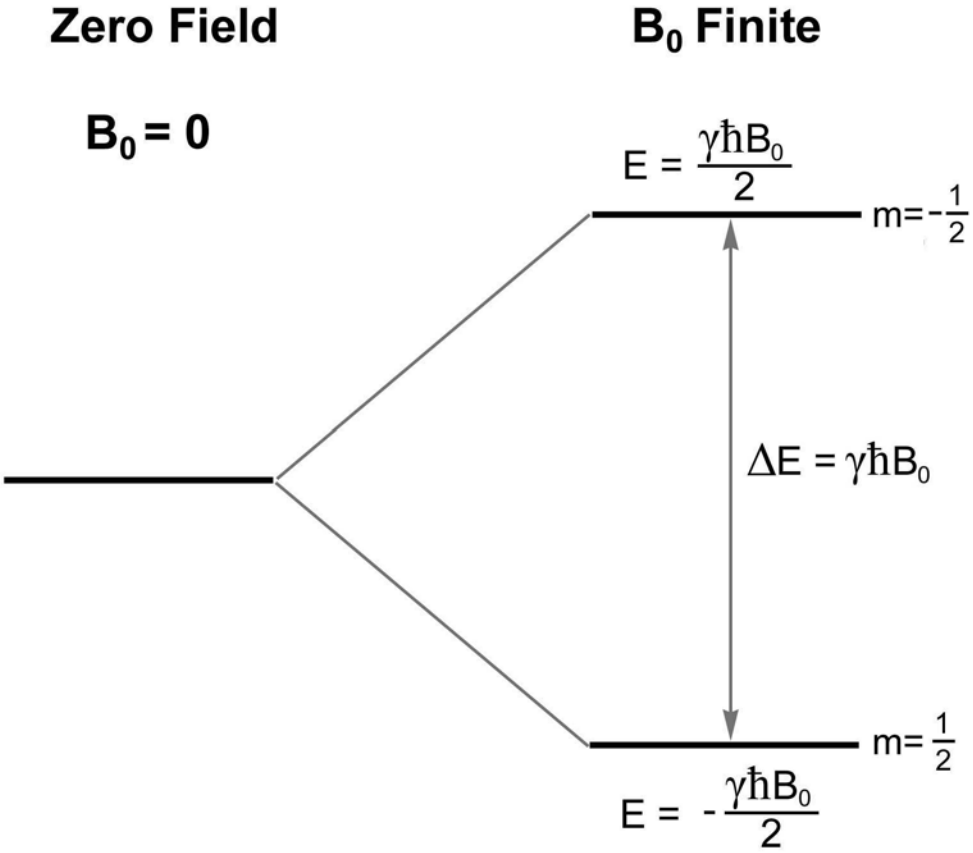

Figure 1.4. Energy level diagram illustrating the splitting of energies that occurs when an *I* = ½ nuclei is placed in a static magnetic field (B_0).

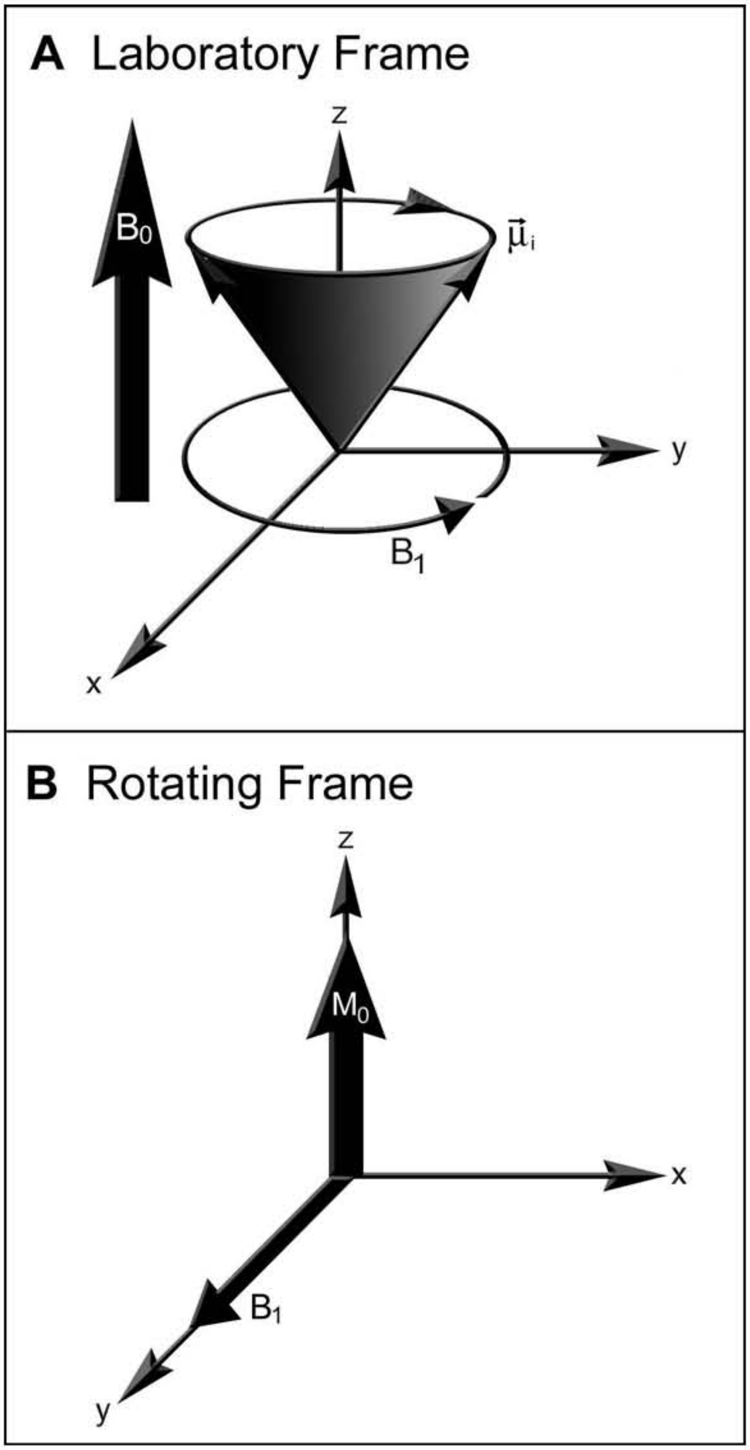

Figure 1.5. Schematic representations of A.the laboratory, and B rotating reference frames used for describing NMR spectroscopic experiments.

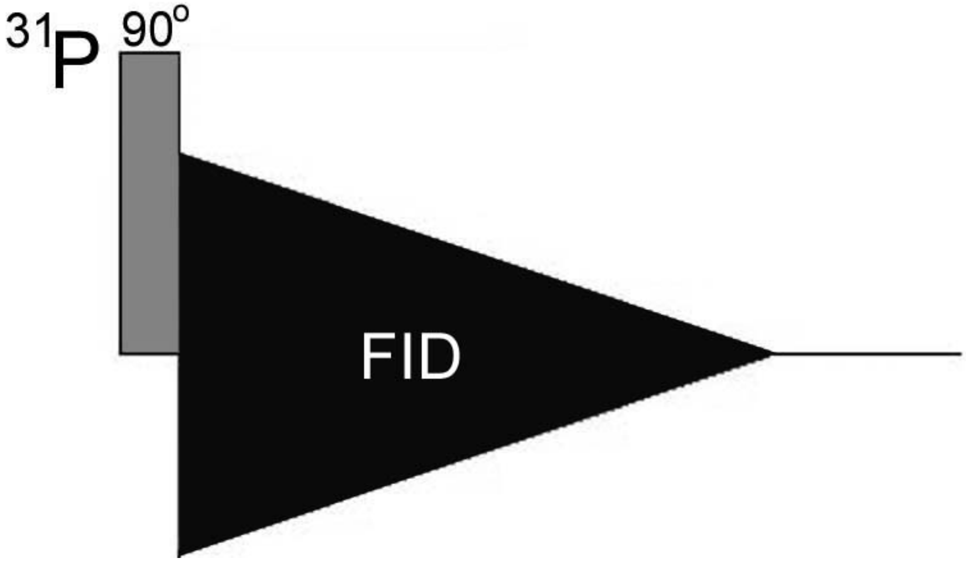

Figure 1.6. Standard pulse sequence depicting a ^{31}P single-pulse NMR experiment.

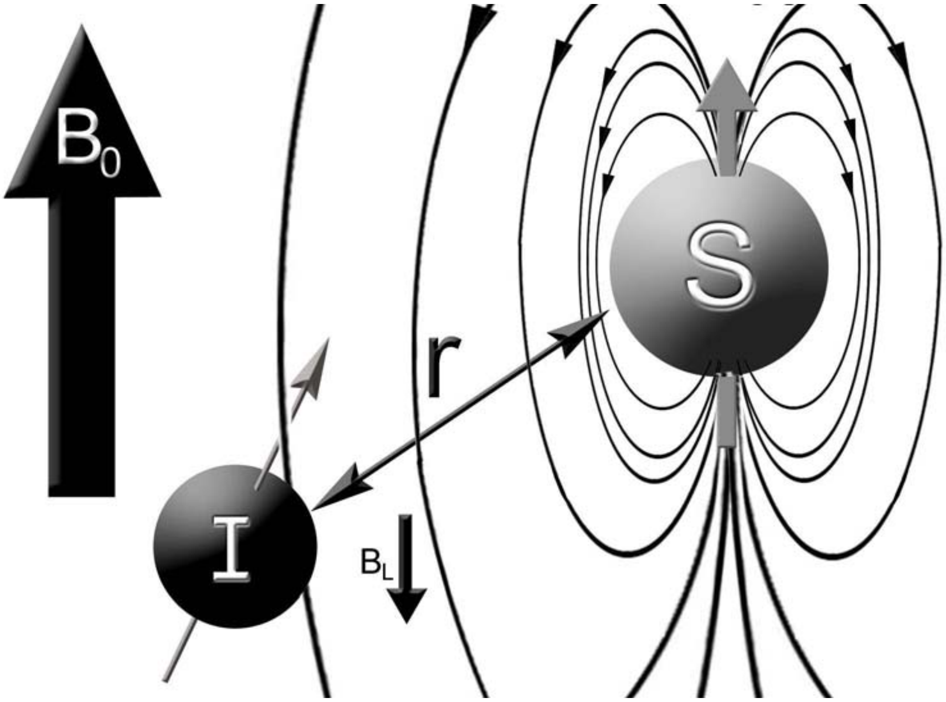

Figure 1.7. Schematic representation of dipole coupling between two nuclei *I* and *S* which in this case are two spin ½ nuclei. Arrow labeled B_0 represents the orientation of the static magnetic field, arrow protruding from the *I* and *S* nucleus represents their magnetic moments, lines surrounding the *S* nucleus represent the magnetic field produced by the *S* nucleus, B_L is the local field generated by *S* which *I* experiences, and *r* is the internuclear distance between the *I* and *S* nuclei.

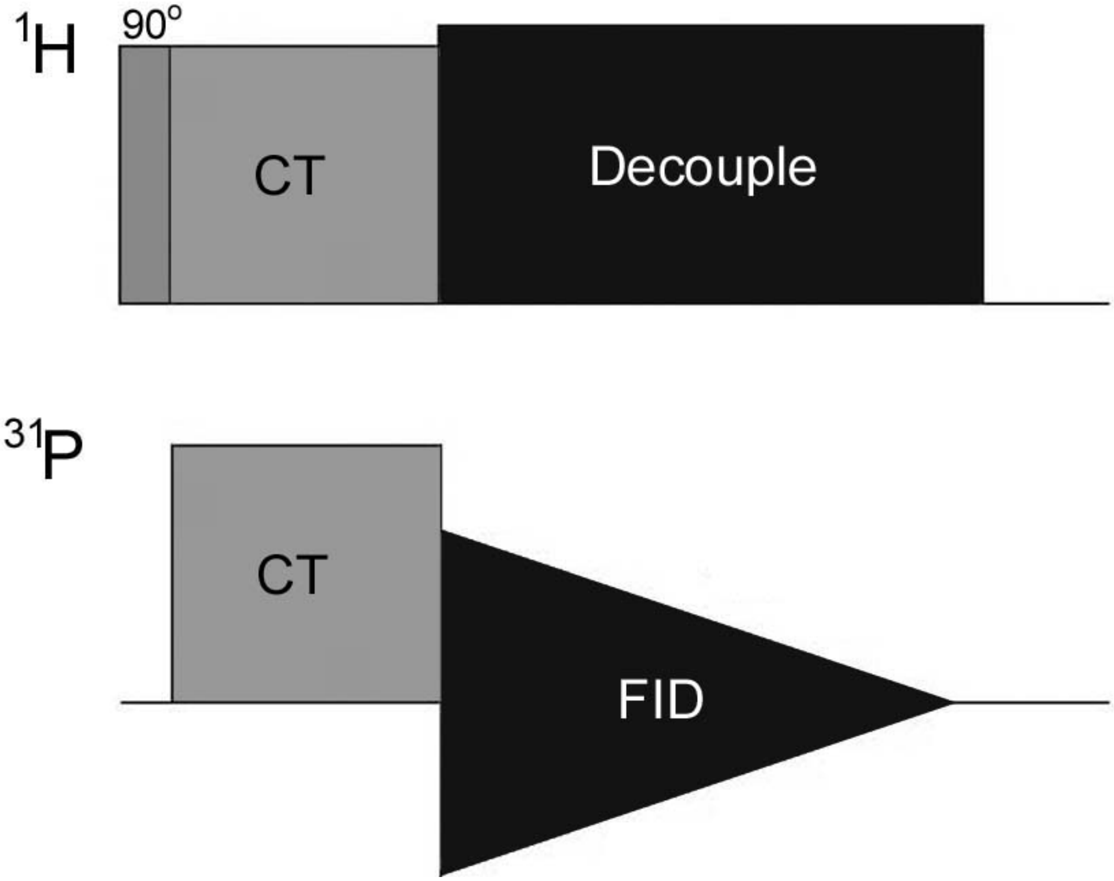

Figure 1.8. Standard Pulse sequence depicting a $^{31}P\{^{1}H\}$ CP/MAS NMR experiment.

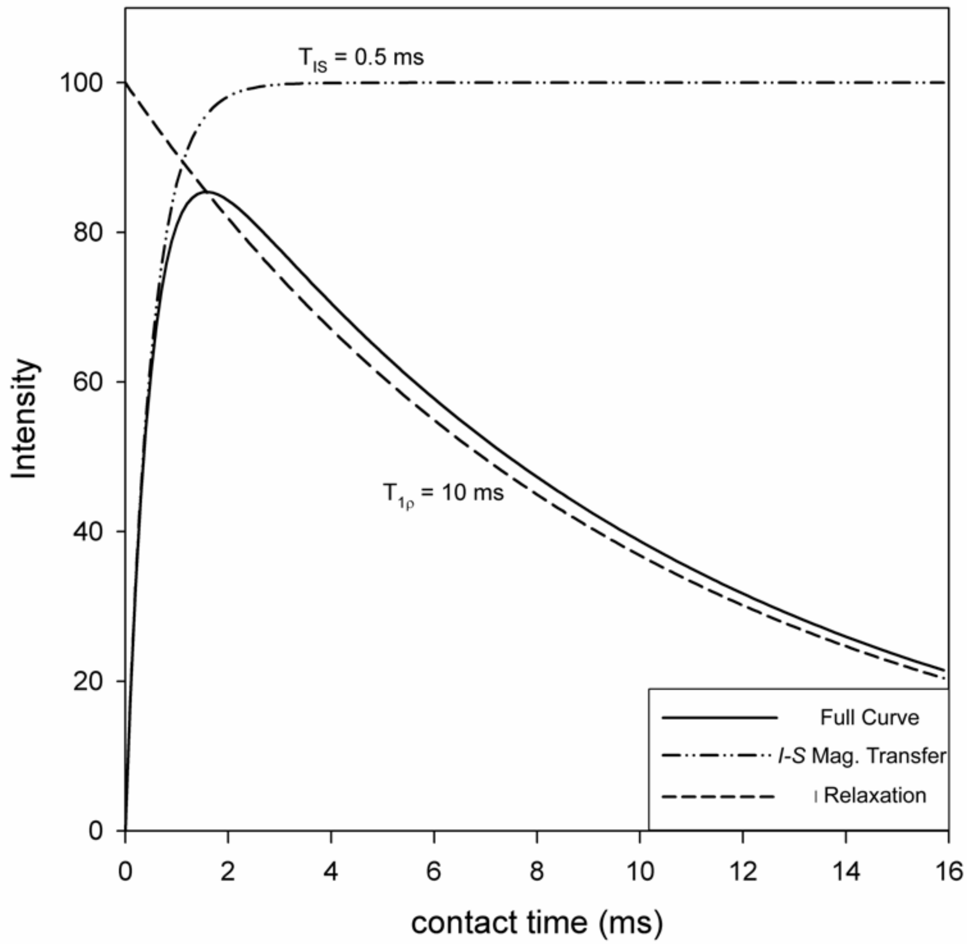

Figure 1.9. Simulated CP kinetics curve using the "classical" model. Shown with the individual T_{IS} and $T_{1\rho}$ curves. T_{IS} = 0.5 ms, $T_{1\rho}$ = 10 ms.

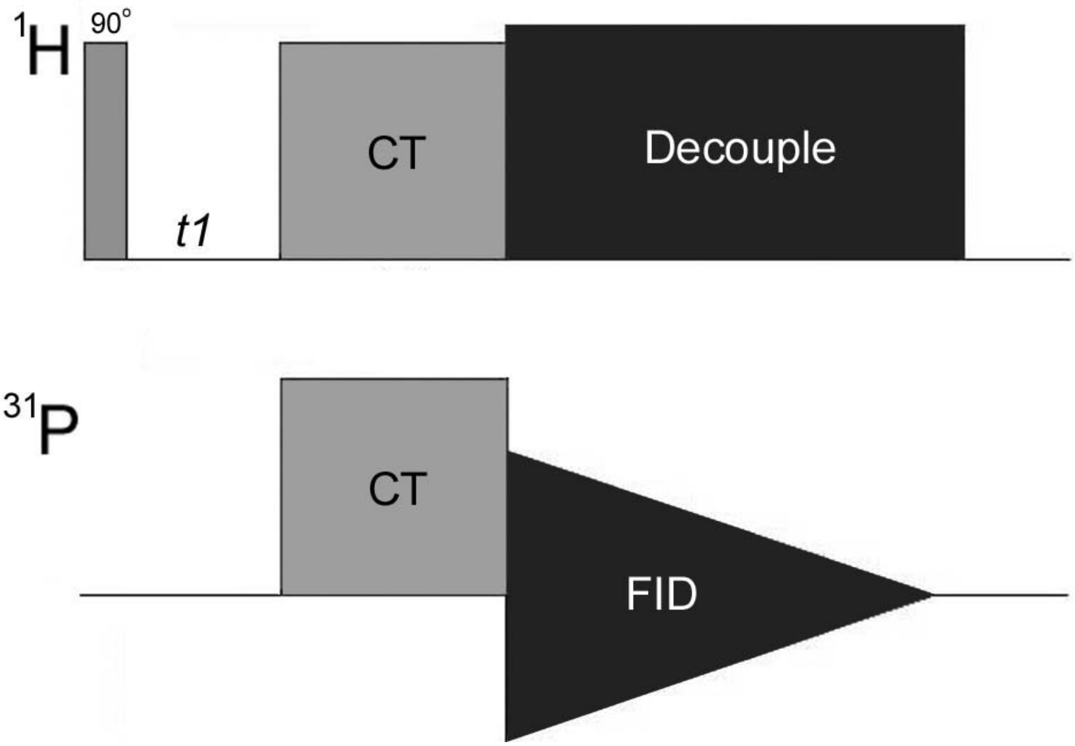

Figure 1.10. Standard Pulse sequence depicting a ^{31}P{^{1}H} HetCor experiment.

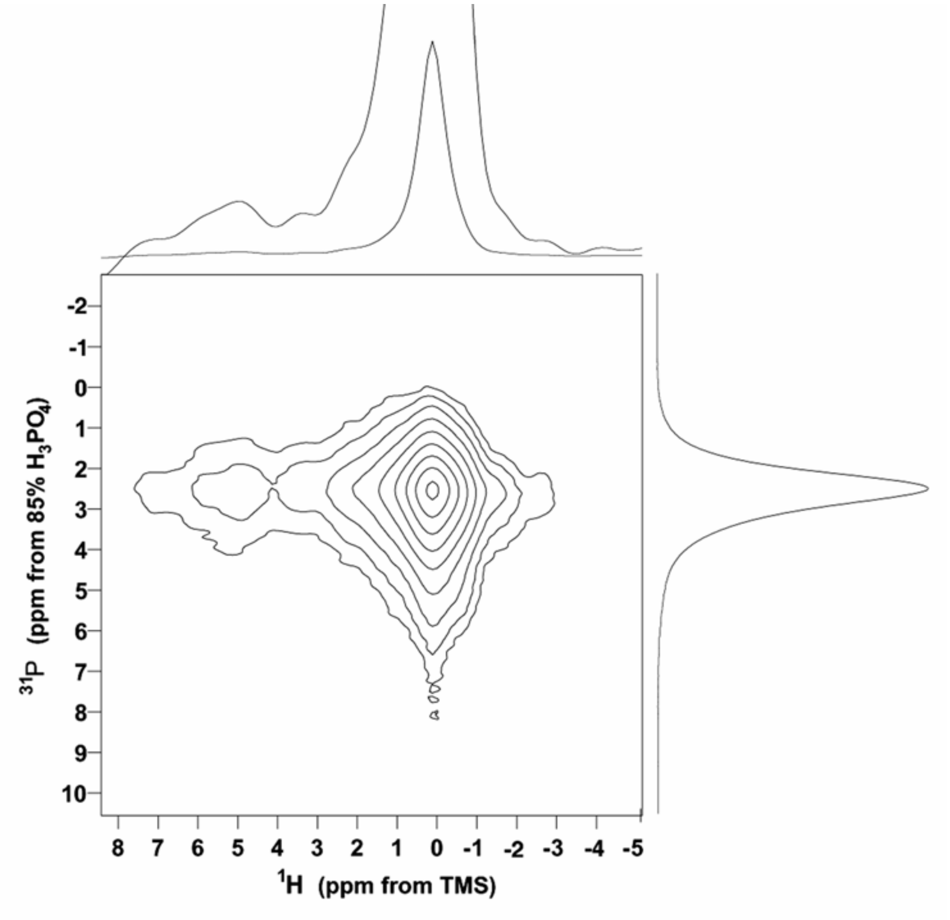

Figure 1.11. ^{31}P{^{1}H} HetCor contour map for a sample of carbonate apatite. ^{1}H summed projection is shown along the top horizonatal axis, and ^{31}P summed projection is shown along the right most vertical axis.

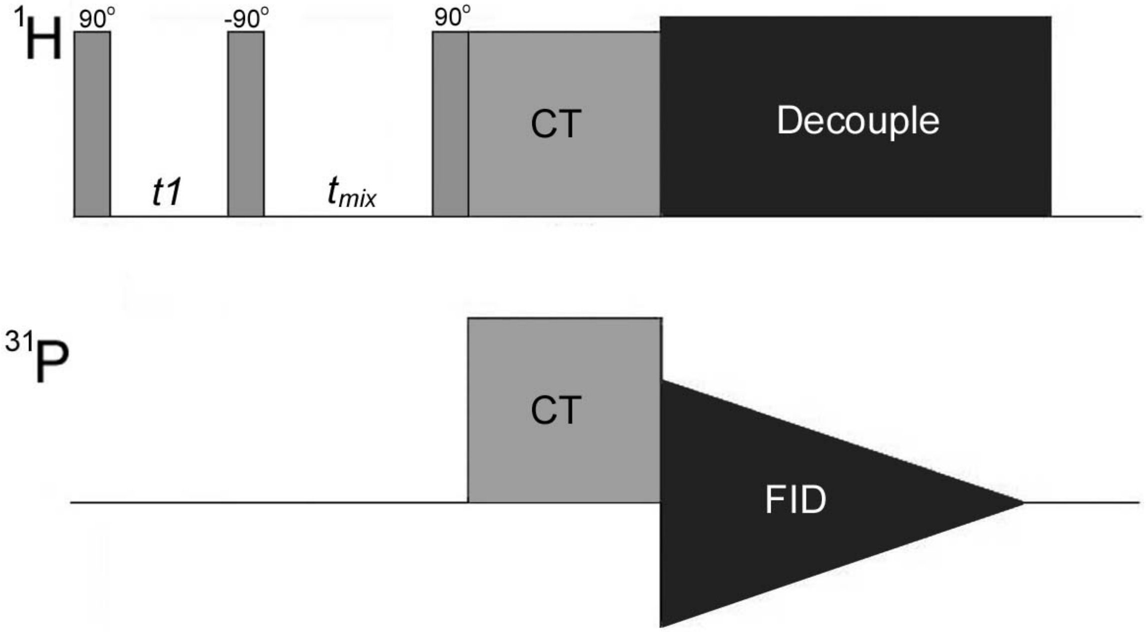

Figure 1.12. Standard pulse sequence depicting the ^{1}H{^{31}P} HetCor experiment with ^{1}H mixing time added.

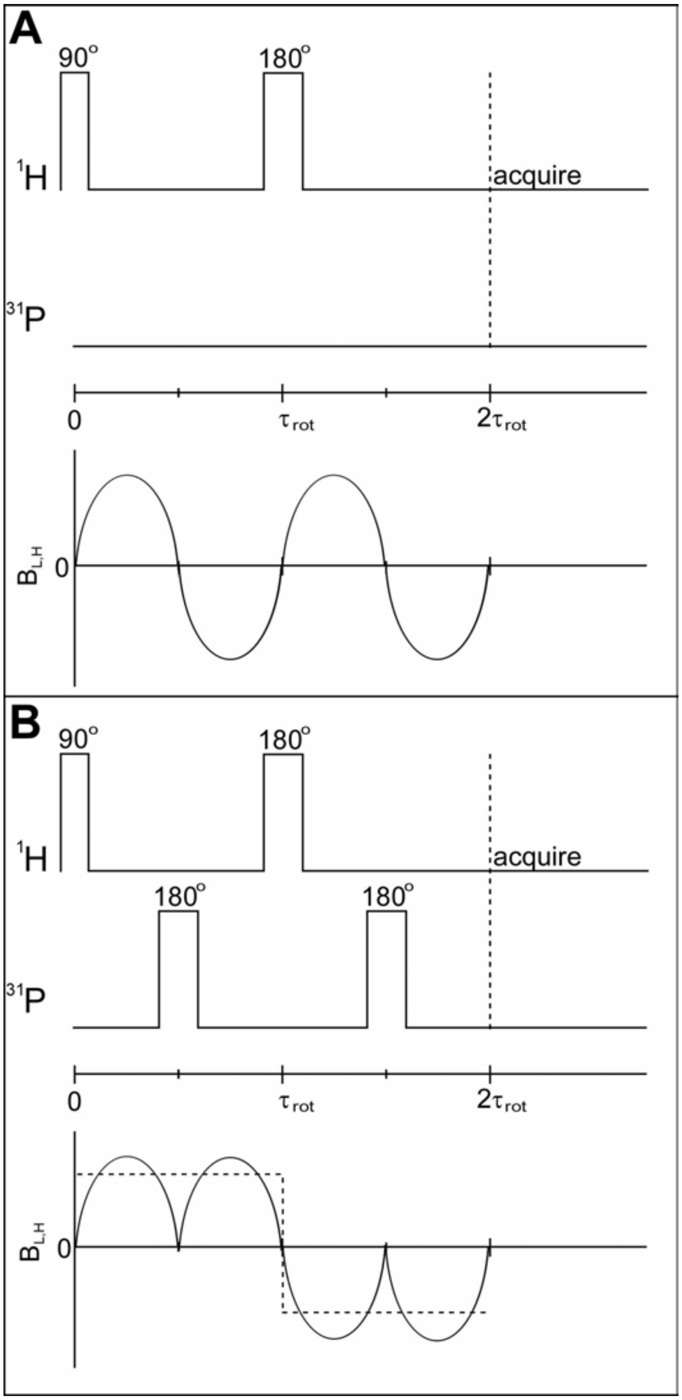

Figure 1.13. Standard pulse sequences depicting a two rotor cycle ^{1}H{^{31}P}REDOR experiment. **A.** ^{1}H Spin-echo control pulse sequence**. B.** ^{1}H{^{31}P} REDOR pulse sequence. Bottom diagrams in both **A** and **B** depict the evolution of the ^{1}H local field ($B_{L,H}$) during the experiment.

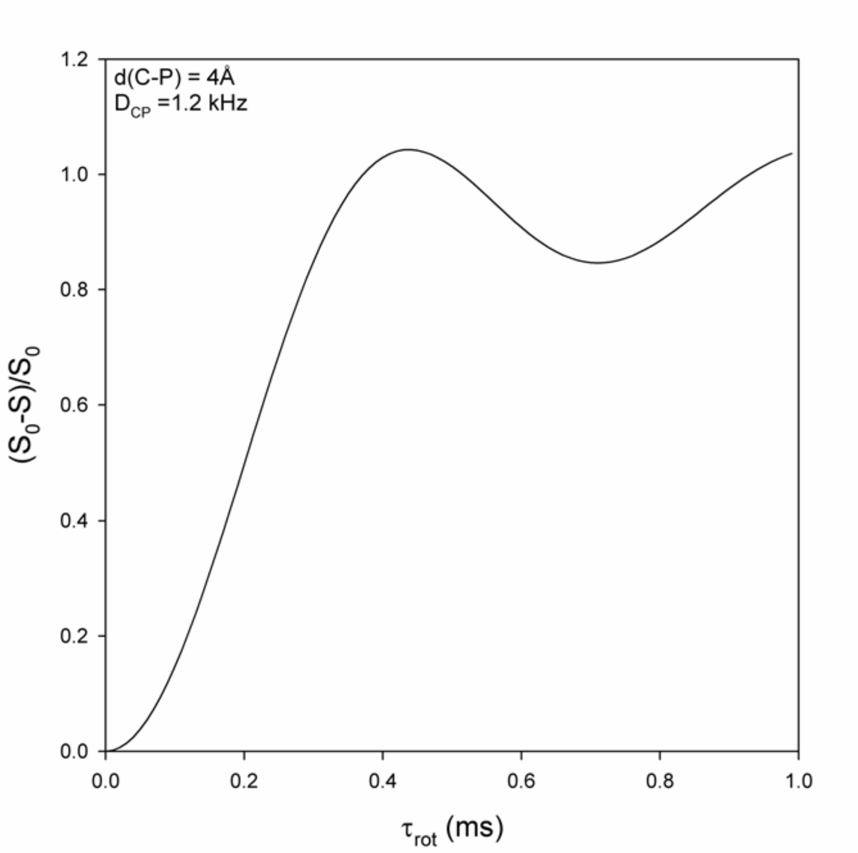

Figure 1.14. Simulated REDOR points and curve for a ^{13}C – ^{31}P pair located at a distance of 4 Å using the SIMPSON software package.

II. Phosphorus Speciation in Calcite Speleothems Determined from Solid-State NMR Spectroscopy

Reproduced with permission from Earth and Planetary Science Letters
Harris E. Mason [a], Silvia Frisia[b], Yuanzhi Tang[a], Richard J. Reeder[a], Brian L. Phillips[a], Phosphorus Speciation in Calcite Speleothems Determined from Solid-State NMR Spectroscopy, Earth Planet. Sc. Lett. 254(2007) 313-322. doi: 10.1016/j.epsl.2006.11.040

[a] *Center for Environmental Molecular Science, Department of Geosciences, State University of New York, Stony Brook, New York, 11794-2100*
[b] *Museo Tridentino di Scienze Naturali, via Calepina 14, 38100 Trento, Italy*

1. Abstract

Variations in speleothem P concentration show cyclic patterns that have important implications for high resolution paleoclimate and paleoenvironmental reconstructions. However, little is known about the speciation of P in calcite speleothems. Here we employ solid-state ^{31}P and ^{1}H magic angle spinning nuclear magnetic resonance (MAS NMR) spectroscopic techniques as a non-destructive method for analyzing the distribution of P in speleothems. The ^{31}P MAS NMR results show three peaks indicating the presence of three primary types of phosphate species in samples from the Grotta di Ernesto (northeastern Italy): a broad peak at a chemical shift $\delta_{P\text{-}31} = 3.1$ to 3.7 ppm from individual phosphate ions incorporated within calcite, a narrow set of peaks near $\delta_{P\text{-}31} = -0.9$ ppm from crystalline monetite and a narrow peak at $\delta_{P\text{-}31} = 2.9$ ppm from an unidentified crystalline phosphate phase. Essentially identical results were obtained for a synthetic calcite/phosphate coprecipitate. Spectra collected for a sample from Grotte de Clamouse (southern France) show only a broad peak near 3.5 ppm suggesting a possible limit for phosphate incorporation into the calcite structure. These data suggest that P in this system can interact to form calcium phosphate surface precipitates during infiltration events and are subsequently enclosed during calcite growth.

2. Keywords

speleothem; phosphate; calcite; NMR spectroscopy

3. Introduction

Speleothems are becoming one of the most promising archives of high resolution climate and environmental proxy data in a variety of continental settings. The last 5 years has seen a rapid advance in techniques capable of analyzing trace element concentrations in speleothem calcite at very high spatial resolution. The corresponding time series of trace element variability in stalagmites and stalactites are of great palaeoenvironmental and palaeoclimate significance. Furthermore, chemical time series can provide annual chronological markers [1]. The application of secondary ionization mass spectrometry (SIMS) [2-5] and excimer, laser-ablation inductively coupled plasma mass spectrometry (ELA-ICPMS) [6, 7] has allowed rapid generation of scans at a spatial resolution of the order of 10 micrometers. In these studies, P and Mg concentrations exhibit clear cycles which have been related to hydrology [6], temperature, and prior calcite precipitation [3].

In annually laminated specimens from Grotta di Ernesto, the association of high P content with visible, ca. 0.5 to 4 μm–thick, dark layers capping each lamina, has been interpreted as recording a short period of increased P supply during autumnal infiltration events [4]. Phosphorus appears, therefore, to be one of the trace elements that most clearly defines annual cycles in speleothems; its distribution appears to be related to the pattern of annual layering in a variety of environmental settings [4, 6]. Little is known, however, about the form in which P is present within cave calcite. The P-rich dark laminae fluoresce, implying that they contain higher concentrations of organic compounds derived from the soil zone [8]. P could be associated with a soil-derived organic fraction brought into the cave during the autumn rains. However, on the basis of average C/P ratio in soil organic matter, Huang et al. estimated that organic P in stalagmites from Grotta di Ernesto should amount to a maximum of ca. 9 ppm [4], which is much lower than the average of 43 ppm measured by SIMS. Huang et al., therefore, infer that the bulk of P is inorganic, but considered the distribution pattern to be inconsistent with submicroscopic apatite grains because P commonly encompasses the inclusion-rich layer. The current interpretation is that at concentrations below 100 ppm P may be present in speleothems as individual phosphate ions incorporated within the calcite structure [4], which reflects cave hydrology, and water chemistry variability [9].

Synchrotron radiation generated micro XRF maps at 2 μm resolution have shown that the lateral distribution of P in the annually laminated speleothems from Grotta di Ernesto follows laterally the visible dark layers marking each lamina. The range of P concentration within each dark layer is, however, wide [9]. Micrometer- to sub-micrometer sized P-rich pixels may be interpreted as associated with submicroscopic grains, which, if the hypothesis of Huang et al. [4] is correct, may not be apatite but some other phase or P adsorbed on colloidal particles [10]. Micrometer-sized, C-rich particles have indeed been observed by scanning electron microscopy in association with the calcite surface which grew across the autumnal flushing at Grotta di Ernesto [11].

Interactions between calcite and dissolved P have been studied extensively due to the potential role of phosphate in the inhibition of calcite crystal growth and the importance of phosphate sorption to mineral surfaces for mediating the geochemical cycling of P [12-20]. House and Donaldson [16] investigated phosphate adsorption and coprecipitation over a pH range of 7 to 9.5 using P concentrations of 1 to 18 μmol L^{-1} and calcite with a surface area of 0.22 and 0.37 m^2 g^{-1}, corresponding to a maximum surface loading of 4.9 P nm^{-2}. They concluded that phosphate coprecipitation, which gave overgrowths having >2000 ppm P, could be adequately explained by a two component adsorption model of PO_4^{3-} or $CaPO_4^-$ and HPO_4^{2-} or $CaHPO_4^0$. In addition they noted that during their adsorption experiments 80% of the P was removed from solution within the first 2 minutes after addition of calcite to the system. Hinedi et al [21] used solid-state ^{1}H and ^{31}P NMR spectroscopy to investigate phosphate sorption onto a high surface area calcite (22 m^2 g^{-1}). At phosphate loadings of 0.002 to 1.0 P nm^{-2} (0.79 to 36.72 μmol P g^{-1} calcite) they observed the sorption of unprotonated phosphate groups, and at higher phosphate loadings of 1.9 to 3.5 P nm^{-2} (69.92 to 128.22 μmol P g^{-1} calcite) the formation of brushite was observed. Dove and Hochella [22] studied calcite precipitation on a 3 mm^3 calcite crystal in the presence of 6 μmol phosphate (8.7 10^5 P nm^{-2}) with scanning force microscopy and found growth to proceed by the initial formation of unidentified globular surface precipitates followed by jagged step progression. These studies suggest that removal of dissolved P in the presence of calcite can occur quickly and by several processes including sorption, coprecipitation, and formation of surface precipitates.

Clearly, an understanding of the chemical form of P within calcite is needed, otherwise interpretation of climate and environmental proxy data becomes very difficult [10]. For example, it is possible that P concentration variations in calcite may reflect limits of the ability of calcite to incorporate phosphate ions brought about by factors other than the P concentration of the precipitating fluid. Given the broader implications that P in carbonates has as a palaeoenvironmental indicator in a variety of environments [23] , the present study aims at understanding its incorporation within natural and synthetic calcite. For this purpose, we used solid-state ^{31}P nuclear magnetic resonance (NMR) spectroscopy, which can measure the Pspeciation in natural materials [24-27]. Cave carbonates are good candidates for solid-state NMR spectroscopic studies because they exhibit a low abundance of paramagnetic ions [28]. Results for speleothem calcite from different climatic settings, including the Grotta di Ernesto speleothems for which P-rich layers seem to be good annual markers, and laboratory-grown crystals indicate that P can be incorporated in speleothem calcite through several processes, including coprecipitation and the formation of surface precipitates of crystalline calcium phosphate phases.

4. Materials and Methods

For the present study we chose specimens from two caves, Grotta di Ernesto and Grotte de Clamouse, characterized by different environmental, geologic and hydrologic settings, and for which much information is already available [11, 29-31]. Speleothems from these caves have been studied for palaeoclimate and environmental reconstruction [29, 32].

Grotta di Ernesto, is a shallow cave (ca. 20 m below the surface), located at an elevation of 1167 m in northeast Italy. It is cut in dolomitized limestone overlain by brown calcareous soil up to 1.5 m thick supporting a mixed conifer and deciduous wood. Mean annual temperature at the cave site is ca. 6.7°C and mean annual rainfall ca. 1300 mm/year, which results in positive net infiltration, with maxima between October and November following high rainfalls [11]. The cave hydrology responds to major recharge events in a relatively short time, from a few days up to three months [33], which result in the development of visible annual laminae in most Holocene stalagmites. Measured cave water pH values range from 7.9 to 8.5, and the saturation index (as $\log(IAP/K_{eq})$) of the drips from 0.1 to 0.35. Typical P concentrations for the Grotta di Ernesto drip water range from 0.10 to 0.26 μmol L^{-1}, but can range from 0.97 to 1.61 μmol L^{-1} during infiltration events [3]. Annual laminae of the speleothems consist of a thick, translucent and a thin dark layers [11, 33]. Modern cave calcite is mostly characterized by a few dislocations. In older portion of the specimens, microstructures such as dislocations and lamellae have been observed when the order in the stacking of the crystals is perturbed with increasing proportion of the dark layer in successive laminae [11].

Grotte de Clamouse is a relatively deep cave, which develops > 50 m below the surface cut in partially dolomitized limestone. The present climate is typically Mediterranean, with mean annual temperature of ca. 14.5°C and mean annual rainfall ca. 750 mm/year. Due to the dry conditions during summer months, negative infiltration is observed in June, July and August. Nevertheless, drips are relatively constant throughout the year; the hydrology of the cave is characterized by a high proportion of storage water in the aquifer. Measured cave water pH values range from ca.7.6 to ca. 7.8, and the saturation index of the drips range from -0.04 to 0.6 [30]. Holocene stalagmites commonly do not show visible or UV-fluorescent annual laminae. At present there is no information on P content in the drip waters. Previous studies indicate, however, that some trace elements such as Mg and Sr show annual variations [32]. Under the present-day cave environmental conditions, the calcite crystals are translucent, and show no microstructures or a few dislocations [30]. The crystals composing the speleothems from these two caves differ and may potentially reflect different incorporation of P.

The natural samples we analysed consisted of three calcite stalagmite speleothem samples ER67 (subsample a, unpublished), still active when removed, and the Holocene ER77 (subsample L) [33] and ER78 (subsample L) [9] from the Grotta di Ernesto, and the tip of stalagmite CL23 (unpublished), consisting of clearly visible calcite crystals, still active at the time of removal, from Grotte de Clamouse. Bulk samples of the ER67a, ER77.3L and ER78L speleothems were crushed to pass a 120 μm sieve and then bleached for an excess of nine days in a 6% commercial sodium hypochlorite solution to remove any organic material. Previous work has reported P contents of 69±20 ppm from SIMS traverses for similar speleothems from Grotta di Ernesto [3, 4], and concentrations about three times lower for a different sample from Grotte de Clamouse [34].

For phosphate coprecipitation with calcite we used a seeded constant-addition method adapted from Zhong and Mucci [35] and Tesoriero and Pankow [36] as described by Reeder et al. [37]. To a stirred reaction vessel containing 0.7 L of a solution with 0.007 M $CaCl_2$ and 0.007 M $NaHCO_3$ and a 0.1 M NaCl background electrolyte, 0.5 g of reagent grade calcite from Alfa Aesar (5 μm particle size) was added as nucleation seeds. A solution containing 0.1 M $CaCl_2$ and 0.1 M NaCl was pumped through a syringe at a constant rate of 150 μL/min into the reaction vessel while bubbling continuously with water-saturated air. From a second syringe a solution containing 0.1 M Na_2CO_3, 0.1 M NaCl and 20 μM K_2HPO_4 was pumped through anti-diffusion tips at the same rate. The total reaction time was 9 h, yielding 1.0 g of phosphate-containing calcite overgrowth on the 0.5 g of seed crystals. The initial solution had a measured pH of 7.86 and was supersaturated with respect to pure calcite, with a saturation index of 1.1 (expressed as log (IAP/K_{eq})), as calculated using the program PHREEQC [38]. During growth the solution pH increased initially and reached a constant value of 8.25 ± 0.1 within 4 to 5 h. Total CO_2 content in the solution was measured using the procedure described by Hall and Aller [39] and, along with pH, was used to assess when the system had reached a near steady-state with respect to calcite supersaturation. As the coprecipitation reaction proceeded, the total amount of CO_2 dropped continuously until near steady-state conditions were achieved, after around 5 hrs. At near steady-state the saturation index with respect to pure calcite was 0.44, as calculated using the program PHREEQC [38]. The final calcite powder was collected by vacuum filtration, washed multiple times with deionized water, and dried in an oven at 50ºC. X-ray diffraction (XRD) revealed only calcite phase. The total phosphate added to the system during crystal growth corresponds to 52 ppm P in the overgrowths, somewhat lower than the average P concentration for the Grotta di Ernesto samples.

All of the NMR spectra were collected on a 400 MHz Varian Inova spectrometer under magic-angle-spinning (MAS) conditions, at operating frequencies of 161.8 MHz and 399.8 MHz for ^{31}P and ^{1}H, respectively. For the ^{31}P experiments, samples were contained in 7.5 mm (o.d.) Si_3N_4 rotors and spun at 5 kHz. Single-pulse (SP) ^{31}P spectra were obtained with 3 μs pulses and relaxation delays that varied from 2 to 1000 s. Spectra taken at 500 s relaxation delay were used to obtain relative concentration ratios; spectra taken for some samples at a 1000 s relaxation delay showed no further increase in absolute intensity. For the

CP/MAS experiments, contact times of 1-2 ms were used. The probe and rotor assemblies yielded no detectable ^{31}P NMR signal after several days of acquisition. However, standard ZrO_2-based rotor sleeves give ^{31}P signals in the spectral region for orthophosphate groups. The ^{31}P NMR chemical shifts (δ_{P-31}) are referenced with respect to 85% phosphoric acid, using hydroxylapatite as a secondary reference set to $\delta_{P-31} = 2.65$ ppm. The ^{1}H SP MAS NMR spectra were obtained using a Chemagnetics probe assembly configured for 4 mm (o.d.) rotors and modified to yield very low ^{1}H background signal. A spinning rate of 15 kHz and a 90° pulse width of 3.5 μs were used. The ^{1}H NMR chemical shifts (δ_{H-1}) are referenced with respect to tetramethylsilane (TMS) using adamantane as a secondary reference set to $\delta_{H-1} = 2.0$ ppm.

5. Results and Discussion

The ^{31}P NMR spectra of all the samples studied can be described by three orthophosphate components consisting of a broad peak with a chemical shift near $\delta_{P-31} = 3.5$ ppm, a narrow resonance at $\delta_{P-31} = 2.9$ ppm and a narrow set of peaks centered near $\delta_{P-31} = -1$ ppm. The single-pulse (SP) spectra in Figure 2.1 show all of the P environments in the samples, but were obtained under experimental conditions that suppress the narrow peak at 2.9 ppm so that the broad peak near 3.5 ppm can be distinguished. The intensities of the NMR peaks depend on the ^{31}P spin-lattice relaxation time and the experimental relaxation delay [40]. The relaxation times differ substantially among the distinct P environments, with that for the peak at $\delta_{P-31} = 2.9$ ppm being by far the longest. Thus, the relative intensity of the peak at 2.9 ppm appears smaller at short relaxation delay. Figure 2.2a shows a typical spectrum (for ER78L) obtained under quantitative conditions, in which the integrated areas of the peaks are proportional to the concentration of the corresponding P environments. The ^{31}P{^{1}H} cross-polarization (CP) spectra (Fig. 2.3) contain signal only for P that is in close spatial proximity to H (less than about 4Å). The calcite seeds used to prepare the synthetic calcite/phosphate coprecipitate yielded no detectable ^{31}P NMR signal by SP or CP methods, thus the spectra for this sample correspond only to P in the overgrowths even though NMR detects the entire sample.

All samples show a broad peak at $\delta_{P\text{-}31}$ = 3.1 ppm to 3.7 ppm (3.6 – 3.8 ppm full width at half-maximum; FWHM) in both the SP and CP spectra (Figs. 2.1, 2.3, and Table 2.1). This peak is similar in position and width to that reported by Hinedi et al [21], which they assigned to unprotonated phosphate groups sorbed onto the surface of calcite. In our samples this peak likely represents phosphate groups that have sorbed onto the surface and subsequently become incorporated as defects during calcite growth. The large width of this peak indicates a distribution of phosphate environments (e.g., bond lengths and angles), as would be expected for a defect structure. The presence of this peak in CP spectra indicates that it corresponds to P in close proximity to H. It is likely that even if these coprecipitated phosphates are unprotonated, other H-bearing species are likely to be present and serve to accommodate the charge imbalance and structural defects created by phosphate substitution in the calcite structure. This observation is in agreement with reports of high levels of H detected by ion probe in the dark, autumnal portion of Grotta di Ernesto stalagmite annual laminae, where P concentration also increases [3, 4], and with the ^{1}H NMR data presented below. The H detected by ion microprobe is consistent with the presence of molecular water or nano-inclusions [41]. However, CP signal requires rigid H species, perhaps indicative of structural defects.

Narrow peaks at a chemical shift near $\delta_{P\text{-}31}$ = -0.9 ppm (1.1 to 1.5 ppm FWHM) occur in both the SP and CP spectra taken for the Grotta di Ernesto samples and the synthetic calcite/phosphate coprecipitate (Figs. 2.1 and 2.3, and Table 2.1). In most spectra this peak occurs at the average position for the two peaks characteristic of crystalline monetite ($CaHPO_4$) [42, 43], which were not resolved in these spectra due to the low ^{1}H decoupling power used. The CP spectrum taken for the synthetic sample (Fig. 2.3) clearly shows two peaks at $\delta_{P\text{-}31}$ = -0.5 ppm (1.3 ppm FWHM) and -1.8 ppm (1.5 FWHM) that closely resemble those previously reported for monetite [42, 43]. The presence of monetite is also supported by the occurrence of a small characteristic peak in the ^{1}H SP MAS NMR spectra of these samples (see below).

The ^{31}P SP spectra of the Grotta di Ernesto and synthetic samples also show a prominent narrow peak at a chemical shift $\delta_{P\text{-}31}$ = 2.9 ppm (0.7 to 0.9 ppm FWHM) that dominates the spectra, but which is notably absent from the CP spectra (cf. Figs. 2.1 and 2.3). The position and width of this narrow peak is within the range of those previously reported for hydroxylapatite [42-44], but is slightly shifted from our measurement for reagent grade material ($\delta_{P\text{-}31} = 2.65$ ppm). Under our experimental conditions even a small fraction of hydroxylapatite would yield a peak in the CP spectra, because of its high $^{31}P\{^{1}H\}$ CP efficiency [45]. Additional CP spectra were taken over a range of experimental conditions, particularly at short and long contact times (0.5 to 7 ms) and long and short relaxation delays (up to 60 s), but no corresponding peak at $\delta_{P\text{-}31} = 2.9$ ppm was observed. The narrow line shape (0.7 to 0.9 ppm FWHM) of this peak indicates a very uniform P environment and suggests strongly that it arises from a well-ordered crystalline phase. However, the ^{31}P NMR properties of other possible Ca-phosphate phases such as tricalcium phosphate, whitlockite, and tetracalcium phosphate do not match any of our data [43, 46, 47]. We tentatively assign this peak at 2.9 ppm to an anhydrous Ca-orthophosphate but cannot identify the phase from the current data. Orthophosphate is indicated by the absence of spinning sidebands, which would be prominent for pyrophosphate groups [48]. Assignment to a Ca-phosphate seems likely because this peak also occurs in the synthetic sample, which was precipitated from a solution containing only Na^{+}, K^{+}, and Ca^{2+} cations.

To obtain quantitative ratios for the three types of phosphate environments we fit the SP spectra taken under quantitative conditions (500 s relaxation delay) to a sum of Gaussian curves (Fig. 2.2), with the constraint that for each sample the width and position of the broad peak centered near $\delta_{P\text{-}31} = 3.5$ ppm equal those observed in the corresponding CP spectrum. The results for the Grotta di Ernesto samples (Table 2.1) indicate that the majority of the P species present (57 to 71%) is represented by the peak at $\delta_{P\text{-}31} = 2.9$ ppm, followed by 25 to 30% as phosphate coprecipitated in calcite (peak at $\delta_{P\text{-}31} = 3.5$ ppm), and 4 to 16% as monetite (peak at $\delta_{P\text{-}31} = -0.9$ ppm). The synthetic calcite/phosphate coprecipitate shows the same P species, but with the peak for phosphate in calcite the most abundant (47%) followed by the peak at $\delta_{P\text{-}31} = 3.0$ ppm (35%) and monetite (17%). This result indicates the synthesis method employed can reproduce the P species present in the natural samples.

Further support for the presence of monetite inclusions is provided by ^{1}H SP MAS NMR data. For the Grotta di Ernesto samples the ^{1}H spectra (Fig. 2.4) are dominated by a narrow peak at $\delta_{H\text{-}1} = 4.8$ ppm, but also contain peaks at $\delta_{H\text{-}1} = 1.5$ ppm and 13.9 ppm in addition to a shoulder on the main peak at about 7.4 ppm and a broad unresolved peak underlying all the peaks, centered at about 6.5 ppm. The dominant peak at $\delta_{H\text{-}1} = 4.8$ ppm arises from aqueous fluid inclusions [49] whereas that at 1.5 ppm has been assigned to hydroxyl groups at defect sites in calcite [50]. The peak at $\delta_{H-1} = 7.4$ ppm is characteristic of bicarbonate defects within the calcite structure [51] and the broad underlying peak, which is not evident at the scaling used for Fig. 2.4, likely arises from rigidly bound structural water [50]. The peak at $\delta_{H-1} = 13.9$ ppm peak occurs in all the Grotta di Ernesto and synthetic samples and is consistent with assignment to acidic protons in monetite [52]. This result supports the assignment of the ^{31}P NMR peaks to this phase. Sample CL23 does not give a ^{1}H NMR peak at 13.9 ppm, in agreement with the absence of peaks for monetite in the ^{31}P spectra of this sample.

These ^{1}H NMR spectra also provide further evidence for the absence of hydroxylapatite in the speleothem samples. Hydroxylapatite gives a narrow ^{1}H NMR peak at $\delta_{H-1} = 0.2$ ppm [52], but a peak near this position was not observed for any of the natural samples (Fig. 2.4). Although the main ^{31}P NMR peak for the Grotta di Ernesto samples occurs near the chemical shift for hydroxylapatite, the absence of a ^{1}H NMR peak at $\delta_{H-1} = 0.2$ ppm for these samples provides strong evidence against assignment to this phase, especially considering that a ^{1}H NMR peak for the less abundant monetite is observed. The synthetic calcite/phosphate coprecipitate does show a peak at $\delta_{H-1} = 0.2$ ppm (Fig. 2.4). However, this peak was also observed in the ^{1}H MAS NMR spectra of calcite precipitated by the same method and seeds but in the absence of phosphate [51], and in samples prepared in D_2O [53], suggesting that it arises from an impurity in the calcite seed crystals.

These observations indicate that the principal P species in the Grotta di Ernesto and synthetic samples, corresponding to the peak at $\delta_{P-31} = 2.9$ ppm, does not arise from hydroxylapatite. However, assignment to a crystalline phosphate inclusion, possibly originating as a surface precipitate, remains the most likely explanation for this NMR signal. Although we cannot completely rule out the possibility of a second type of phosphate environment in calcite at this time, assignment of the peak at $\delta_{P-31} = 2.9$ ppm to a calcite defect is very unlikely considering the small width of this peak (0.7 ppm FWHM), which reflects a very uniform bonding environment for phosphate as expected for a crystalline phase. This peak is narrower than those for many crystalline phosphates [42-44, 46, 47]. Phosphate defects in calcite are expected to exhibit a range of local structural environments for accommodating the size and charge difference between carbonate and phosphate groups, giving a distribution of ^{31}P chemical shifts such as that observed for the peak near $\delta_{P\text{-}31}$ = 3.5 ppm for all samples. The width of this peak (3-4 ppm, FWHM) spans the range of ^{31}P chemical shifts for Ca-orthophosphates and is similar to that observed for amorphous calcium phosphate [54]. If a second, well-ordered type of phosphate environment could occur in calcite, it should be present in all samples. However, the peak at $\delta_{P\text{-}31}$ = 2.9 ppm is completely absent in the spectra for the CL23 sample, but would have been detected even if it represented a small fraction of the P.

The low signal intensity observed in the ^{31}P NMR spectra from the Grotte de Clamouse sample (CL23) indicates that this sample has the lowest P-content of the samples studied, consistent with the P concentrations measured for other samples from this locality (ca. 20 ppm [34]). The ^{31}P NMR spectra of CL23 contain only the broad peak near $\delta_{P\text{-}31}$ = 3.5 ppm (Figs. 2.1 and 2.3) and indicate that P is present only as individual phosphate ions incorporated into the calcite. Comparison of the absolute intensity of this peak to the corresponding resonance from the Grotta di Ernesto samples indicates that the concentration of P represented by this peak is comparable among all the samples. The lack of resonances from crystalline phases in the CL23 sample suggests that there is a P threshold for formation of surface precipitates, and, conversely, a limit for phosphate coprecipitation into the calcite structure.

With the information from the present study we can begin to understand the underlying mechanisms that control the incorporation of P in speleothems. Our results indicate that some P occurs in speleothems as individual phosphate ions in calcite defects as suggested by Huang et al. [4]. This appears to be the only incorporation mechanism for the P-poor, defect-poor Grotte de Clamouse calcite. At higher P concentrations, phosphate defects in calcite also occur, but most of the P is incorporated as crystalline phosphate phases. At similar P concentrations, other factors such as crystal morphology, P speciation in the parent waters, and crystal growth rate might contribute to the differences observed in these samples. For example, differences in P distribution between the Grotta di Ernesto and synthetic samples, which have similar total P concentrations, might be related to the faster growth rate for the lab-grown crystals.

Even though there appears to be a limit for phosphate incorporation in the calcite structure, our study suggests that P remains a good indicator of environmental changes, provided the system is well-characterized. The residence time of water in the aquifer above the Grotta di Ernesto, which has been reported to be <1 week during major infiltration events [4], allows some P to be flushed before it can be mineralized in the soil. The periods between infiltration events are likely too long to prevent mineralization of P in soils. Since we observe the formation of precipitates over the course of a few hours in the seeded growth experiments and that adsorption of phosphate on the calcite surface has been reported to occur on the order of a few minutes [16] it is likely these same processes may form surface precipitates in the span of a few days after a major infiltration event in a natural setting. In the time between infiltration events these surfaces would then be exposed to solutions with lower P concentrations and calcite precipitation would continue, enclosing any surface precipitates. These processes would then repeat over a given season giving a band concentrated in P with respect to the surrounding calcite matrix. The large spot size for SIMS and ELA-ICPMS (10-25 μm) relative to typical surface precipitate size (e.g., 3 nm height reported in ref. [55]) and scanning geometry relative to the calcite growth surfaces will only give the average concentration for the area being scanned and not the concentration represented by crystalline surface precipitates and thus will likely prevent analyzed P concentrations from exceeding ca. 100 - 200 ppm.

The results of the present study have potentially wide ranging implications for the distribution of P in other low-temperature geochemical settings dominated by carbonates. Interactions of dissolved inorganic phosphate with the surface of calcite and corresponding incorporation mechanisms similar to those we observe in the synthetic and speleothem samples can be expected to occur also in soils and sediments, affecting the distribution and cycling of P in these environments. Incorporation of phosphate in calcite as crystalline inclusions is likely to reduce P mobility in sediments during recrystallization and delay formation of the thermodynamically stable apatite phases. Current models cannot predict surface precipitation and, indeed, distinguishing whether phosphate removal from solution occurs by sorption, coprecipitation, or formation of a surface precipitate is a difficult problem [56]. Clearly, standard treatments for trace element incorporation, such as linear distribution coefficients, are insufficient to describe the phosphate distribution we observe in the speleothem and synthetic samples, especially at higher P concentration. Further analytical and experimental work is needed to identify the main phosphate inclusion we observe in the calcite speleothems, to determine whether similar P distributions occur in carbonate minerals from other low-temperature environments, and how this distribution depends on the precipitation conditions and growth rate. However, our results show that solid-state ^{31}P NMR spectroscopy can be used to determine in situ the distribution of P in carbonate minerals at the concentrations found in nature.

6. Conclusions

Our results indicate that calcite speleothems can contain phosphate in several forms, including phosphate defects in calcite and several types of coexisting crystalline phosphate inclusions. The presence of crystalline inclusions indicates that the ability of calcite speleothems to record P flushing events is not limited by the solubility of phosphate ions in the calcite structure. Calcite crystal growth appears capable of effectively encasing surface precipitates that form during periods of high P flux, forming inclusions. The results for the CL23 sample, however, indicate that these precipitates do not form in all cases and that their formation is likely related to periods of higher P influx. The phosphate/calcite coprecipitation experiment indicates that it is possible to reproduce in chemically simple systems the essential P environments present in the speleothems, suggesting that the formation of the included phases does not depend on other cations or anions present at trace concentration.

7. Acknowledgments

We thank Ian Fairchild and two anonymous reviewers for insightful comments that led to many improvements to the manuscript. This work was supported by the US-NSF through the Center for Environmental Molecular Science (CHE-0221934) and EAR-0310200 (B.L.P). S.F. acknowledges support from the AQUAPAST project (funded by Provincia Autonoma di Trento) and FG 668 of DFG (DAPHNE).

8. References

[1] J.U.L. Baldini, F. McDermott, I.J. Fairchild, Structure of the 8200-year cold event revealed by a speleothem trace element record, Science 296(2002) 2203-2206.

[2] M.S. Roberts, P.L. Smart, A. Baker, Annual trace element variations in a Holocene speleothem, Earth Planet. Sci. Lett. 154(1998) 237-246.

[3] I.J. Fairchild, A. Baker, A. Borsato, S. Frisia, R.W. Hinton, F. McDermott, A.F. Tooth, Annual to sub-annual resolution of multiple trace-element trends in speleothems, J. Geol. Soc. London 158(2001) 831-841.

[4] H.M. Huang, I.J. Fairchild, A. Borsato, S. Frisia, N.J. Cassidy, F. McDermott, C.J. Hawkesworth, Seasonal variations in Sr, Mg and P in modern speleothems (Grotta di Ernesto, Italy), Chem. Geol. 175(2001) 429-448.

[5] A.A. Finch, P.A. Shaw, G.P. Weedon, K. Holmgren, Trace element variation in speleothem aragonite: potential for palaeoenvironmental reconstruction, Earth Planet. Sci. Lett. 186(2001) 255-267.

[6] P.C. Treble, J. Chappell, J.M.G. Shelley, Complex speleothem growth processes revealed by trace element mapping and scanning electron microscopy of annual layers, Geochim. Cosmochim. Acta 69(2005) 4855-4863.

[7] J.M. Desmarchelier, J.C. Hellstrom, M.T. McCulloch, Rapid trace element analysis of speleothems by ELA-ICP-MS, Chem. Geol. 231(2006) 102-117.

[8] A. Baker, P.L. Smart, R.L. Edwards, D.A. Richards, Annual growth banding in a cave stalagmite, Nature 364(1993) 518-520.

[9] S. Frisia, A. Borsato, I.J. Fairchild, J. Susini, Variations in atmospheric sulphate recorded in stalagmites by synchrotron micro-XU and XANES analyses, Earth Planet. Sci. Lett. 235(2005) 729-740.

[10] I.J. Fairchild, C.L. Smith, A. Baker, L. Fuller, C. Spotl, D. Mattey, F. McDermott, E.I.M.F., Modification and preservation of environmental signals in speleothems, Earth Sci. Rev. 75(2006) 105-153.

[11] S. Frisia, A. Borsato, I.J. Fairchild, F. McDermott, Calcite fabrics, growth mechanisms, and environments of formation in speleothems from the Italian Alps and southwestern Ireland, J. Sediment. Res. 70(2000) 1183-1196.

[12] R.A. Griffin, J.J. Jurinak, Interaction of phosphate with calcite, Soil Sci. Soc. Am. J. 37(1973) 847-850.

[13] M.M. Reddy, Crystallization of calcium carbonate in presence of trace concentrations of phosphorus containing anions. 1. Inhibition by phosphate and glycerophosphate ions at pH 8.8 and 25ºC, J. Cryst. Growth 41(1977) 287-295.

[14] J. Dekanel, J.W. Morse, Chemistry of orthohosphate uptake from seawater onto calcite and aragonite, Geochim. Cosmochim. Acta 42(1978) 1335-1340.

[15] H.J. Meyer, The influence of impurities on the growth rate of calcite, J. Cryst. Growth 66(1984) 639-646.

[16] W.A. House, L. Donaldson, Adsorption and coprecipitation of phosphate on calcite, J. Colloid Interface Sci. 112(1986) 309-324.

[17] W.A. House, Inhibition of calcite crystal growth by inorganic phosphate, J. Colloid Interface Sci. 119(1987) 505-511.

[18] A. Mucci, Growth kinetics and composition of magnesian calcite overgrowths precipitated from seawater: Quantitative influence of orthophosphate ions, Geochim. Cosmochim. Acta 50(1986) 2255-2265.

[19] E.A. Burton, L.M. Walter, The role of pH in phosphate inhibition of calcite and aragonite precipitation rates in seawater, Geochim. Cosmochim. Acta 54(1990) 797-808.

[20] L.J. Plant, W.A. House, Precipitation of calcite in the presence of inorganic phosphate, Colloids Surf., A 203(2002) 143-153.

[21] Z.R. Hinedi, S. Goldberg, A.C. Chang, J.P. Yesinowski, A ^{31}P and ^{1}H MAS NMR study of phosphate sorption onto calcium carbonate, J. Colloid Interface Sci. 152(1992) 141-160.

[22] P.M. Dove, M.F. Hochella, Calcite precipitation mechanisms and inhibition by orthophosphate: In situ observations by scanning force microscopy, Geochim. Cosmochim. Acta 57(1993) 705-714.

[23] P. Montagna, M. McCulloch, M. Taviani, C. Mazzoli, B. Vendrell, Phosphorus in cold-water corals as a proxy for seawater nutrient chemistry, Science 312(2006) 1788-1791.

[24] R. Lookman, H. Geerts, P. Grobet, R. Merckx, K. Vlassak, Phosphate speciation in excessively fertilized soil: A ^{31}P and ^{27}Al MAS NMR spectroscopy study, Eur. J. Soil Sci. 47(1996) 125-130.

[25] L.L. Clark, E.D. Ingall, R. Benner, Marine phosphorus is selectively remineralized, Nature 393(1998) 426-426.

[26] L.C. Kolowith, R.A. Berner, Weathering of phosphorus in black shales, Global Biogeochemical Cycles 16(2002).

[27] S. Hunger, H. Cho, J.T. Sims, D.L. Sparks, Direct speciation of phosphorus in alum-amended poultry litter: Solid-State ^{31}P NMR investigation, Environ. Sci. Technol. 38(2004) 674-681.

[28] A. Kuczumow, D. Genty, P. Chevallier, J. Nowak, M. Florek, A. Buczynska, X-ray and electron microprobe investigation of the speleothems from Godarville tunnel, X-Ray Spectrom. 34(2005) 502-508.

[29] F. McDermott, S. Frisia, Y.M. Huang, A. Longinelli, B. Spiro, T.H.E. Heaton, C.J. Hawkesworth, A. Borsato, E. Keppens, I.J. Fairchild, K. van der Borg, S. Verheyden, E. Selmo, Holocene climate variability in Europe: Evidence from δ^{18}O, textural and extension-rate variations in three speleothems, Quat. Sci. Rev. 18(1999) 1021-1038.

[30] S. Frisia, A. Borsato, I.J. Fairchild, F. McDermott, E.M. Selmo, Aragonite-calcite relationships in speleothems (Grotte de Clamouse, France): Environment, fabrics, and carbonate geochemistry, J. Sediment. Res. 72(2002) 687-699.

[31] V. Plagnes, C. Causse, G. Dominique, M. Paterne, D. Blamart, A discontinuous climatic record from 187 to 74 ka from a speleothem of the Clamouse Cave (south of France), Earth Planet. Sci. Lett. 201(2002) 87-103.

[32] E.A. McMillan, I.J. Fairchild, S. Frisia, A. Borsato, F. McDermott, Annual trace element cycles in calcite-aragonite speleothems: Evidence of drought in the western Mediterranean 1200-1100 yr BP, J. Quat. Sci. 20(2005) 423-433.

[33] S. Frisia, A. Borsato, N. Preto, F. McDermott, Late Holocene annual growth in three Alpine stalagmites records the influence of solar activity and the North Atlantic Oscillation on winter climate, Earth Planet. Sci. Lett. 216(2003) 411-424.

[34] E.A. McMillan, Tests for paleoaridity in Holocene Stalagmites from SW Europe. Ph.D. Thesis (unpublished), Keele University, U.K., (2006).

[35] S.J. Zhong, A. Mucci, Calcite precipitation in seawater using a constant addition technique: A new overall reaction kinetic expression, Geochim. Cosmochim. Acta 57(1993) 1409-1417.

[36] A.J. Tesoriero, J.F. Pankow, Solid solution partitioning of Sr^{2+}, Ba^{2+}, and Cd^{2+} to calcite, Geochim. Cosmochim. Acta 60(1996) 1053-1063.

[37] R.J. Reeder, M. Nugent, G.M. Lamble, C.D. Tait, D.E. Morris, Uranyl incorporation into calcite and aragonite: XAFS and luminescence studies, Environ. Sci. Technol. 34(2000) 638-644.

[38] D.L. Parkhurst, C.A.J. Appelo, User's guide to PHREEQC (Version 2) – A computer program for speciation, batch-reaction, one-dimensional transport, and inverse geochemical calculations. , U. S. Geol. Surv. Water Res. Inv. Rept., 1999, pp. 99-4259.

[39] P.O. Hall, R.C. Aller, Rapid, small-volume, flow injection analysis for ΣCO_2 and NH^{4+} in marine and fresh waters, Limnol. Oceanogr. 37(1992) 1113-1119.

[40] M.A. Nanny, R.A. Minear, J.A.e. Lenheer, Nuclear Magnetic Resonance Spectroscopy in Environmental Science and Technology, Oxford University Press, London, 1997.

[41] F. McDermott, H.P. Schwarcz, P.J. Rowe, Isotopes in speleothems. In: Isotopes in Palaeoenvironmental Research, Springer, Dordrecht, The Netherlands, 2005 (in press).

[42] W.P. Aue, A.H. Roufosse, M.J. Glimcher, R.G. Griffin, Solid-State ^{31}P nuclear magnetic resonance studies of synthetic solid phases of calcium phosphate: Potential models of bone mineral, Biochemistry 23(1984) 6110-6114.

[43] P.S. Belton, R.K. Harris, P.J. Wilkes, Solid-state ^{31}P NMR studies of synthetic inorganic calcium phosphates, J. Phys. Chem. Solids 49(1988) 21-27.

[44] W.P. Rothwell, J.S. Waugh, J.P. Yesinowski, High-resolution variable-temperature ^{31}P NMR of solid calcium phosphates, J. Am. Chem. Soc. 102(1980) 2637-2643.

[45] A. Kaflak, D. Chmielewski, A. Gorecki, A. Slorarczyk, W. Kolodziejski, Efficiency of $^{1}H \rightarrow ^{31}P$ cross-polarization in bone apatite and its mineral standards, Solid State Nucl. Magn. Reson. 29(2006) 345-348.

[46] J. Vogel, C. Russel, G. Gunther, P. Hartmann, F. Vizethum, N. Bergner, Characterization of plasma-sprayed hydroxyapatite by ^{31}P-MAS-NMR and the effect of subsequent annealing, J. Mater. Sci.: Mater. Med. 7(1996) 495-499.

[47] M. Bohner, J. Lemaitre, A.P. Legrand, J.B.D. delaCaillerie, P. Belgrand, Synthesis, X-ray diffraction and solid-state ^{31}P magic angle spinning NMR study of alpha-tricalcium orthophosphate, J. Mater. Sci.: Mater. Med. 7(1996) 457-463.

[48] D. Prochnow, A.R. Grimmer, D. Freude, Solid-state NMR studies of ^{17}O-enriched pyrophosphates, Solid State Nucl. Magn. Reson. 30(2006) 69-74.

[49] J.P. Yesinowski, H. Eckert, G.R. Rossman, Characterization of hydrous species in minerals by high-speed ^{1}H MAS-NMR, J. Am. Chem. Soc. 110(1988) 1367-1375.

[50] S.J. Gaffey, H_2O and OH in echinoid calcite: A spectroscopic study, Am. Mineral. 80(1995) 947-959.

[51] J. Feng, Y. Lee, R.J. Reeder, B.L. Phillips, Observation of bicarbonate in calcite by NMR spectroscopy, Am. Mineral. 91(2006) 957-960.

[52] J.P. Yesinowski, H. Eckert, Hydrogen environments in calcium phosphates: ^{1}H MAS NMR at high spinning speeds, J. Am. Chem. Soc. 109(1987) 6274-6282.

[53] B.L. Phillips, Y.J. Lee, R.J. Reeder, Organic coprecipitates with calcite: NMR spectroscopic evidence, Environ. Sci. Technol. 39(2005) 4533-4539.

[54] J. Tropp, N.C. Blumenthal, J.S. Waugh, Phosphorus NMR study of solid amorphous calcium phosphate, J. Am. Chem. Soc. 105(1983) 22-26.

[55] V.G.R. Chada, D.B. Hausner, D.R. Strongin, A.A. Rouff, R.J. Reeder, Divalent Cd and Pb uptake on calcite $\{10\bar{1}4\}$ cleavage faces: An XPS and AFM study, J. Colloid Interface Sci. 288(2005) 350-360.

[56] L. Li, R. Stanforth, Distinguishing adsorption and surface precipitation of phosphate on goethite (α-FeOOH), J. Colloid Interface Sci. 230(2000) 12-21.

9. Figures and Captions

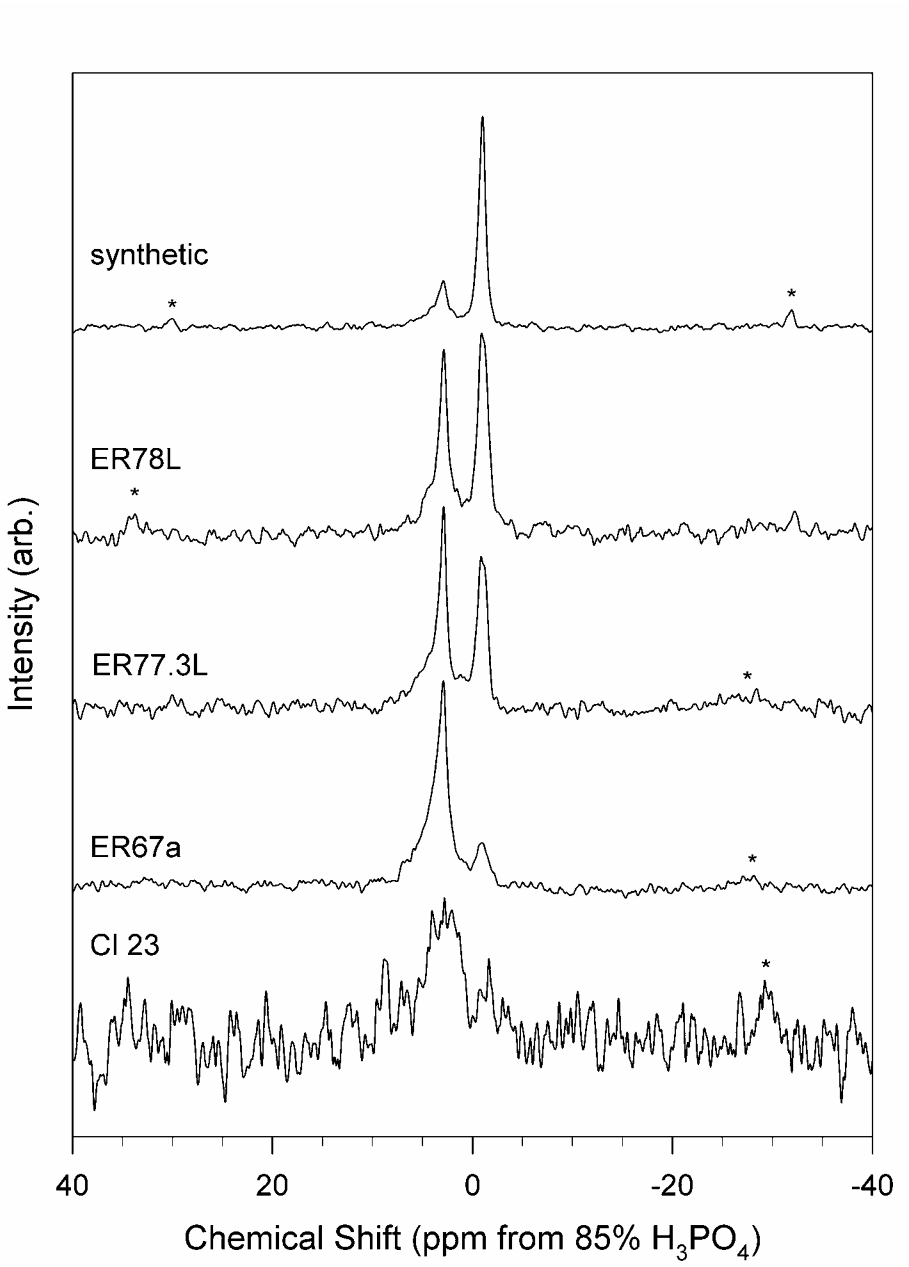

Figure 2.1. ^{31}P single-pulse (SP) MAS NMR spectra of speleothem and synthetic samples studied. Spectra were collected at a spin rate of 5 kHz and a pulse delay of 2 s for (from bottom to top) 42386, 127221, 42272, 42029, and 45580 acquisitions. Asterisks denote spinning sidebands

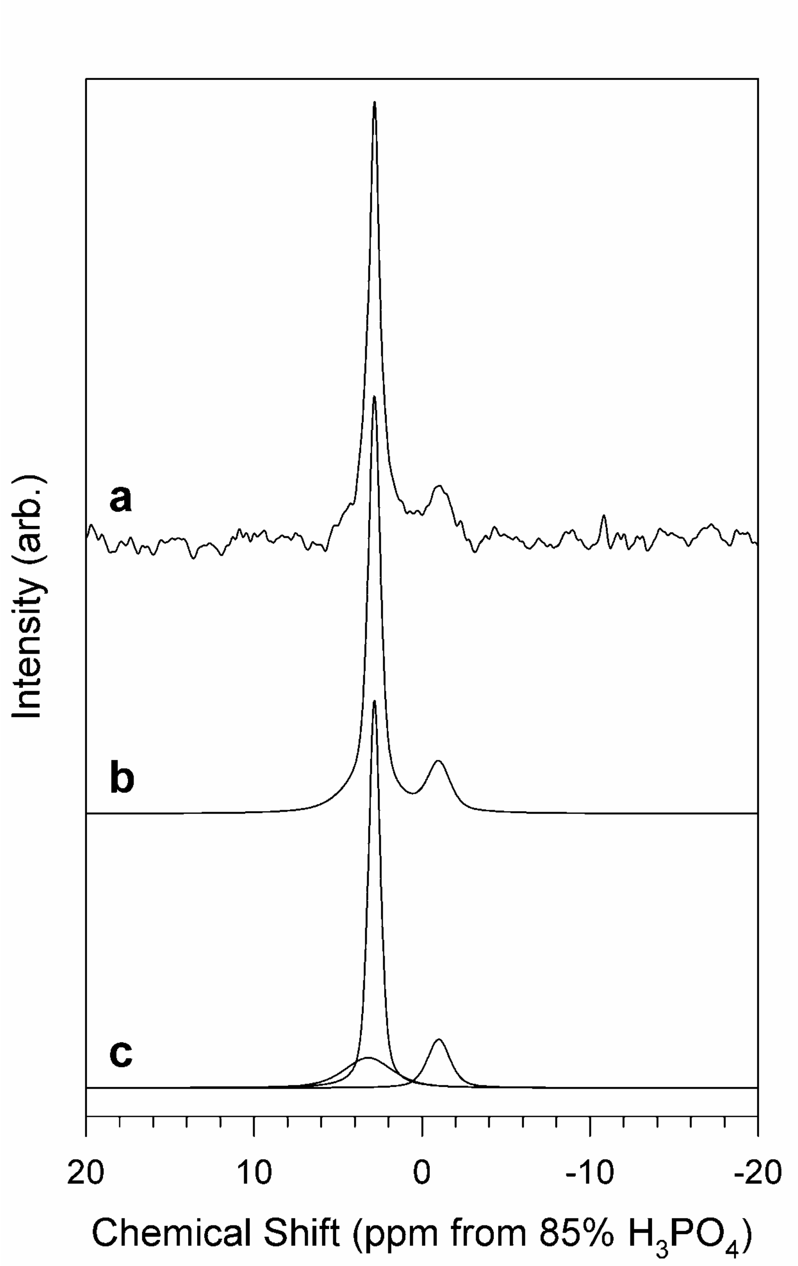

Figure 2.2. **a)** ^{31}P SP MAS NMR spectrum of calcite speleothem ER78L acquired under quantitative conditions, corresponding to 472 acquisitions at a relaxation delay of 500 s. **b)** The spectral profile from a least-squares fit to the experimental data. **c)** The individual curves for the least-squares fit shown in **b),** corresponding to the principal phosphate environments: phosphate in calcite ($\delta_{P\text{-}31}$ = 3.2 ppm, 3.6 ppm FWHM), unidentified crystalline inclusion ($\delta_{P\text{-}31}$ = 3.0 ppm, 0.6 ppm FWHM), and monetite ($\delta_{P\text{-}31}$ = -1 ppm, 1.1 ppm FWHM).

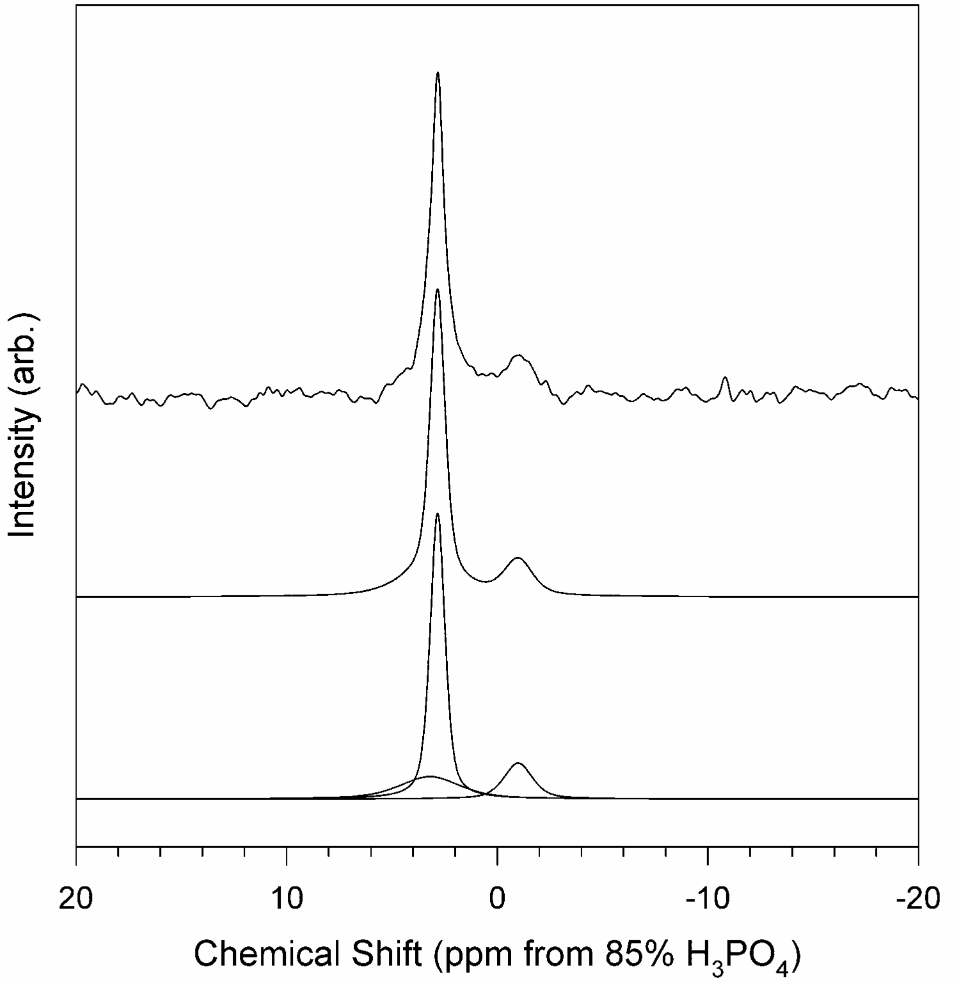

Figure 2.3. $^{31}P\{^1H\}$CP/MAS NMR spectra of speleothem and synthetic samples studied (See text for description). Spectra were collected at a spin rate of 5 kHz and 1 s relaxation delay, with contact time of 5 ms for CL23 and 2 ms for ER67a, ER77.3L, ER78L and synthetic calcite/phosphate coprecipitate. Spectra represent (from bottom to top) 165112, 139094, 155135, 100000, and 100000 acquisitions. Asterisks denote spinning sidebands.

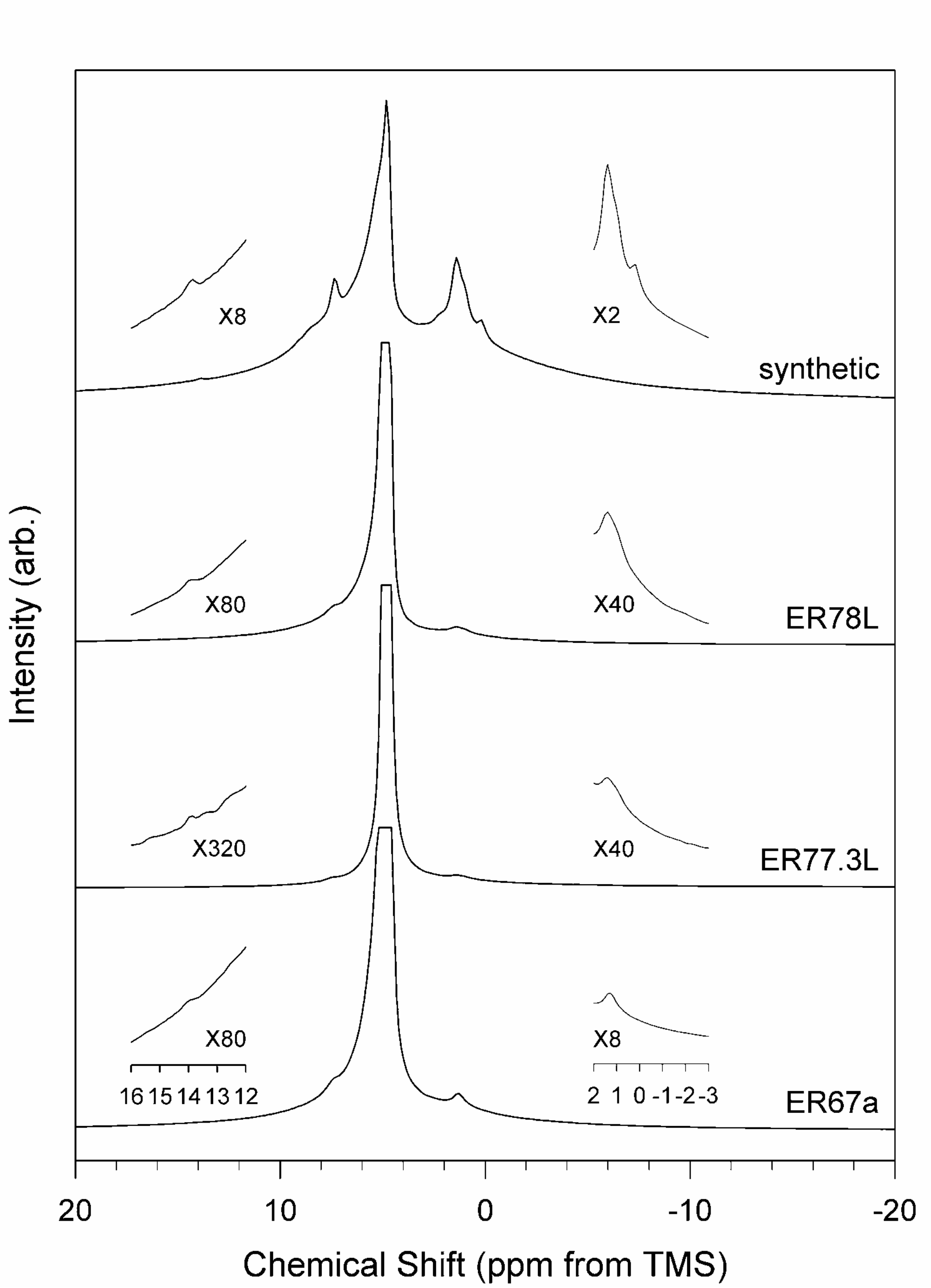

Figure 2.4. ^{1}H MAS NMR spectra of calcite speleothems and synthetic calcite/phosphate coprecipitate. Insets shown at expanded vertical scale to show the regions 16 to 12 ppm and 2 to -3 ppm. Each spectrum was collected with a relaxation delay of 10 s for 6 000 to 9 000 aquisitions.

III. The Nature of Phosphate in Coral Skeletal Aragonite

In Review at Earth and Planetary Science Letters
Harris E. Mason[1], Paolo Montagna[2,3], Marco Taviani[3], Malcolm McCulloch[4], Brian L. Phillips[1], The Nature of Phosphate in Coral Skeletal Aragonite, Earth Planet. Sci. Rev. (in review)

[1]*Department of Geosciences, Stony Brook University, Stony Brook, New York 11794-2100*
[2]*Istituto Superiore per la Protezione e la Ricerca Ambientale (ISPRA), Via Vitaliano Brancati 48, 00144 Rome, Italy*
[3]*Istituto di Scienze Marine (ISMAR), Consiglio Nazionale delle Ricerche (CNR), Via P. Gobetti 101, 40122 Bologna, Italy*
[4]*Research School of Earth Sciences, Australian National University, Canberra, ACT 200, Australia*

1. Abstract

Recent development of paleoproxies based on the P/Ca ratio in deep sea corals has illustrated the necessity for accurate geochemical models of P incorporation in aragonite based on reliable speciation data. Here we use single and double-resonance solid-state nuclear magnetic spectroscopy (NMR) to investigate the P speciation of these coral aragonites. These results indicate that the majority P is present as P contained as defects in the aragonite structure plus minor hydroxylapatite. Quantification of the amount of hydroxylapatite also reveals that its presence is not related to external environmental factors and can occur in differing abundances within the same corallite sample. Since few models are able to describe how crystalline phases can incorporate into carbonates careful examination is needed to select for samples which contain only P defects.

2. Keywords

coral, phosphate, aragonite, NMR spectroscopy, apatite, ^{1}H, ^{19}F

3. Introduction

Recently, it has been proposed that P/Ca ratios in the aragonite skeleton of deep-sea corals record the concentration of ambient dissolved inorganic phosphate (DIP), which combined with U-series chronology could prove to be a useful paleo-nutrient proxy [1-3]. The amount of bioavailable phosphate in the photic zone of the surface ocean serves as a limit to primary productivity in many ocean basins. Since export of biomass to deep-waters may act to drawdown atmospheric CO_2 [1, 3], knowledge of past oceanic P concentrations is important as can allow estimation of the contribution of the "biological pump" to the levels of atmospheric CO_2. Montagna et al. [1] noted that laser ablation inductively coupled plasma mass spectrometry (LA-ICPMS)-derived P/Ca ratios for aragonite septa from a variety of *Desmophyllum dianthus* coral samples were linearly related to the P concentration of the waters from which they were collected. This correlation was used to reconstruct paleo-nutrient data from a ~11 190 yr old sample. Unlike other trace elements used as paleo-environmental proxies, such as Ba, Sr and Cd, P cannot substitute simply into the aragonite crystal structure and its form in the coral aragonite is unknown. The P speciation can be reasonably expected to influence the relationship between DIP concentration and aragonite P/Ca.

Geochemical models of trace element incorporation into calcite and aragonite typically rely on incompatible incorporation of the trace element into defect sites in the carbonate crystal lattice [4-6]. P coprecipitation, sorption, and desorption studies at low P solution concentrations (<100 mM) and near neutral pH suggest that phosphate incorporation can be modeled by the sorption and incompatible incorporation of protonated phosphate groups [7-9]. It has also been shown in certain cases calcium phosphate surface precipitates can form at these low P concentrations which are subsequently encapsulated by continued crystal growth [10]. Few models account for the formation of P-rich precipitates, and models that could potentially explain this behavior based on either epitaxial crystal growth [11] or surface encapsulation [12, 13] have yet to be fully explored. Therefore, it appears in order to model the interactions of P in solution with calcite or aragonite it is necessary that phosphate incorporate as an incompatible structural constituent.

Using nuclear magnetic resonance (NMR) spectroscopy we show here that the majority of phosphorus in coral skeletal material occurs as phosphate defects in aragonite, but that some corals also contain crystalline hydroxylapatite. The occurrence and quantity of hydroxylapatite inclusions in the skeletal aragonite does not appear to correlate simply with any environmental factors. It is not understood how apatite inclusions are incorporated into skeletal aragonite so selecting samples containing P only as phosphate defects is likely to improve proxy relationship.

4. Materials and Methods

Subsamples of coral skeleton were selected from modern and subfossil corals with no evidences for any visible Fe-Mn-rich crust, checked under a binocular microscope and using thin sections under plane and cross-polarized light. No major visible alterations (e.g. diagenetic alteration or bioerosions) were evident.

The sampling methods were different according to the various coral species:

Desmophyllum dianthus and *Flabellum* sp.: pieces of septum were carefully removed from the S1 septa, the largest septa, by a diamond tipped saw attached to a dentist drill. Other subsamples were cut from the thecal wall and all the small fragments of septa attached to the theca were mechanically abraded away using the same saw. This allowed us to obtain samples representative of the thecal margin only.

Lophelia pertusa: pieces of the thecal wall were obtained cutting single corallites transversally. The part corresponding to the intersection between the wall and the septa (inside edge of the theca) was abraded and septa were completely removed.

Madrepora oculata: a piece of the coral was collected cutting a corallite transversally. This coral portion contains both the thecal wall and the septa ("whole coral" reported in the text).

Porites sp.: a small rectangular parallelepiped of coral was removed from a 7 mm slab previously obtained by cutting a coral core along the axis of growth. The subsample was taken at a distance of 12 cm from the top of the coral core in order to avoid the remnants of coral tissue.

Aragonite/phosphate coprecipitation was undertaken using a seeded constant addition method adapted from Zhong and Mucci [14] and described in Reeder et al [15]. The seeds were synthesized by pumping two solutions of 0.2 M $CaCl_2$ and 0.2 M Na_2CO_3 using a syringe pump at a rate of 300 μl/min into a constantly stirring initial solution containing 7 mM $CaCl_2$, 7 mM $NaHCO_3$, and 50 mM $MgCl_2$ which was being bubbled with air. Each solution contained 0.1 M $NaCl_2$ as background electrolyte. The aragonite seeds were analyzed by SEM for to determine the average dimensions and morphology of the crystallites produced and reveal on average blocky crystals 3 μm wide by 4 to 10 μm long grouped into 40 to 50 μm sized ball shaped clusters. For phosphate coprecipitation, the same procedure was used except 0.1 g of aragonite seed material was added to initial growth solution, the concentrations of reactants in the syringes were 0.1M and $NaHPO_4$ was added to the CO_3^{2-} syringe such that the phosphate concentration ranged from 50 to 100 μM. A 0.1 M $NaH^{13}CO_3$ solution replaced the Na_2CO_3 syringe to synthesize the ^{13}C-enriched sample. Periodically, solution was drawn from the growth solution to analyze total carbonate and reactive phosphate concentrations. At the end of 4 to 5 hrs of reaction time the solid was collected, filtered, dried for 2 hrs in a 60° C oven. Powder X-ray diffractions patterns of the samples indicate that in all cases aragonite dominated the final samples with some samples exhibiting only minor calcite impurities.

The ^{31}P single pulse magic angle spinning (SP/MAS) NMR and $^{31}P\{^1H\}$ cross polarization (CP) MAS NMR spectra were collected on a 400 MHz Varian Inova spectrometer at operating frequencies of 161.8 and 399.8 MHz for ^{31}P and ^1H, respectively. Samples were contained in 7.5 mm (o.d.) Si_3N_4 rotors and spun at 5 kHz. The probe and rotor assemblies yielded no detectable ^{31}P NMR signal after several days of acquisition. However, standard ZrO_2 based rotor sleeves can give ^{31}P signal in the orthophosphate region. The ^1H SP/MAS NMR and $^1H\{^{31}P\}$ rotational echo double resonance (REDOR) spectra were obtained using a Chemagnetics probe assembly configured for 4 mm (o.d.) rotors and modified to yield very low ^1H background signal. $^{31}P\{^1H\}$ Heteronuclear Correlation (HetCor) spectra were obtained using a probe configured for 3.2 mm (o.d.) rotors and collected as a total of 100 hypercomplex points in *t1* with a 10 μs increment corresponding to a 100 kHz spectral window in *t1*. A Carr-Purcell-Meiboom-Gill (CPMG) type acquisition was implemented to shorten the length of the HetCor experiment. $^{19}F\{^{31}P\}$ REDOR, $^{31}P\{^{13}C\}$ SP/REDOR, and $^1H \rightarrow {}^{31}P\{^{13}C\}$ CP/REDOR spectra were collected on a 500 MHz Varian Infinity Plus spectrometer at operating frequencies of 125.7, 202.3, 470.2, and 499.8 MHz for ^{13}C, ^{31}P, ^{19}F and ^1H respectively. $^{19}F\{^{31}P\}$ REDOR spectra were collected using a Varian/Chemagnetics T3-type probe configured for 3.2 mm (o.d.) rotors and to give a very low ^{19}F background. $^{13}P\{^{13}C\}$ SP and $^1H \rightarrow {}^{31}P\{^{13}C\}$ CP/REDOR spectra were collected using Varian HXY probe configured for 4 mm (o.d) rotors. The ^{31}P MAS NMR spectra are referenced with respect to 85% phosphoric acid using hydroxylapatite as a secondary reference set to 2.65 ppm. The ^{1}H MAS NMR spectra are referenced with respect to tetramethylsilane using hydroxylapatite as a secondary reference set to 0.2 ppm. ^{19}F spectra were referenced with respect to CCl_3F (C_6F_6 = 142. ppm).

5. Results and Discussion

We obtained solid-state ^{31}P NMR spectra for a variety of aragonitic azooxanthellate and zooxanthellate coral samples having P contents ranging from 17 to 319 ppm (Fig. 3.1; Table 3.1), including septa and thecal wall portions as well as whole coral samples. The ^{31}P{^{1}H} cross-polarization magic-angle spinning (CP/MAS) and ^{31}P single-pulse (SP) MAS spectra of a *Desmophyllum dianthus* septum (DD LM99-124) are presented in Figure 3.2 and illustrate the typical spectral profile observed for most samples. These spectra can be described by a sum of two Gaussian peaks centered at ^{31}P chemical shifts (δ_P) of 2.7 and 4.0 ppm which have full-widths at half maximum (fwhm) of 1.7 and 6.4 ppm, respectively. These peaks are easily separated in ^{31}P{^{1}H} CP/MAS spectra obtained with different contact times owing to their distinct CP kinetics. The peak at δ_P = 2.7 ppm (Fig. 3.2a) is dominant at long contact times due to a long relaxation time of associated ^{1}H ($T_{1\rho,H}$ > 10 ms) compared to that at δ_P = 4.0 ppm ($T_{1\rho,H}$ = 1 ms). Based on its narrow width, CP behavior and chemical shift, we assign the peak at δ_P = 2.7 ppm to crystalline apatite[16-18]. The broad peak at δ_P = 4.0 ppm dominates at short contact times (Fig. 3.2c) because of its much faster $^{1}H \rightarrow {}^{31}P$ CP rate (T_{PH} = 0.4 ms). This behavior indicates a close association with rigid ^{1}H. The two peaks fit to the CP/MAS spectra also describe the quantitative SP spectra, indicating that they represent the P distribution in the sample. With few exceptions the spectra of the other deep sea corals are similar, differing only in the total P content and proportion of apatite.

A broad peak near δ_P = 4 ppm that is similar in both chemical shift and width to the broad peak observed for the coral samples dominates ^{31}P NMR spectra of synthetic aragonite precipitated from solutions containing 1 - 3 μM DIP (Fig. 3.1g-h). The samples range in P concentration from 125 to 700 ppm but their NMR spectra showed no significant differences. The ^{31}P CP/MAS spectra of the aragonite/phosphate coprecipitates also contain small narrow peaks at δ_P = 11.4 and 8.4 ppm that are not present in the spectra of coralline aragonite nor in quantitative ^{31}P SP/MAS spectra (Fig. 3.1h), suggesting they arise from minor protonated phosphate species possibly in unidentified crystalline phases. No peak for apatite was observed for any synthetic sample. The similarity of the broad peak near $\delta_P = 4$ ppm in spectra of coral aragonite to that from synthetic aragonite/phosphate coprecipitates suggests that most of the P present in corals occurs as inorganic phosphate.

This interpretation is supported by ^{1}H NMR spectra of the H associated with P, which are consistent with hydrogen phosphate and molecular water. The ^{31}P-detected ^{1}H spectra were obtained by two-dimensional ^{31}P{^{1}H} HetCor methods. The ^{1}H spectrum for a sample containing no P as apatite (DD G16505 S) shows a narrow peak at $\delta_H = 5.5$ ppm that is underlain by a broad peak at 7.5 ppm (8.2 ppm fwhm) with a broad spinning sideband pattern (Fig. 3.3). Neither of these peaks occurs in the range expected for aliphatic H in organophosphates [19] but are consistent with molecular water and weakly H-bonded hydrogen phosphate. Furthermore, the inorganic aragonite/phosphate coprecipitate yielded a very similar ^{31}P-detected ^{1}H spectrum (Fig. 3.3b) containing essentially the same peaks in the same positions (a narrow peak at 6.1 ppm and a broader peak at 8.4 ppm).

The ^{31}P and ^{1}H NMR data are fully consistent with the presence of P mainly as inorganic phosphate in the aragonite structure or as amorphous calcium phosphates since the latter yield similar spectra. [19, 20] A test for the presence of phosphate as defects in the aragonite structure is provided by ^{31}P{^{13}C} REDOR NMR experiments on a ^{13}C-enriched synthetic aragonite/phosphate coprecipitate (Fig. 3.3). This experiment consists of two spectra, a control spectrum (S_0; Fig. 3.4a,c) containing signal from all ^{31}P in the sample and a REDOR spectrum (S; Fig. 3.4b,d) in which a reduction in signal intensity relative to S_0 occurs for ^{31}P species near ^{13}C. Simulations of the REDOR experiment indicate that no significant effect is expected for P located farther than 5 Å from ^{13}C. The results at 6.7 ms REDOR dephasing period show a large REDOR fraction [$(S_0-S)/S_0$] of 0.7 for the peak near $\delta_P = 4$ ppm. This value is somewhat lower than SPINEVOLUTION [21] simulated REDOR fractions corresponding to P located 3.2 Å from 6 C (Fig. 3.5), 0.90 at 6.7 ms. This difference is likely due to a combination of pulse imperfections, incomplete excitation of the sample contained at the ends of the rotor, and a disrupted structure near the defect leading to fewer adjacent C or C-P distances larger than the C-C distances of aragonite. Similar results were obtained with both SP and CP excitation of ^{31}P and taken overall these data indicate that the P corresponding to the broad peak near 4 ppm arises from phosphate in the carbonate phase.

Additional $^{1}H\{^{31}P\}$ and $^{19}F\{^{31}P\}$ REDOR NMR experiments were used to determine the origin of the crystalline apatite inclusions that occur in some natural specimens. Fluorapatite is a significant sink for phosphate in marine sediments [22] whereas biogenic apatite is composed primarily of carbonate-substituted hydroxylapatite [20]. The ^{19}F NMR spectrum for the *Flabellum* sp. theca sample is complex with multiple peaks, none of which can be assigned nor correspond to previous data for fluorapatite. No $^{19}F\{^{31}P\}$ REDOR effect was observed for any ^{19}F peak, further indicating that the apatite is not fluorapatite (Fig. 3.6). The $^{1}H\{^{31}P\}$ REDOR data (Fig. 3.7) were obtained for a *Desmophyllum dianthus* theca wall sample (DD CHILE Coral A). The control spectrum contains large peaks at δ_H = 4.8 and 1.5 ppm that do not decrease in the REDOR spectrum and which correspond well to water molecules and OH in the calcium carbonate phase [23]. A very small peak is observed at δ_H = 0.2 ppm that is similar in chemical shift to that for hydroxylapatite,[24] which is absent from the REDOR spectrum, indicating proximity to P. These observations are consistent with observation of the narrow peak in $^{31}P\{^{1}H\}$ CP spectra and its assignment to hydroxylapatite. Hydroxylapatite can also contain significant amounts of F, however, the hydroxyl peak would be expected to occur at a more positive chemical shift of about 1.2 to 1.4 ppm [24].

Since acquisition of quantitative ^{31}P NMR spectra are extremely time-consuming, and impractical at P contents less than about 200 ppm, we developed a relationship between relative intensities in ^{31}P SP/MAS and $^{31}P\{^{1}H\}$ CP/MAS spectra as a means to estimate the proportion of hydroxylapatite. Ideally the abundances of the two peaks at 2.6 and 3.8 ppm would be derived through the careful integration of ^{31}P single-pulse (SP) MAS NMR spectra. However, the low abundance of P in the samples and the long experimental pulse delays (100s of seconds) need for quantitative results required at times almost 4 days of continuous spectrometer time. Conversely, a $^{31}P\{^{1}H\}$ CP/MAS NMR spectrum takes nearly half the time to collect with the same signal to noise of the SP. The results of a CP/MAS experiment are not quantitative without significant experimentation and analysis of CP kinetics [25]. Therefore a method for deriving the relative percentages of apatite in the aragonic coral skeletons was developed through a similar correlation as proposed in Mason et al. [10]. The relative intensities for ^{31}P SP/MAS and $^{31}P\{^{1}H\}$ CP/MAS spectra of a sample which contained a higher relative amount of P in the aragonite (*Desmophyllum dianthus* septa sample; DD LM99 124) were compared used to develop a correlation between the normalized intensities of subsequent CP/MAS NMR spectra collected under the same conditions.

Combining these results with absolute P-contents from LA-ICPMS data on the same sample the amount of hydroxylapatite can be obtained (Table 3.1). The result is a wide range of hydroxylapatite contents appearing unrelated to environmental factors such as depth and dissolved inorganic phosphate. Nor do the concentrations of hydroxylapatite do not correlate with absolute P concentration of the skeletal aragonite. Moreover, there seems to be no clear correlation between the apatite content and the preservation state of the corals (i.e. alive or fossil). For example, DD G16505 TW contains only 17.27 ppm P but 31% of which occurs in hydroxylapatite.

Two other samples we examined have P distributions that differ from those of the other deep-sea coral species. Spectra of a *Madrepora oculata* sample (MO CORAL2 75) contain a broad peak near $\delta_P = 4$ ppm plus a narrow peak at -0.6 ppm (1.1 ppm fwhm) (Fig. 3.1i). The peak at -0.6 ppm could arise from a crystalline inorganic phosphate phase[10, 17, 18], or phosphate esters which have been reported in this range,[26] but usually give broader peaks. The origin of this peak was not investigated further, but its presence illustrates that other P-containing components could be present in coralline aragonite. The *Porites* sp. (PO FR2004) sample also yields spectra containing a broad peak near 4 ppm (Fig. 3.1j) but also an additional peak at $\delta_P = 22.5$ ppm (3.0 ppm fwhm), that is consistent with the presence of phosphonates [14-16] These two specimens are both whole corallite specimens and the possibility exists that the samples include areas containing remnant cellular material from either the coral polyp or endolithic algae, although phosphonates are also known to be adsorbed strongly to calcite surface [27] and could be occluded during crystal growth.

A robust relationship between P content of coral aragonite and DIP suitable for use as a paleo-proxy would seem possible only if P occurs as phosphate defects in the aragonite structure. Simple trace element partitioning models developed for inorganic carbonates have been applied to coralline systems[4, 5, 28], because the coral polyp precipitates aragonite extra-cellularly between the polyp and older skeletal aragonite from seawater that is brought in through the vacuoles and supersaturated through transport of Ca^{2+} and H^+ [6]. At least three processes could lead to P incorporation in coralline aragonite, including encapsulation of surface precipitates, occlusion of organic matter, and coprecipitation of dissolved inorganic phosphate as defects in the aragonite. Of these, only in the latter could it be expected that equilibrium is established between surface sorbed phosphate and the aqueous phase as required for a linear partition coefficient[29, 30]. Standard methodology used for paleo-proxy development such as LA-ICPMS and x-ray adsorption spectroscopy (XAS) cannot yet provide the molecular-scale spatial relationships between P and carbonate necessary to test whether P incorporates as inorganic defects. Although based on a limited number of samples, our results strongly suggest that coprecipitation of phosphate is the dominant origin of P in most deep-water corals, and support the use of P content as a proxy. However, many deep-sea corals also contain significant amounts of apatite that could cause systematic error, but which is easily detected using the methods described here. Taking into account the non-carbonatic contaminations by carefully selecting the coral portion to be analysed it will be eventually possible to obtain a more robust P/Ca vs. DIP calibration, useful for paleo-nutrient reconstructions.

6. Acknowledgments

This research was supported by the Center for Environmental Molecular Science, which is funded by the U.S. NSF (CHE-0221934), and instrumentation provided by NSF CHE-03-21001. Coral collection was funded by CNR grants, ESF Moundforce and EU Hermes projects; Bruno Briano (Savona, Italy) and Günter Försterra kindly supplied corals from offshore Madagascar and the Chilean fiords, respectively. Ship time of RV Urania provided by CNR is gratefully acknowledged. This is IGM scientific contribution n.xxxx. H.M. was supported through a U.S. Dept. of Education sponsored GAANN fellowship (P200A060248).

7. References

[1] P. Montagna, M. McCulloch, M. Taviani, C. Mazzoli, B. Vendrell, Phosphorus in cold-water corals as a proxy for seawater nutrient chemistry, Science 312(2006) 1788-1791.

[2] M. LaVinge, M.P. Field, E. Anagnostou, A.G. Grottoli, G.M. Wellington, R.M. Sherrell, Skeletal P/Ca tracks upwelling in Gulf of Panama coral: Evidence for a new seawater phosphate proxy, Geophys. Res. Lett. 35(2008) L05604.

[3] E. Anagnostou, R.M. Sherrell, J.F. Adkins, A.C. Gagnon, Phosphorus, barium and boron in the deep-sea coral Desmophyllum dianthus: Preliminary calibrations, Geochim. Cosmochim. Acta 71(2007) A22.

[4] A.C. Gagnon, J.F. Adkins, D.P. Fernandez, L.F. Robinson, Sr/Ca and Mg/Ca vital effects correlated with skeletal architecture in a scleractinian deep-sea coral and the role of Rayleigh fractionation, Earth Planet. Sc. Lett. 261(2007) 280-295.

[5] G.A. Gaetani, A.L. Cohen, Element partitioning during precipitation of aragonite from seawater: A framework for understanding paleoproxies (vol 70, pg 4617, 2006), Geochim. Cosmochim. Acta 71(2007) 530-530.

[6] A.L. Cohen, T.A. McConnaughey, Geochemical perspectives on coral mineralization, Biomineralization 54(2003) 151-187.

[7] W.A. House, L. Donaldson, Adsorption and Coprecipitation of Phosphate on Calcite, J. Colliod Interf. Sci. 112(1986) 309-324.

[8] Z.R. Hinedi, S. Goldberg, A.C. Chang, J.P. Yesinowski, A ^{31}P and ^{1}H MAS NMR-Study of Phosphate Sorption onto Calcium-Carbonate, J. Colliod Interf. Sci. 152(1992) 141-160.

[9] F. Millero, F. Huang, X.R. Zhu, X.W. Liu, J.Z. Zhang, Adsorption and desorption of phosphate on calcite and aragonite in seawater, Aquat. Geochem. 7(2001) 33-56.

[10] H.E. Mason, S. Frisia, Y. Tang, R.J. Reeder, B.L. Phillips, Phosphorus speciation in calcite speleothems determined from solid-state NMR spectroscopy, Earth Planet. Sc. Lett. 254(2007) 313-322.

[11] P.G. Koutsoukos, G.H. Nancollas, Crystal-Growth of Calcium Phosphates - Epitaxial Considerations, J. Cryst. Growth 53(1981) 10-19.

[12] E.B. Watson, A conceptual model for near-surface kinetic controls on the trace-element and stable isotope composition of abiogenic calcite crystals, Geochim. Cosmochim. Acta 68(2004) 1473-1488.

[13] E.A. Burton, L.M. Walter, The Role of pH in Phosphate Inhibition of Calcite and Aragonite Precipitation Rates in Seawater, Geochim. Cosmochim. Acta 54(1990) 797-808.

[14] S.J. Zhong, A. Mucci, Calcite Precipitation in Seawater Using a Constant Addition Technique - a New Overall Reaction Kinetic Expression, Geochim. Cosmochim. Acta 57(1993) 1409-1417.

[15] R.J. Reeder, M. Nugent, G.M. Lamble, C.D. Tait, D.E. Morris, Uranyl incorporation into calcite and aragonite: XAFS and luminescence studies, Environ. Sci. Technol. 34(2000) 638-644.

[16] A. Kaflak, D. Chmielewski, A. Gorecki, A. Slorarczyk, W. Kolodziejski, Efficiency of $^{1}H \rightarrow ^{31}P$ cross-polarization in bone apatite and its mineral standards, Solid State Nucl. Magn. Reson. 29(2006) 345-348.

[17] W.P. Rothwell, J.S. Waugh, J.P. Yesinowski, High-Resolution Variable-Temperature ^{31}P NMR of Solid Calcium Phosphates, J. Am. Chem. Soc. 102(1980) 2637-2643.

[18] P.S. Belton, R.K. Harris, P.J. Wilkes, Solid-State ^{31}P NMR-Studies of Synthetic Inorganic Calcium Phosphates, J. Phys. Chem. Solids 49(1988) 21-27.

[19] A. Teleman, P. Richard, M. Toivari, M. Penttilla, Identification and quantitation of phosphorus metabolites in yeast neutral pH extracts by nuclear magnetic resonance spectroscopy, Anal. Biochem. 272(1999) 71-79.

[20] J.C. Elliott, Calcium Phosphate Biominerals, Rev. Mineral. Geochem. 48(2002) 427-453.

[21] M. Veshtort, R.G. Griffin, SPINEVOLUTION: A powerful tool for the simulation of solid and liquid state NMR experiments, J. Magn. Reson. 178(2006) 248-282.

[22] D. Kim, J.D. Schuffert, M. Kastner, Francolite authigenesis in California continental slope sediments and its implications for the marine P cycle, Geochim. Cosmochim. Acta 63(1999) 3477-3485.

[23] S.J. Gaffey, H_2O and OH in Echinoid Calcite - a Spectroscopic Study, Am. Mineral. 80(1995) 947-959.

[24] J.P. Yesinowski, H. Eckert, Hydrogen Environments in Calcium Phosphates - ^{1}H MAS NMR at High Spinning Speeds, J. Am. Chem. Soc. 109(1987) 6274-6282.

[25] W. Kolodziejski, J. Klinowski, Kinetics of cross-polarization in solid-state NMR: A guide for chemists, Chem. Rev. 102(2002) 613-628.

[26] B.J. Cade-Menun, Characterizing phosphorus in environmental and agricultural samples by ^{31}P nuclear magnetic resonance spectroscopy, Talanta 66(2005) 359-371.

[27] A.T. Kan, G.M. Fu, M.B. Tomson, Adsorption and precipitation of an aminoalkylphosphonate onto calcite, J. Colliod Interf. Sci. 281(2005) 275-284.

[28] D.J. Sinclair, M.J. Risk, A numerical model of trace-element coprecipitation in a physicochemical calcification system: Application to coral biomineralization and trace-element 'vital effects', Geochim. Cosmochim. Acta 70(2006) 3855-3868.

[29] E. Curti, Coprecipitation of radionuclides with calcite: estimation of partition coefficients based on a review of laboratory investigations and geochemical data, Appl.Geochem. 14(1999) 433-445.

[30] J.D. Rimstidt, A. Balog, J. Webb, Distribution of trace elements between carbonate minerals and aqueous solutions, Geochim. Cosmochim. Acta 62(1998) 1851-1863.

Tables

Table 3.1. Coral samples studied by ^{31}P NMR, including the location, depth, and dissolved inorganic phosphate concentration of waters in which sample grew at the time of collection. Percentage of the total P contained in apatite (% P_{Ap}) was estimated by NMR (Supplemental information). All corals were live at the time of collection unless otherwise indicated.

Name	**Genus**	**Portion**	**location**	**depth (m)**	**DIP (μM)**	**[P] in solid (ppm)**	**%P_{Ap}**	**$[P]_{Ap}$ (ppm)**
DD LM99-124	*Desmophyllum* (fossil)	Septa	Tyrrhenian Sea	377-411	1.8-2.0	119.2±59.72	35(5)	41.7
DD CHILE CoralA	*Desmophyllum*	Theca	Chilean Fjords	30	1.78±0.36	No Data	41(7)	N/A
DD G16505 S	*Desmophyllum*	Septa	Western Pacific	406	1.26±0.18	202.02±55.53	0	0
DD G16505 TW	*Desmophyllum*	Theca	Western Pacific	406	1.26±0.18	17.27±4.99	31(5)	5.4
F MAD S	*Flabellum*	Septa	Madagascar	800-1000	1.99-2.35	86.65±21.14	0	0
F MAD TW	*Flabellum*	Theca	Madagascar	800-1000	1.99-2.35	54.67±11.27	34(5)	18.6
DD CHILE S	*Desmophyllum*	Septa	Chilean Fjords	30	1.78±0.36	318.73±78.61	8.3(9)	26.5
DD CHILE TW	*Desmophyllum*	Theca	Chilean Fjords	30	1.78±0.36	35±7.6	0	0
LP CORAL2 75	*Lophelia*	Theca	Ionian Sea	828-818	0.26±0.01	32±12	15(3)	4.8
LP COBAS 109	*Lophelia* (fossil)	Theca	Baleares Islands	366	No Data	106.04±18.93	0	0
MO CORAL2 75	*Madrepora*	ThecaWhole coral	Ionian Sea	828-818	0.26±0.01	No Data	0	N/A
PO FR2004	*Porites*	Whole coral	Fitsroy Reef (Great Barrier Reef)	5	0.12-0.15	35.7±11.4	0	0

Figures and Captions

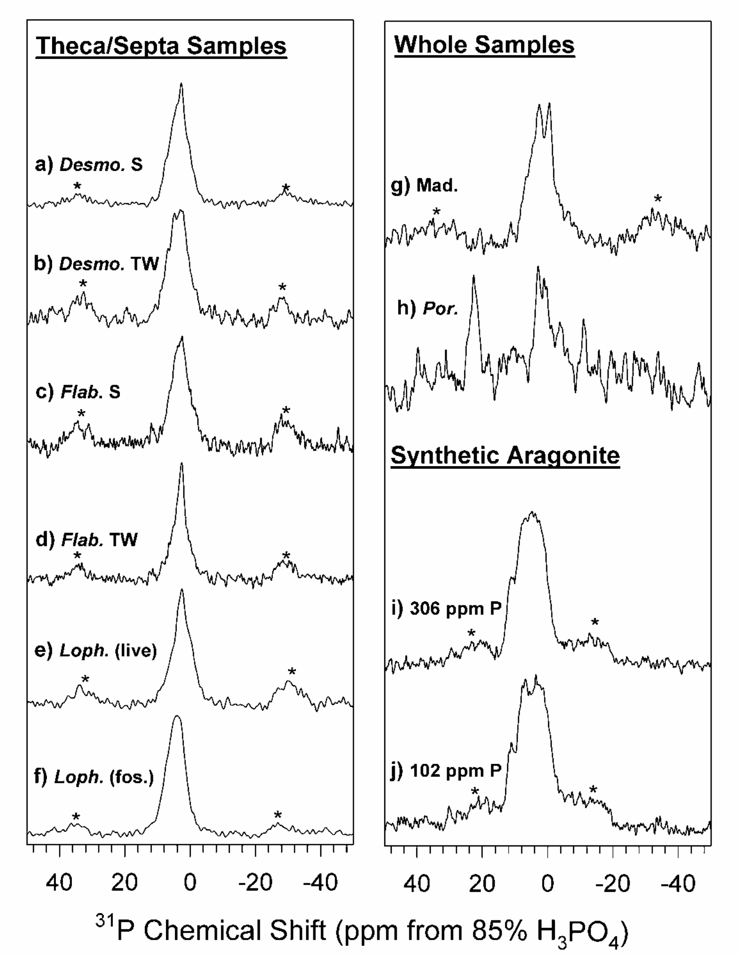

Figure 3.1. ^{31}P NMR spectra for coral aragonite and aragonite/phosphate coprecipitate samples. **a-f)** $^{31}P\{^1H\}$ CP/MAS NMR spectra of coral septa and thecal wall aragonite **a)** septa and **b)** thecal wall of *Desmophyllum dianthus* (DD CHILE) **c)** septa and **d)** thecal wall of *Flabellum sp.* (F MAD) **e)** live collected (LP CORAL2 75) and **f)** fossil (LP COBAS 109) samples of *Lophelia pertusa* thecal wall **g)** $^{31}P\{^1H\}$ CP/MAS and **h)** ^{31}P SP/MAS spectra of aragonite/phosphate coprecipitate containing 650 ppm P. **i-j)** $^{31}P\{^1H\}$ CP/MAS spectra of whole coral samples *Madrepora oculata* (MO CORAL2 75) and *Porites sp.* (PO FR2004), respectively. All spectra obtained using a spinning rate of 5 kHz, 2 ms CP contact time, and 2 s pulse delay except **g)** 2 ms CP contact time, 2 s pulse delay and a spinning rate of 3 kHz, and **h)** 10 kHz spinning rate and 120 s pulse delay. Asterisks mark the location of spinning sidebands.

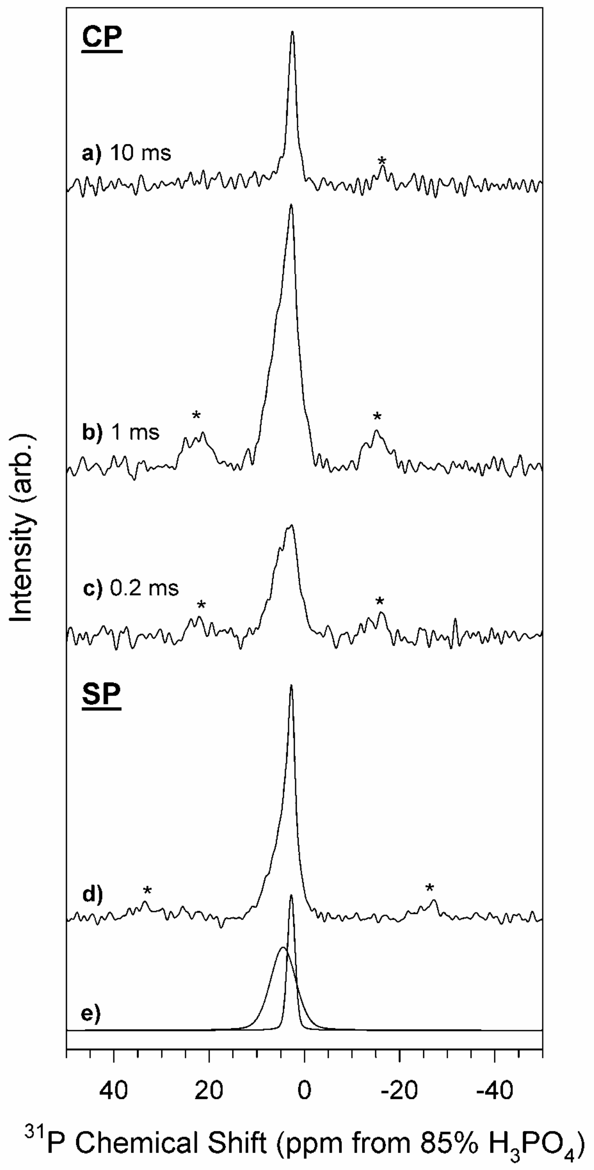

Figure 3.2. ^{31}P MAS NMR spectra collected of *Desmophyllum dianthus* coral septa (DD LM99 124) from the Tyrrhenian Sea. **a-c)** ^{31}P{^{1}H} CP/MAS NMR spectra collected at a 3 kHz spinning rate and 2 s pulse delay for 4672 acquisitions using contact times of **a)** 10 ms, **b)** 1 ms, and **c)** 0.2 ms. **d)** ^{31}P SP/MAS NMR spectrum obtained with a 5 kHz spinning rate and 120 s pulse delay for 819 acquisitions. **e)** Components of the least squares fit to the spectrum shown in **d),** vertically offset for clarity.

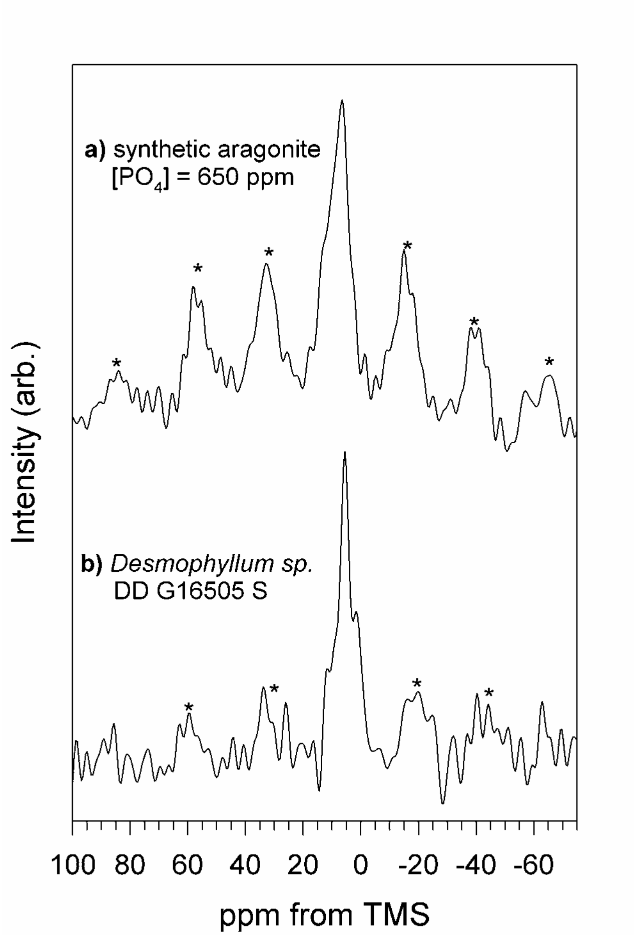

Figure 3.3. ^{31}P-detected ^{1}H MAS/NMR obtained from summed projections of 2-d ^{31}P{^{1}H} CPMG HetCor data for **a)** synthetic and **b)** Desmophyllum coral sample DD G16505 S. Both were collected at 2 ms contact time and 10 kHz spinning rate. Asterisks mark the location of spinning sidebands.

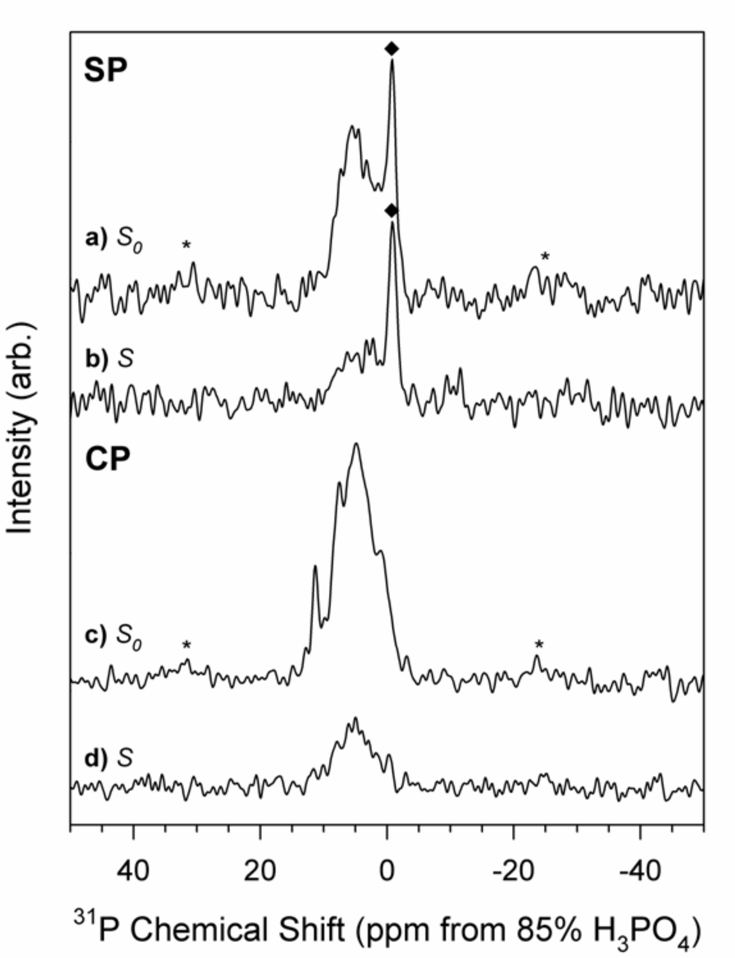

Figure 3.4. $^{31}P\{^{13}C\}$ REDOR NMR spectral sets for ^{13}C-enriched aragonite coprecipitated with phosphate collected at a 6 kHz spinning rate and 6.7 ms dephasing period. **SP:** Standard SP/REDOR, **CP:** CP/REDOR with 2 ms $^{31}P\{^{1}H\}$ CP preparation. **a, d)** Echo control spectra (S_0) **b, c)** $^{31}P\{^{13}C\}$ REDOR spectra (S). Diamonds denote background signal from rotor and asterisks mark the location of spinning sidebands.

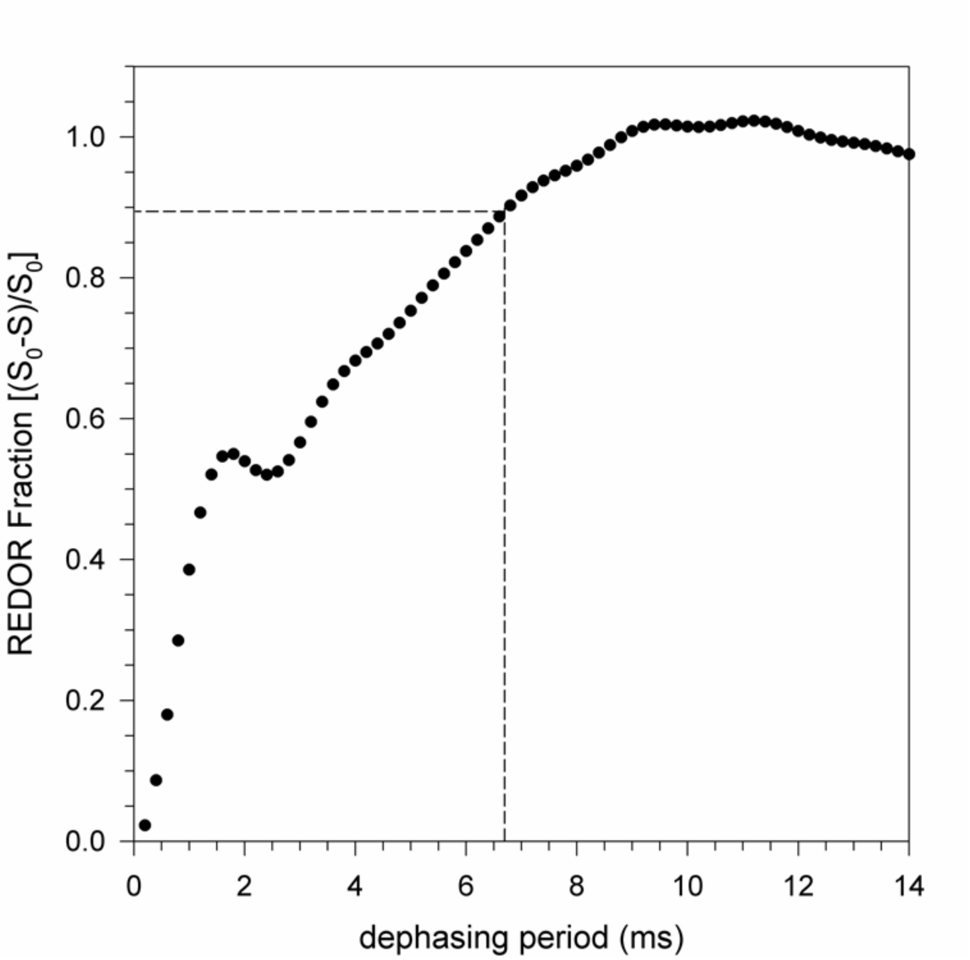

Figure 3.5. SPINEVOLUTION Simulated $^{31}P\{^{13}C\}$ REDOR curve for a ^{31}P surrounded by 6 ^{13}C at a distance of 3.2 Å. Dashed line occurs at the dephasing period where experimental data is reported.

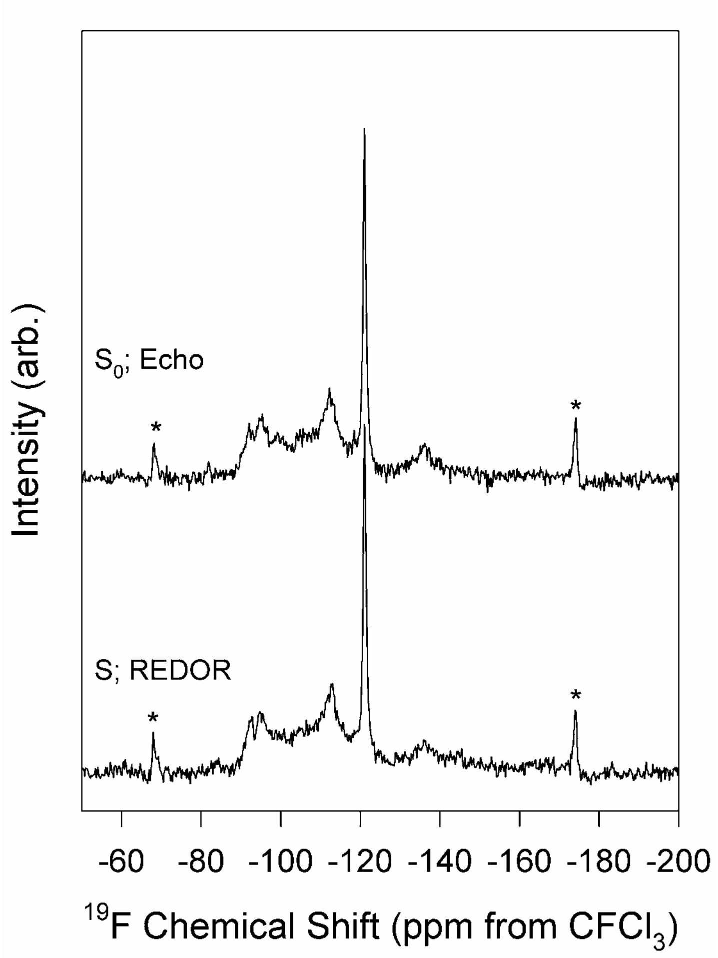

Figure 3.6. $^{19}F\{^{31}P\}$ REDOR NMR spectra collected for the *Flabellum sp.* theca sample (F MAD S) collected at a spinning rate of 25 kHz, a 100 s pulse delay, and 1.28 ms dephasing period for 1488 acquisitions. **Top**: ^{19}F Spin-echo control spectrum (S_0) **Bottom**: $^{19}F\{^{31}P\}$ REDOR spectrum (*S*). Asterisks mark the location of spinning sidebands

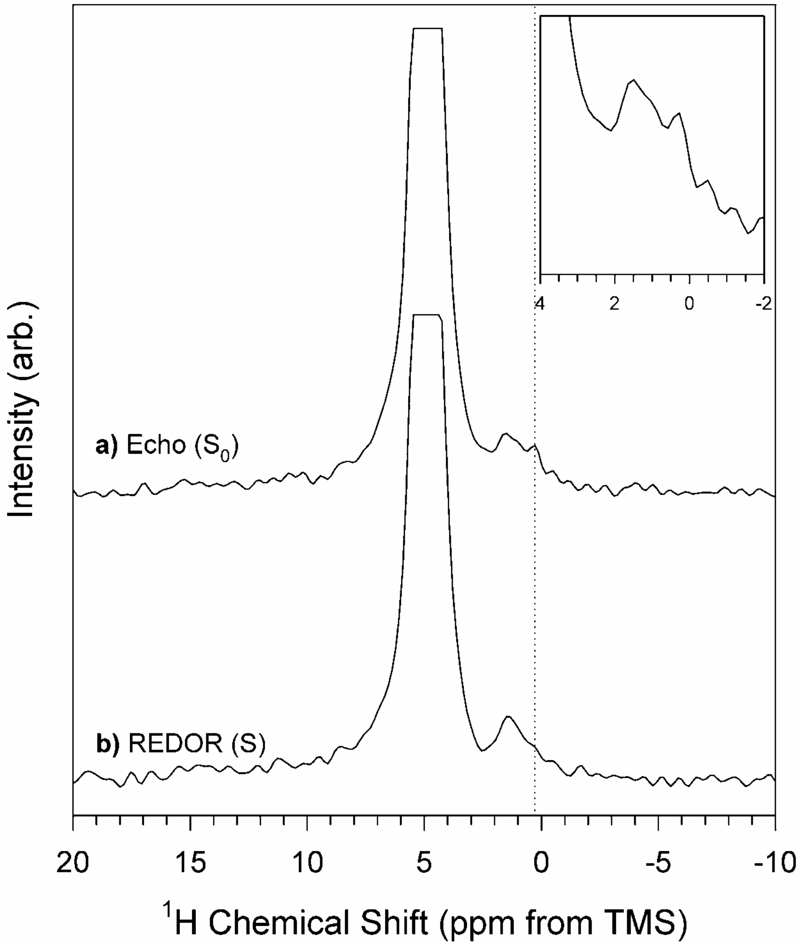

Figure 3.7. ^{1}H{^{31}P} REDOR NMR spectra for a *Desmophyllum dianthus* (DD CHILE CoralA) sample collected at a spinning rate of 15 kHz, pulse delay of 2 s, and dephasing period of 4.4 ms for 62 928 aquisitions. Spectra are shown at 5 times vertical exaggeration and truncated. a) ^{1}H{^{31}P} Spin-echo control spectrum (S_0) b) ^{1}H{^{31}P} REDOR spectrum (S). Dotted line illustrates the position of the peak at 0.2 ppm in the Spin-echo control spectrum. Inset: Expanded view Spin-echo control spectra over the range of 4 to -2 ppm.

IV. Solid-State NMR Study of the Role of H and Na in AB-type Carbonate Hydroxylapatite

Published with permission from Chemistry of Materials
Harris E. Mason[a,b,], Andrew Kozlowski[a,c], Brian L. Phillips[a,b], Solid-State NMR Study of the Role of H and Na in AB-type Carbonate Hydroxylapatite, Chem. Mater. 20(2008) 294-302, doi: 10.1021/cm0716598*

[a] *Center for Environmental Molecular Science, State University of New York, Stony Brook, New York, 11794-2100*
[b] *Department of Geosciences, State University of New York, Stony Brook, NY, 11794-2100*
[c] *Department of Chemistry, St. Lawrence University, Canton, NY 13617*

1. Abstract

Solid-State Nuclear Magnetic Resonance (NMR) techniques, combined with Fourier Transform Infrared (FT-IR) spectroscopy, were used to study synthetic AB-type carbonate hydroxylapatite (CHAp). $^{13}C\{^1H\}$ double resonance experiments indicate that the two carbonate environments represented by the peaks at $\delta_{C\text{-}13}$ = 169.8 and 170.8 ppm are associated with three H environments with one environment represented by a peak centered about $\delta_{H\text{-}1}$ = 0.0 ppm and two additional peaks located at 1.3 and 5.5 ppm. The peaks about $\delta_{H\text{-}1}$ = 0.0 ppm correspond to hydroxyl environments within the channels of the CHAp, whereas these at 1.3 and 5.5 exhibit spectral characteristics consistent with bicarbonate ions that donate moderate to weak hydrogen bonds. The carbonate-associated H appears to represent only a small fraction of H environments present. The broad range of H-bonding environments indicated by NMR likely prevents easy detection of protonated carbonate by FT-IR spectroscopy. Possible methods by which bicarbonate incorporation can be accommodated by the apatite structure are discussed. The Na/carbonate ratio and ^{23}Na NMR spectroscopy indicate that Na plays an important role in the carbonate incorporation in these materials.

2. Introduction

Carbonate-containing hydroxylapatite (CHap) has been the subject of numerous studies spanning a broad range of disciplines. This material is of interest to the medical and dental fields because the inorganic component of teeth and bones is best described by nanometer sized particles of hydroxylapatite containing significant concentrations of carbonate impurity (~ 8 wt%).[1] CHAp has also been studied with relevance to the fields of both material sciences and geochemistry due to the changes in reactivity and solubility of hydroxylapatite when carbonate is present as a trace anion.[2] Bone apatite is commonly used in permeable reactive barriers and has been shown to effectively sequester heavy metal cations and radionuclides.[3, 4] It is, therefore, important to understand how carbonate is incorporated in apatite and what accommodations must be made in order for it to successfully integrate within the apatite structure.

Previous studies have shown that two principal modes of carbonate substitution can exist within the apatite structure. The first substitution mechanism (A-site substitution) involves the replacement of channel site hydroxyl ions with carbonate. The second mechanism (B-site substitution) corresponds to the carbonate replacing a phosphate group.[2, 5] While pure phases containing only A-type substitution or B-type substitution have been successfully synthesized,[6, 7] CHAp can also be produced which contains substitution in both the A and B sites denoted as AB-type CHAp[8, 9]. While all CHAp phases have been synthesized in aqueous systems[1, 5, 7, 10], many studies produce CHAp under high-temperature, high pressure conditions in order to produce crystals suitable for X-ray and neutron diffraction studies.[6, 9, 11-13] Recently, Fleet and Liu[9], suggested that in sodium-bearing AB-type CHAp the A and B carbonate substitutions were coupled through substitutions in neighboring A and B sites. They noted that structural refinements gave O···O distances between O in the A-type carbonate group and O in phosphate tetrahedron that were too short which they interpreted to indicated B-type substitution in the neighboring PO_4 site.

The A and B-type carbonate substitutions in CHAp can be distinguished by Fourier Transform Infrared (FT-IR) spectroscopy. These substitutions give a distinct splitting in the υ_3 carbonate mode where A and B-type yield distinct peaks at 880 and 875 cm^{-1} respectively.[5, 11, 13] Additionally, differences in the υ_2 region from 1545 to 1410 cm^{-1} have been also used to differentiate these substitution sites.[11] Recently, however, Fleet and

Liu[9] have indicated that the presence of sodium significantly changes the shape of the υ_2 region in AB-type CHAp compared to that of sodium-free AB-type CHAp.

Solid-State Nuclear Magnetic Resonance (NMR) has also been employed in these systems to show the difference between the A and B sites in the apatites.[7, 12] Beshah et al[7] studied the system using $^{13}C\{^1H\}$ Cross Polarization Magic Angle Spinning (CP/MAS) NMR and showed that A-type CHAp gives a well-defined, narrow peak at about δ_{C-13} = 166.5 ppm, B-type CHAp gives a broad, asymmetric peak centered at about 170.2 ppm, and AB-type CHAp produces a complex lineshape containing a peak at 168.2 ppm in addition to the two peaks at the same position for A and B-type CHAp. Using dipolar suppression techniques and heat treatment, the complex lineshape observed in the AB-type CHAp was attributed to be the result of combination of A-type, B-type and a disordered carbonate species in contact with water adsorbed onto the surface.

In this study we have prepared synthetic samples of AB-type carbonate hydroxylapatites (CHAp) under aqueous conditions (90º C) and have characterized the substitutions using Fourier transform infrared (FT-IR) spectroscopy, Raman Spectroscopy, and a variety of one- and two-dimensional solid-state Nuclear Magnetic Resonance (NMR) spectroscopic techniques. These data indicate that two carbonate sites exist within the CHAp which are coupled to distinct H environments. We also provide evidence for the incorporation of hydrogen carbonate species into the CHAp structure. These results show that H as well as Na play a role in accommodating carbonate in the apatite structure.

3. Experimental Section

3.1. Sample Synthesis

A series of samples of AB-type CHAp were synthesized using a method adapted from Nelson and Featherstone[5] (Table 4.1). An initial CHAp (AK-2) was precipitated from aqueous solution by adding 40 ml of a solution containing 0.189 M of ammonium hydrogen phosphate and 0.588 M sodium bicarbonate at a rate of 0.55 ml/min to 40 ml of a continuously stirred 0.212 M calcium nitrate solution under a nitrogen atmosphere at 90º C. The pH of the reaction was maintained between 8.5 and 9.5 by periodic manual additions of small amounts of 10 N NaOH. The precipitate was collected, centrifuged, rinsed in deionized water, and dried in an oven at 100° C for 14 hrs. A portion of this sample was then placed in a PTFE-lined hydrothermal vessel with a solution containing 1M sodium bicarbonate and heated 200º C under autogenous pressure for two days in an attempt to increase the crystallinity of the sample (AK-2H). This same method was used to prepare a partially dueterated sample (AK-2HD) from the AK-2H sample where the sodium bicarbonate solution in the hydrothermal vessel was prepared in 98% D_2O.

Additional samples of aqueous precipitated (AK-4) and hydrothermally treated (AK-5H) CHAp were prepared following the same methods as above but using solutions containing ^{13}C-enriched sodium bicarbonate. AK-4 was vacuumed filtered, washed with acetone and allowed to dry in a 100º C oven for 30 min. AK-5H was collected, centrifuged, washed with DI water and allowed to dry in a dessicator at room temperature for 18 hrs. While collection methods differed for these samples no major differences were observed in the XRD patterns of these samples from those which were otherwise prepared.

3.2. Analytical Methods

Elemental analysis for Na, Ca, and P were done using a Beckman Spectraspan SSUU Direct Current Plasma Emission Spectrometer on portions of the AK-4 and AK-5H samples dissolved in a 23 mM HCl solution. Standards were prepared to mimic the compositions of the sample solutions to minimize matrix effects in the analysis. Carbonate content of the samples was estimated from correlations between Raman spectral features and carbonate content developed by Krajewski.[14]

X-ray powder diffraction (XRD) patterns were collected using a Scintag PADX powder X-ray diffractometer to verify the phase purity of all the synthetic samples and in all cases a single phase CHAp was produced. Fourier Transform infrared (FT-IR) spectra were collected over a range of 650 to 4000 cm^{-1} for the samples on a Nicolet 670 FT-IR spectrometer in adsorption mode. Samples were ground in an agate mortar with spectroscopic grade KBr in an approximate 1:10 ratio of sample to KBr and spectra were collected for 128 scans at a resolution 1 cm^{-1}. Raman spectra were collected over a range of 200 to 3900 cm^{-1} on an InPhotonics RS-2000 Raman Spectrometer at a resolution of 1 cm^{-1}.

Most NMR spectra were collected on a 400 MHz Varian Inova spectrometer at operating frequencies of 399.76 MHz, 161.82 MHz, and 100.57 MHz for ^{1}H, ^{31}P and ^{13}C respectively. ^{1}H Single Pulse magic angle spinning (SP/MAS) NMR spectra were collected at a spinning rate of 15 kHz on a Chemagnetics probe configured for 4 mm (o.d.) rotors and modified to yield a very low ^{1}H background signal which is insignificant compared to signal from the samples and was not subtracted from the spectra. ^{31}P{^{1}H} 2-dimensional (2-d) Heteronuclear Correlation (HetCor) and ^{13}C{^{1}H} 2-d HetCor spectra were acquired with a Varian/Chemagnetics 3.2 mm T3 probe assembly at a 10 kHz spinning rate. For the ^{13}C{^{1}H} HetCor we acquired a total of 64 hypercomplex points in *t*1 with a 100 μs increment, corresponding to a 10 kHz F1 spectral window, at contact times from 0.5 to 10.0 ms using a linear ramp of the ^{1}H field to optimize signal intensity. For the ^{31}P{^{1}H} HetCor spectra a total of 128 hypercomplex points in *t*1 were collected with a 20 μs increment, corresponding to a 50 kHz F1 spectral window. All HetCor NMR data were processed with standard linear prediction methods to complete the signal in *t*1. ^{1}H spectra were referenced to tetramethylsilane (TMS) by setting the hydroxyl resonance in a standard reagent grade hydroxylapatite to $\delta_{H\text{-}1}$ = 0.2 ppm.[15] ^{31}P spectra were referenced with respect to 85% H_3PO_4 using the same hydroxylapatite as an external reference at $\delta_{P\text{-}31}$ = 2.65 ppm (shift measured previously with respect to an 85% H_3PO_4 solution). ^{13}C spectra were referenced with respect to TMS using adamantane as an external reference at $\delta_{C\text{-}13}$ = 38.6 ppm.[16] The ^{1}H dimension in the ^{13}C{^{1}H} HetCor were referenced with a ^{31}P{^{1}H} HetCor spectrum of hydroxylapatite using the same F1 acquisition parameters.

^{23}Na SP/MAS NMR, ^{23}Na{^{31}P} REDOR, and ^{13}C{^{31}P} CP/REDOR spectra were collected on a 500 MHz Varian Infinity Plus Spectrometer at operating frequencies of 499.78 MHz, 202.32 MHz, 132.17 MHz and 125.69 MHz for ^{1}H, ^{31}P, ^{23}Na, and ^{13}C respectively. ^{23}Na SP MAS NMR spectra were collected using a 1 μs pulse at a spinning rate of 18 kHz. ^{23}Na{^{31}P} REDOR spectra were collected at a spinning rate of 10 kHz using selective spin-echo pulses for ^{23}Na (π = 15 μs) and 8 μs re-coupling pulses for ^{31}P. The ^{1}H→ ^{13}C{^{31}P} CP/REDOR spectra were collected at a spinning rate of 5 kHz, and using π-pulses of 12 μs on both the ^{13}C and ^{31}P channels and a 5 ms ^{13}C{^{1}H} CP preparation. ^{23}Na SP/MAS and multiple quantum (MQ) MAS NMR spectra were collected on the 400 MHz spectrometer at 105.74 MHz and a spinning rate of 15 kHz. For the ^{23}Na MQMAS spectra 2.9 μs excitation and 1.1 μs pulses were used (ν_1 = 125 kHz) followed by a selective 15 μs (ν_1 = 16 kHz) z-filtering pulse collecting a total of 128 hypercomplex points in *t1* with a 20 μs increment.[17, 18] ^{23}Na MQ MAS NMR data were processed using standard shearing methods.[18] In all cases ^{23}Na spectra were referenced with respect to an aqueous 1M NaCl solution.

4. Results

4.1. Sample Composition

The chemical compositions of the ^{13}C-enriched AK-4 and AK-5H samples are similar to those which have been measured previously for sodium bearing CHAp which has been shown to be reasonable analogues for human dental enamel.[9] These results give Na contents of 2.7 and 1.6 wt% and Ca:P molar ratios of 1.67 and 1.76 for AK-4 and AK-5H respectively. Carbonate contents of the CHAp samples were estimated by the method proposed by Krajewski et al.[14] based on a correlation of the intensity ratio between the Raman active υ_1 PO_4 peak at 962 cm^{-1} and the υ_1 CO_3 peak at 1072 cm^{-1} and elemental analyses for carbonate content. Using this correlation we obtained values of approximately 5 wt%, and 7 wt% carbonate for the AK-4 and AK-5H, samples respectively. These values for AK-4 and AK-5H place the carbonate content of these samples within this range of natural biogenic apatites, such as bone apatite and dental enamel, which contain 3.5 to 8 wt% carbonate.[1, 19] The molar ratios of Na:carbonate in these samples (1.4 and 0.6 for AK-4 and AK-5H respectively) suggest Na is important to the carbonate substitution mechanisms.

4.2. Vibrational Spectroscopy

The results for the vibrational spectroscopy for the samples AK-4, AK-5H, AK-2H and AK-2HD are summarized in Table 4.1.[20] The Raman spectra taken of the sample (Figure SI-1, Supporting Information) contain only a few peaks. Peaks are observed in all samples at 1086, 1050, 962, 608, 590, and 432 cm^{-1} which correspond to PO_4 modes.[5, 14] A single peak at, 1072 cm^{-1}, was identified for CO_3 which corresponds to the υ_1 mode.[14] Hydroxyl modes were observed for the AK-2HD sample, for which a shifted OD peak was observed at 2636 cm^{-1}.

The FT-IR spectra (Fig. 4.1) exhibit peaks characteristic of those previously described for carbonate groups present in the apatite structure.[5, 6, 8] In the spectra for AK-2H distinct peaks can be observed at 879 and 872 cm^{-1} for the CO_3 υ_2 modes for the A and B carbonate sites respectively (Fig. 4.1b). Additionally, peaks are observed between 1500 and 1300 cm^{-1} which agree well with those reported previously for the υ_3 modes of CO_3 in carbonated apatite. These same peaks are also apparent in the spectra of the AK-4 and AK-5H samples but are shifted to lower wavenumber with respect to those for AK-2H due to the ^{13}C enrichment. While a distinct doublet is not observed in the CO_3 υ_2 region of the AK-4 sample an asymmetric peak is observed with its two components corresponding to the positions of the doublet. We also observe in the AK-2H sample CO_3 combination bands at 2520 and 2476 for $\upsilon_1+\upsilon_3$ and at 2926 cm^{-1} for $2\upsilon_3$.[21] These same bands occur in the ^{13}C-enriched samples but are subsequently shifted towards lower wavenumbers.

In response to NMR data that indicate the presence of weakly hydrogen bonded bicarbonate groups (see below), we dueterated the AK-2H sample (AK-2HD) but saw no significant shifting in the CO_3 regions. However, small peaks at 2928 and 2850 cm^{-1} that occur in the region which are usually assigned to CO_3 $2\upsilon_3$ [21] can be observed to disappear with dueteration (Fig. 4.1C). However, these peaks are also not apparent in spectra of the ^{13}C-enriched samples AK-4 and AK-5H. This result may indicate the presence of protonated carbonate in these samples, however, the vibrational spectra are inconclusive in this respect.

4.3. ^{13}C NMR

The ^{13}C SP/MAS NMR spectrum of sample AK-5H shows a relatively broad, asymmetric peak (Fig. 4.2a) centered near $\delta_{C-13} = 170$ ppm. This spectrum appears similar to that observed previously for a B-type carbonated apatite where an asymmetric peak at 170.2 ppm was observed.[7] This same study also reported a peak at 166.5 ppm from A-type substitution in their AB-type CHAp which is not observed in the present samples. Variable CP/MAS contact time experiments show systematic changes in shape of the peak at 170 ppm that suggests the presence of at least two resonances. At long contact times (Fig. 4.2b) the peak exhibits a shape similar to that of the SP spectrum, but in spectra collected at short contact times a second peak is clearly evident (Fig. 4.2c). The variation in peak shape with contact time can be described by intensity changes of two components corresponding to a sharp peak at 170.8 ppm (1.3 ppm full width at half-maximum; FWHM) and a broader asymmetric resonance at 168.9 ppm (Fig. 4.2d). The shape of the broad peak does not vary significantly with contact time and was represented, for purposes of spectral integration, by a sum of two Gaussian curves at constant intensity ratio. We also observe similar peak shapes in $^{1}H\rightarrow{}^{13}C\{^{31}P\}$ CP/REDOR spectra taken of the AK-5H sample (Fig. 4.SI-2, Supporting Information). Nearly identical lineshapes were observed in the control (S_0), REDOR (S) and REDOR difference spectra (S_0-S) which indicates a similar close association of all the ^{13}C to ^{31}P. This result shows that all the ^{13}C species must be contained in the CHAp and that the distinct ^{13}C resonances cannot be distinguished easily based on proximity to P using this method. The ^{13}C chemical shift anisotropy (CSA) for spectra collected at contact times of 0.5 ms and 15 ms, obtained by fitting the integrated intensities of the spinning sidebands[22] were very similar with spans (Ω) of 91.0 and 89.9 ppm and skews (κ) of 0.42 and 0.51 respectively.

The CP dynamics of the intensity build up was analyzed by fitting variable contact time $^{13}C\{^{1}H\}$CP/MAS spectra to the same components (Fig. 4.2d) allowing only the intensities to vary. The experimental conditions unmodulated, continuous wave (CW) polarization transfer and a spinning rate of 3.0 kHz were chosen to correspond to previous study of carbonate groups[23] and allow us to directly relate the results obtained to those of previous studies on weakly coupled $^{13}C/^{1}H$ systems.[23, 24] These results indicate that two separate ^{1}H spin reservoirs contribute intensity to the each of the ^{13}C resonances represented by the peaks at 169.8 and 170.8 ppm. Each ^{13}C peak exhibits bi-exponential CP intensity buildup with a small apparent fraction (13 - 34%) of the intensity increasing quickly with contact time (T_{IS} values of 0.8 and 0.7 ms) and the remainder exhibits a slower rate defined by T_{IS} values of 4.7 and 6.5 ms for the peaks at 169.8 and 170.8 ppm respectively. These data did not allow $T_{1\rho,H}$ value to be determined because the intensities continued to increase for all contact times. We independently measured the ^{1}H $T_{1\rho}$ by introducing a delay before the contact pulse to allow the ^{1}H to evolve under the spin locking pulse. At constant contact time the $^{13}C\{^{1}H\}$ CP/MAS intensity decays according to a bi-exponential function. This result indicates the presence of at least two proton spin reservoirs associated with the ^{13}C with a subset of spins characterized by a short $T_{1\rho,H}$ of 1.8 ms (32%) while the majority relax more slowly with a value of $T_{1\rho,H} = 33$ ms.

4.4. HetCor NMR

$^{13}C\{^1H\}$ 2-dimensional HetCor NMR spectra were acquired for the AK-5H sample at a variety of contact times to examine the relationship between the H and carbonate groups in this system. A typical spectrum is shown in Figure 4.3 as a contour plot. The individual summed ^1H projections contain three individual peaks where a peak is centered about δ_{H-1} = 0.0 ppm and two additional peaks which occur at 1.3 ppm, and 5.5 ppm, the latter of which is broad and asymmetrical with a tail extending to 11 ppm. The peaks at 1.3 and 5.5 ppm are prominent in the ^1H summed projections collected at short contact time, whereas the peaks centered about 0.0 ppm grow in to become the dominant peak in the spectra at long contact times (Fig. 4.4a). The contour plot also shows clearly the presence of two ^{13}C resonances at δ_{C-13} = 170.8 and 169.8, that were inferred from the CP/MAS spectra at variable contact time. The summed ^{13}C projections (Fig. 4.4b) show similar changes in peak shape with increase of contact time as those collected for the variable contact time $^{13}C\{^1H\}$CP/MAS experiment (Fig. 4.2).

The HetCor spectra indicate that the resolved carbonate environments are distinguished by association with different ^1H environments and that the H environments are strongly related to carbonate substitution. At short contact times the carbonate resonance at δ_{C-13} = 169.8 ppm is most strongly correlated to peaks at δ_{H-1}= -0.1 and 5.5 ppm (Fig. 4.5a). The peak at δ_{C-13} = 170.8 ppm appears to shows a correlation with the δ_{H-1} = 5.5 ppm peak that appears weak due to the width of this peak whereas a more apparent stronger correlations for this site are observed with the proton resonances at δ_{H-1} = 0.07 and 1.3 ppm due to their narrow lineshape (Fig. 4.5b). The CP dynamics for each $^{13}C/^1H$ cross peak was determined by fitting the ^1H slices (F1) taken at the respective ^{13}C isotropic chemical shift to a sum of Gaussian curves (Table 4.2). The fitted relative intensities were scaled to total integrated intensities obtained from $^{13}C\{^1H\}$ CP/MAS variable contact time spectra acquired under the same conditions (Fig. 4.6). Corresponding T_{CH} and $T_{1\rho,H}$ values were determined by fitting the intensities to a classical biexponential CP buildup curve.[25] The $^1H(5.5)/^{13}C(169.8)$ cross-peak exhibits a quick intensity buildup characterized by a T_{CH} value of 0.8 ms and decay with an apparent $T_{1\rho,H}$ value of 12 ms. The peaks at 1.3 and -0.1 ppm exhibit slower intensity buildups with T_{CH} values of 2.7 and 4.3 ms respectively. This result indicates that the ^1H species represented by the peak at 5.5 ppm are more closely associated with this carbonate site than those at 1.3 and -0.1 ppm. The CP dynamics for the carbonate site at $\delta_{C\text{-}13}$ = 170.8 ppm are characterized by T_{CH} values of 0.8, 0.7 and 3.6 ms for the sites at $\delta_{H\text{-}1}$= 5.5, 1.3 and 0.07 ppm respectively. This result suggests strong coupling between this carbonate site to the peaks at 5.5 and 1.3 ppm and a weak correlation to that at 0.07 ppm. Although the ^{1}H peak at 5.5 ppm does not appear prominent in the spectra, its intensity is significant at short contact times due to its large width. However, comparison of the contour plot (Fig. 4.3) and fitted ^{13}C spectral components (Fig. 4.2d) suggests it is likely that much of the apparent ^{1}H(5.5)/^{13}C(170.6) cross-peak intensity corresponds to overlap with the ^{13}C peak at 168.9 ppm.

Additional $^{13}C\{^1H\}$ HetCor spectra were collected at a contact time of 10 ms with a mixing time introduced between ^{1}H excitation and the $^1H\rightarrow{}^{13}C$ polarization transfer. This experiment indicated whether the short apparent ^{1}H $T_{1\rho}$ values observed for the various ^{1}H sites by HetCor contain a contribution from ^{1}H-^{1}H spin diffusion to an abundant ^{1}H reservoir at long contact times. We observe that as the mixing time increases from 20 to 40 ms the peaks at 1.3 and those centered about 0.0 ppm remain at a constant intensity while that at 5.5 ppm gradually decays at a rate consistent with the apparent value of $T_{1\rho,H}$ = 12 ms measured for this peak. This result indicates that the short apparent $T_{1\rho,H}$ for the peak at 5.5 ppm appears results from spin diffusion to a bulk ^{1}H reservoir. However, the peak at 1.3 ppm appears to represent a distinct ^{1}H reservoir that relaxes to thermal equilibrium before spin diffusion to the other peaks, giving a distinct $T_{1\rho,H}$. These results are consistent with the observations from the $T_{1\rho,H}$ measurements obtained from the $^{13}C\{^1H\}$CP/MAS spectra where a bi-exponential decay was observed although absolute values from HetCor are larger probably due to faster spinning rate.

$^{31}P\{^1H\}$ HetCor NMR spectra were also taken of the AK-5H sample to examine whether the proton environments observed in the $^{13}C\{^1H\}$ HetCor NMR spectra are also occur near phosphate in the apatite (Fig. 4.SI-2, Supporting Information). The ^{31}P projections show only a single peak at $\delta_{P\text{-}31}$ = 2.8 ppm. The ^{1}H projection shows peaks at $\delta_{H\text{-}1}$ = 0.2 ppm, 1.3 ppm, and 5.5 ppm, similar to those observed in the $^{13}C\{^1H\}$ HetCor NMR spectra. In this case, however, the peaks at 1.3 and 5.5 ppm are much weaker and that at 1.3 ppm appears not as a distinct peak but rather as a weak shoulder on the dominant 0.2 ppm peak. The ^{1}H peak at 5.5 ppm is somewhat sharper than the $^{13}C\{^1H\}$ HetCor, suggesting that the 5.5 ppm cross peak might contain a contribution from HPO_4 groups,[26] but the data are inconclusive. These results indicate an association between the ^1H peaks at 1.3 and 5.5 ppm and the phosphate groups, and show that these H occur in the apatite structure.

4.5. ^1H MAS NMR

^1H SP/MAS NMR spectra show a complex set of peaks for the ^{13}C enriched CHAp samples (Fig. 4.7). These spectra are dominated by three peaks at chemical shifts of δ_{H-1} = 0.2, 1.3, and 5.2 ppm. An additional set of sharp peaks occur in the spectrum for AK-4 near 2.3 ppm which contribute less than 2% of the total intensity and do not occur in HetCor spectra taken of this sample (not shown) and are, therefore, due to unknown impurities or surface sites. Also a broad component centered at about 11.6 ppm occurs in this spectrum which is similar to that observed for HPO_4 groups in nanocrystalline hydroxylapatite[26] but their identity in this sample is uncertain.

Comparison of the spectra for AK-4 and AK-5H show that the hydrothermal treatment has an effect on the proton environments present in the samples. The collection methods also differed between these two samples and could explain the differences ^1H spectra but what would be expected to change would be the amount of adsorbed water observed. However, the spectrum of the AK-5H exhibits decreased linewidths in comparison to that for AK-4 with the major peak at 5.2 ppm decreasing from FWHM of 1.8 ppm to a FWHM of 1.1 ppm. The set of peaks near 2.3 ppm and the broad peak at 11.6 ppm are not present in the spectrum of the AK-5H sample. There is, however, an additional sharp peak at 4.8 ppm (0.1 ppm FWHM) which given its position and narrow linewidth is likely the result of fluid phase water either as inclusions or adsorbed on the surface. Although the chemical shift region of 2 to -1 ppm in the spectrum of AK-5H contains several overlapping peaks, the HetCor data (described above) contain only the resonances at 1.3 ppm and those located about 0 ppm. It is likely these additional peaks are either not resolved in the ^1H slices of the HetCor spectra, possibly due to rapid motion, or are the result of impurity phases. Comparison of the ^1H spectra obtained from the ^{13}C and ^{31}P HetCor data with these direct-observe spectra shows that the CHAp contains many H environments that are not directly associated with the apatite structure or are mobile on the NMR timescale. These H are likely to be bonded to oxygen and are likely to contribute to the OH-stretch region of the vibrational spectra.

4.6. ^{23}Na NMR

Since replacement of Ca^{2+} in the structure by Na^+ has been proposed as a method for charge balancing carbonate substitutions in CHAp[5, 9] and chemical analysis showed significant Na content, we studied the AK-5H sample with ^{23}Na NMR techniques. The ^{23}Na SP/MAS spectra are similar at both 9.4 and 11.7 T field strengths and show a broad, asymmetric peak (Fig. 4.8a). ^{23}Na{^{31}P} REDOR spectra were taken over a variety of dephasing periods to investigate the connectivity between Na and P in the sample. Although this technique can be used as a method for determining P - Na distances[27] in this instance we used it only as a spectral editing technique. We observed similar peak shapes for the ^{23}Na control spectrum (S_0; Fig. 4.8b), the ^{23}Na{^{31}P} REDOR spectrum (S; Fig. 4.8c) and the REDOR difference spectrum (S_0-S; Fig. 4.8d). The REDOR fraction ($1-S/S_0$) under these conditions reaches unity at 4 ms dephasing time indicating that all of the Na in the sample is associated with P and therefore contained in the CHAp and not a separate phase. Comparison of the ^{23}Na SP (Fig. 4.8a) and ^{23}Na spin echo spectra (S_0, Fig. 4.8b) shows the presence of a narrow component in the former that does not appear in the spin echo data, probably due to a short T_2. However, ^{23}Na MQ/MAS spectra (Fig. 4.SI-4, Supporting Information) do not resolve distinct ^{23}Na resonances and instead show 2-dimensional peak shapes consistent with distributions in both chemical shift and quadrupolar coupling. This result indicates that the Na is disordered in the CHAp with a distribution of orientations and bond distances. The SP data at both 11.7 T and 9.4 T can be fit with a sum of quadrupolar MAS lineshapes corresponding to a distribution of electric field gradients[28] that approximates a Gaussian distribution of quadrupolar coupling constants with an average of 1.2 MHz and a width of 2.6 MHz (FWHM); truncated near $C_Q = 0$, at an average isotropic chemical shift of $\delta_{Na\text{-}23} = -3.9$ ppm.

5. Discussion

5.1. ^{1}H Peak Assignments of carbonate-associated H

Our results from the ^{1}H SP/MAS and the HetCor spectra indicate that the carbonate groups are associated with several distinct H species. While the position of the peak at 0.2 ppm observed in the ^{1}H SP/MAS and the ^{31}P{^{1}H} HetCor is in good agreement with those previously observed by ^{1}H SP/MAS for hydroxyl groups in hydroxylapatite,[15] close examination of the HetCor data show that the hydroxyl resonance is slightly shifted to 0.07 and -0.1 ppm in slices taken at $\delta_{C-13} = 170.8$ and 169.8 ppm respectively. The intensity of these peaks increases slowly with contact time in all the ^{13}C{^{1}H} HetCor slices indicating that this proton environment is well removed from the carbonate carbon. The long T_{CH} values (3 to 4 ms) are consistent with long H-C distances and are comparable to the T_{PH} values observed for pure HAp.[26] Considering that for HAp a ^{1}H chemical shift 0.2 ppm to correspond to a d(O···O) = 3.44 Å[29] these peaks at 0.07 and -0.1 ppm suggest somewhat longer O···O distances near the carbonate substitution.[30] We therefore assign these peaks to hydroxyl groups at positions that are perturbed and slightly from the normal hydroxyl position by the insertion of carbonate.

The cross-peak at $\delta_{H-1} = 1.3$ ppm exhibits a very rapid intensity buildup in the HetCor slices taken at $\delta_{C-13} = 170.8$ ppm corresponding to a T_{CH} value (0.7 ms) that is similar to that observed for the initial $^1\text{H}\rightarrow{}^{13}\text{C}$ polarization transfer for bicarbonate defects in calcite.[23] Such short T_{CH} requires C-H distances (ca. 2 Å) that are too short to be accounted for by hydroxyl groups hydrogen bonded to carbonate, especially considering that this ^{1}H chemical shift indicates a weak H-bonding environment [d(O···O) ≈ 3.0 Å].[30] For comparison chemical shifts reported for strongly hydrogen bonded bicarbonate are much higher for phases such as nahcolite ($NaHCO_3$; $\delta_{H-1} = 14.1$ ppm) and trona [$Na_3H(CO_3)_2(H_2O)_2$; $\delta_{H-1} = 18.6$ ppm], which have a d(O···O) of 2.55 and 2.37 Å respectively.[23] Therefore, we interpret the combination of short T_{CH} values (0.7 ms) and small ^{1}H chemical shift to indicate H directly bonded to carbonate ion that is a weak hydrogen bond donor, and not an OH group in close association with a carbonate group. These results indicate significant contribution of bicarbonate to the peak at 170.8 ppm such that it accounts for about 24% of the polarization transfer from CP kinetics (Table 4.2).

Previous studies have noted distinct differences of ^{13}C chemical shift and chemical shift anisotropy (CSA) between alkali bicarbonates and their carbonate containing counterparts[31] (e.g, $KHCO_3$: $\delta_{C\text{-}13,\,iso}$ = 159.9 ppm, Ω = 97 ppm κ = -0.46; K_2CO_3: $\delta_{C\text{-}13,\,iso}$ = 169.3, Ω = 82 ppm κ = 0.61). In these compounds bicarbonate groups accept and donate strong hydrogen bonds. In contrast, bicarbonate defects in calcite, which are moderate hydrogen bond donor, exhibit ^{13}C chemical shift and CSA that are nearly indistinguishable from that of the deprotonated carbonate groups (HCO_3: $\delta_{C\text{-}13,\,iso}$ = 168.7 ppm, Ω = 84 ppm, κ = 0.55: CO_3: $\delta_{C\text{-}13,\,iso}$ = 168.7 ppm, Ω = 76 ppm, κ = 0.95).[23] The CSA patterns in $^{13}C\{^1H\}$ CP/MAS NMR at short contact time (Ω = 91.0 ppm, κ = 0.43) match well those observed for bicarbonate in calcite.[23] Therefore, it appears that ^{13}C chemical shift parameters are insufficient to identify the difference between carbonate and bicarbonate in weakly hydrogen bonded systems.

The peak at 1.3 ppm also appears to contribute about 22% of the intensity to the ^{13}C cross-peak at 169.8 ppm (Table 4.2). However, this peak is not well resolved in the ^{1}H slices taken at 169.8 ppm and its intensity was obtained from fits in which the peak width and position were fixed to those derived for the $^1H(1.3)/^{13}C(170.8)$ cross-peak. It is possible, therefore, that the intensity of this peak in the ^{1}H slices at 169.8 ppm is just the tail of the peak at 0.07 ppm however, the much different $T_{1\rho,H}$ values indicates distinct H species. While the $^1H(1.3)/^{13}C(169.8)$ cross-peak exhibits a longer T_{CH} value than that of the $^1H(1.3)/^{13}C(170.8)$ cross-peak (2.7 and 0.7 ms respectively) the $T_{1\rho,H}$ values (18 ms) are the same within uncertainty suggesting that these cross-peaks correspond to the same H environment which is near both types of carbonate, but further removed from the carbonate at $\delta_{C\text{-}13}$ = 169.8 ppm and closer to that at 170.8 ppm. However, another possibility consistent with these observations is a channel hydroxyl with a weak hydrogen bond to the A-type channel carbonate. ^{1}H NMR peaks near this chemical shift have been reported for fluorhydroxylapatites[15] and it might be expected that the carbonate could be positioned closer to one of the adjacent OH groups in the channel to give a weak donor-acceptor geometry.

The peak at $\delta_{H\text{-}1}$ = 5.5 ppm exhibits a quick buildup of CP intensity in both the HetCor slices taken at $\delta_{C\text{-}13}$ = 170.8 and 169.8 ppm. However, the resolution in the ^{13}C dimension is poor and the contour plots suggest that these H environments are associated primarily with the peak at 169.8 ppm. This assignment is consistent with the considerable overlap of the peaks at 170.8 and 169.8 ppm (Fig. 4.2d), the larger width of the latter and the very similar CP kinetics fit to the 170.8 and 169.8 ppm slices. The ^{1}H(5.5)/^{13}C(169.8) cross-peak also exhibits a short T_{CH}, similar to that observed for bicarbonate defects in calcite,[23] indicative of a short C-H distance. Although the ^{1}H chemical shift of this cross-peak corresponds well to that observed for water contained in apatite[26] assignment of the short observed T_{CH} value to carbonate-water interaction would require a very short hydrogen bond distance and consequently a much more positive ^{1}H chemical shift value. We also observe that this peak decays when a mixing time is introduced in the HetCor experiment indicating that spin diffusion to the main ^{1}H reservoir near 0 ppm accounts for some of the apparent intensity loss at long contact times. We therefore assign the ^{1}H(5.5)/^{13}C(169.8) cross-peak to A-type bicarbonate groups in the channel sites that donate moderate hydrogen bonds, possibly to adjacent hydroxyl in the channels. The broad asymmetric lineshape in the ^{1}H-dimension with intensity tailing out to about 11 ppm corresponds to a wide range of hydrogen bond lengths with d(O···O) values ranging from about 2.88 to 2.66 Å.[30] Therefore, in the FT-IR spectra the corresponding OH stretch can be expected to give a broad, ill defined peak spanning 2982 to 3399 cm^{-1} [32] which would be difficult to observe.

5.2. A Type Substitution

Our NMR evidence for the presence of bicarbonate groups in CHAp implies defect structures in addition to those suggested previously. In the case of A-type (channel) carbonate the method for substitution that has been commonly reported is the removal of two hydroxyl groups for the inclusion of a single carbonate group.[8, 11]

$$[{}^{A}CO_3^{2-} = 2OH^{-}]$$

Peroos et al.[33] studied this substitution method in CHAp using molecular dynamics simulations and found that the most stable configuration of this A-type carbonate defect occurred with the carbonate ion located midway between the two hydroxyl positions. The calculated minimum energy configuration for this defect leads to a long hydrogen bond interaction between the carbonate oxygens and the channel hydroxyl with a d(O···O) distance of 2.75 Å. This distance corresponds well to the d(O···O) distance range of 2.66 to 2.88 Å derived for the bicarbonate carbonate group represented by the broad peak at δ_{H-1} = 5.5 ppm but its strong coupling to C indicates bonding to the carbonate group. The inclusion of bicarbonate, however, invokes a charge imbalance that must be accommodated. This charge imbalance could be compensated through the coupling of the A-type substitution with a corresponding Na^+ defect:

$[Na^+ + {}^AHCO_3^- = Ca^{2+} + 2OH^-]$.

The large molar Na/carbonate ratio found for our samples supports such a coupled substitution. One possible advantage of bicarbonate groups is that this configuration would allow the hydroxyl ordering within the channels to be preserved without significant perturbations of the hydroxyl ions in the channel sites. Weak interaction of a non-protonated carbonate oxygen with a hydroxyl could explain the cross peak at δ_{H-1} = 1.3 ppm in CHAp which corresponds well to that observed for a hydroxyl group in fluor-hydroxylapatites[15]. However, this chemical shift would correspond to an O···O distance longer than the 2.75 Å from the computation models.

5.3. AB Type Substitution

Previous studies have suggested that a coupled substitution is not only possible but in cases required for the incorporation of carbonate into both the A and B site in type AB CHAp.[9, 33] Computational models[33] suggest that a substitution for the AB-type defect can be accommodated by the removal of a channel hydroxyl and the movement of a channel hydroxyl to a position next to the B-type carbonate group.

$$[2CO_3^{2-} = PO_4^{3-} + {}^AOH^-]$$

It was found that this configuration gives the most energetically favorable defect of all A, B and AB-type substitution methods studied. However, this arrangement requires not only a close proximity of the B-hydroxyl to the carbonate group [d(O···O) = 2.24 to 2.77 Å], but also a crowding of the A-type carbonate due to the substitution for one channel hydroxyl instead of two. We find no evidence for a hydroxyl with such short hydrogen bond lengths; all H with large chemical shift appears to correspond to bicarbonate groups. Astala and Stott[34] suggest that the B-type carbonate is best accommodated through a Ca vacancy and a corresponding HPO_4 substitution. While we do see potential evidence for HPO_4 groups the model proposed for this substitution would require short hydrogen bond distances to the carbonate oxygen and again a correspondingly large positive ^1H

chemical shift. Fleet and Liu[9] suggest that a coupled AB-type substitution could be accomplished through an additional substitution of a Na^+ for Ca^{2+}. However, they do not propose a specific charge balance mechanism. Based on this information we can propose an additional substitution which incorporates bicarbonate into the B-site through a coupling with an A-site substitution and Na:

$$[Na^+ + {}^{B}HCO_3^- + {}^{A}CO_3^{2-} = Ca^{2+} + PO_4^{3-} + OH^-]$$

This substitution method would eliminate the need for an additional hydroxyl group to be incorporated with the B-type substitution. The replacement of two hydroxyl groups in the channels for one carbonate group would allow for less steric hindrance of the A-type substitution but would require a second Na^+ for charge-balance. If the bicarbonate ion is oriented with respect to the channel similar to that proposed by Fleet and Liu[9] with its plane lying more or less parallel to one of the far faces of the phosphate ion the smallest d(O···O) distance for the bicarbonate ion to the closest oxygen of the non-protonated carbonate group would be about 3.05 Å. This geometry is in good agreement with the d(O···O) value 3.04 Å estimated from the chemical shift of the ^1H cross-peak at 1.3 ppm. Observation of similar $T_{1\rho,H}$ values (18ms) for both the $^1H(1.3)/^{13}C(170.8)$ and the $^1H(1.3)/^{13}C(169.8)$ cross-peaks is consistent with a contribution from a single H environment associated with both carbonate environments as expected for such a coupled substitution. In this case, the short T_{CH} of the $^1H(1.3)/^{13}C(170.8)$ cross-peak indicates protonation of the B-type carbonate.

6. Acknowledgements

This work was supported by the Center for Environmental Molecular Science which is funded by the NSF EMSI program (CHE-0221934) and NSF CHE-03-21001 for instrumentation.

7. References

[1] J. Barralet, S. Best, W. Bonfield, Carbonate substitution in precipitated hydroxyapatite: An investigation into the effects of reaction temperature and bicarbonate ion concentration, Journal of Biomedical Materials Research 41(1998) 79-86.

[2] J.C. Elliott, Calcium Phosphate Biominerals, Phosphates: Geochemical, Geobiological, and Materials Importance 48(2002) 427-453.

[3] J.L. Conca, J. Wright, An Apatite II permeable reactive barrier to remediate groundwater containing Zn, Pb and Cd, Applied Geochemistry 21(2006) 1288-1300.

[4] J. Wright, K.R. Rice, B. Murphy, J. Conca, PIMS Using Apatite II^{TM}: How It Works To Remediate Soil and Water, in: R.E. Hinchee, B. Alleman, (Eds), Sustainable Range Management, Battelle Press, Columbus, OH, 2004.

[5] D.G.A. Nelson, J.D.B. Featherstone, Preparation, Analysis, and Characterization of Carbonated Apatites, Calcified Tissue International 34(1982) S69-S81.

[6] M.E. Fleet, X.Y. Liu, Carbonate apatite type A synthesized at high pressure: new space group (P(3)over-bar) and orientation of channel carbonate ion, Journal of Solid State Chemistry 174(2003) 412-417.

[7] K. Beshah, C. Rey, M.J. Glimcher, M. Schimizu, R.G. Griffin, Solid-State ^{13}C and Proton NMR-Studies of Carbonate-Containing Calcium Phosphates and Enamel, Journal of Solid State Chemistry 84(1990) 71-81.

[8] M.E. Fleet, X.Y. Liu, Location of type B carbonate ion in type A-B carbonate apatite synthesized at high pressure, Journal of Solid State Chemistry 177(2004) 3174-3182.

[9] M.E. Fleet, X. Liu, Coupled substitution of type A and B carbonate in sodium-bearing apatite, Biomaterials 28(2007) 916-926.

[10] R.M. Wilson, J.C. Elliott, S.E.P. Dowker, R.I. Smith, Rietveld structure refinement of precipitated carbonate apatite using neutron diffraction data, Biomaterials 25(2004) 2205-2213.

[11] M.E. Fleet, X.Y. Liu, P.L. King, Accommodation of the carbonate ion in apatite: An FTIR and X-ray structure study of crystals synthesized at 2-4 GPa, American Mineralogist 89(2004) 1422-1432.

[12] R.M. Wilson, S.E.P. Dowker, J.C. Elliott, Rietveld refinements and spectroscopic structural studies of a Na-free carbonate apatite made by hydrolysis of monetite, Biomaterials 27(2006) 4682-4692.

[13] Y. Suetsugu, I. Shimoya, J. Tanaka, Configuration of carbonate ions in apatite structure determined by polarized infrared spectroscopy, Journal of the American Ceramic Society 81(1998) 746-748.

[14] A. Krajewski, M. Mazzocchi, P.L. Buldini, A. Ravaglioli, A. Tinti, P. Taddei, C. Fagnano, Synthesis of carbonated hydroxyapatites: efficiency of the substitution and critical evaluation of analytical methods, Journal of Molecular Structure 744(2005) 221-228.

[15] J.P. Yesinowski, H. Eckert, Hydrogen Environments in Calcium Phosphates - ^{1}H MAS NMR at High Spinning Speeds, Journal of the American Chemical Society 109(1987) 6274-6282.

[16] W.L. Earl, D.L. Vanderhart, Measurement of C-13 Chemical-Shifts in Solids, Journal of Magnetic Resonance 48(1982) 35-54.

[17] L. Frydman, J.S. Harwood, Isotropic Spectra of Half-Integer Quadrupolar Spins from Bidimensional Magic-Angle-Spinning Nmr, Journal of the American Chemical Society 117(1995) 5367-5368.

[18] J.P. Amoureux, C. Fernandez, Triple, quintuple and higher order multiple quantum MAS NMR of quadrupolar nuclei, Solid State Nuclear Magnetic Resonance 10(1998) 211-223.

[19] B. Wopenka, J.D. Pasteris, A mineralogical perspective on the apatite in bone, Materials Science & Engineering C-Biomimetic and Supramolecular Systems 25(2005) 131-143.

[20] S.J. Joris, C.H. Amberg, Nature of Deficiency in Nonstoichiometric Hydroxyapatites .2. Spectroscopic Studies of Calcium and Strontium Hydroxyapatites, Journal of Physical Chemistry 75(1971) 3172-&.

[21] M.J. Genge, A.P. Jones, G.D. Price, An Infrared and Raman-Study of Carbonate Glasses - Implications for the Structure of Carbonatite Magmas, Geochimica Et Cosmochimica Acta 59(1995) 927-937.

[22] J. Herzfeld, A.E. Berger, Sideband Intensities in Nmr-Spectra of Samples Spinning at the Magic Angle, Journal of Chemical Physics 73(1980) 6021-6030.

[23] J. Feng, Y. Lee, R.J. Reeder, B.L. Phillips, Observation of bicarbonate in calcite by NMR spectroscopy, American Mineralogist 91(2006) 957-960.

[24] J. Feng, Y. Lee, J.D. Kubicki, R.J. Reeder, B.L. Phillips, NMR Spectroscopy of Citrate in Solids: Cross-Polarization Kinetics in Weakly Coupled Systems, Magnetic Resonance in Chemistry Submitted(2007).

[25] W. Kolodziejski, J. Klinowski, Kinetics of cross-polarization in solid-state NMR: A guide for chemists, Chemical Reviews 102(2002) 613-628.

[26] C. Jager, T. Welzel, W. Meyer-Zaika, M. Epple, A solid-state NMR investigation of the structure of nanocrystalline hydroxyapatite, Magnetic Resonance in Chemistry 44(2006) 573-580.

[27] W. Strojek, H. Eckert, Medium-range order in sodium phosphate glasses: A quantitative rotational echo double resonance solid state NMR study, Physical Chemistry Chemical Physics 8(2006) 2276-2285.

[28] D. Coster, A.L. Blumenfeld, J.J. Fripiat, Lewis-Acid Sites and Surface Aluminum in Aluminas and Zeolites - a High-Resolution Nmr-Study, Journal of Physical Chemistry 98(1994) 6201-6211.

[29] A.T. Sanger, W.F. Kuhs, Structural Disorder in Hydroxyapatite, Zeitschrift Fur Kristallographie 199(1992) 123-148.

[30] J.P. Yesinowski, H. Eckert, G.R. Rossman, Characterization of Hydrous Species in Minerals by High-Speed ^{1}H MAS NMR, Journal of the American Chemical Society 110(1988) 1367-1375.

[31] D. Stueber, A.M. Orendt, J.C. Facelli, R.W. Parry, D.M. Grant, Carbonates, thiocarbonates, and the corresponding monoalkyl derivatives: III. The C-13 chemical shift tensors in potassium carbonate, bicarbonate and related monomethyl derivatives, Solid State Nuclear Magnetic Resonance 22(2002) 29-49.

[32] E. Libowitzky, Correlation of O-H stretching frequencies and O-H•••O hydrogen bond lengths in minerals, Monatshefte Fur Chemie 130(1999) 1047-1059.

[33] S. Peroos, Z.M. Du, N.H. de Leeuw, A computer modelling study of the uptake, structure and distribution of carbonate defects in hydroxy-apatite, Biomaterials 27(2006) 2150-2161.

[34] R. Astala, M.J. Stott, First principles investigation of mineral component of bone: CO_3 substitutions in hydroxyapatite, Chemistry of Materials 17(2005) 4125-4133.

8. Tables

Table 4.1. Comparison of major IR and Raman peak positions in cm^{-1}. Raman spectra were not collected for the AK-2H sample.

Assignment	AK-2H	AK-2HD		AK-4		AK-5H		Ref.
	IR	IR	Raman	IR	Raman	IR	Raman	
OH Stretch	3571	3571		3572		3571		[1]
H_2O Stretch	3376	3376		3329		3376		[2]
$^{12}CO_3\ 2\nu_3{}^2$	2926	2926						[2]
Uncertain	2928							
$^{13}CO_3\ 2\nu_3$						2838		
OD Stretch								
Uncertain	2850							
$^{12}CO_3\ \nu_1+\nu_3$	2520	2634	2636					[2]
$^{13}CO_3\ \nu_1+\nu_3$	2476			2464		2471		
						2434		
D_2O Stretch		2495						
$PO_4\ \nu_1+\nu_3$	2133	2138		2137		2135		[3]
	2075	2075		2075		2075		[3]
	1996	1998		1993		1997		[3]
$^{12}CO_3\ \nu_3$	1466	1468						[1]
	1418	1418						
$^{13}CO_3\ \nu_3$				1419		1414		
				1379		1376		
Uncertain		1200						
$PO_4\ \nu_3$	1090	1091		1093	1086	1092	1072	[1,4]
$CO_3\ \nu_1$			1086		1072		1050	[4]
$PO_4\ \nu_3$	1041	1043	1072	1040	1050	1044	962	[1,4]
$PO_4\ \nu_1$	962	962	1050	961	962	962		[1,4]
$^{12}CO_3\ \nu_2$	879	879	962	874		874		[1]
	872	872						
$^{13}CO_3\ \nu_2$				848		852		
						846		
$PO_4\ \nu_4$			608		608		608	[4]
			590		590		590	[4]
$PO_4\ \nu_2$			432		432		432	[4]

[1] Nelson and Featherstone (1982) [2] Genge et al (1995) [3] Joris and Amberg (1971) [4] Krajewski (2005)

Table 4.2. CP kinetic values obtained for the ^{1}H HetCor cross peaks. $T_{1\rho,H}$ values reported are apparent values. *value fixed to obtain suitable fit.

$\delta_{C\text{-}13}$	$\delta_{H\text{-}1}$	I_0 (%)	T_{CH} (ms)	$T_{1\rho,H}$ (ms)
169.8	-0.1	0.42(1)	4.3(1)	>100*
	1.3	0.22(3)	2.7(3)	18(2)
	5.5	0.31(2)	0.8(2)	17(1)
170.8	0.07	0.53(1)	4.3(1)	>100*
	1.3	0.24(1)	0.7(1)	18(1)
	5.5	0.23(3)	0.8(3)	12(2)

9. Figures and Captions

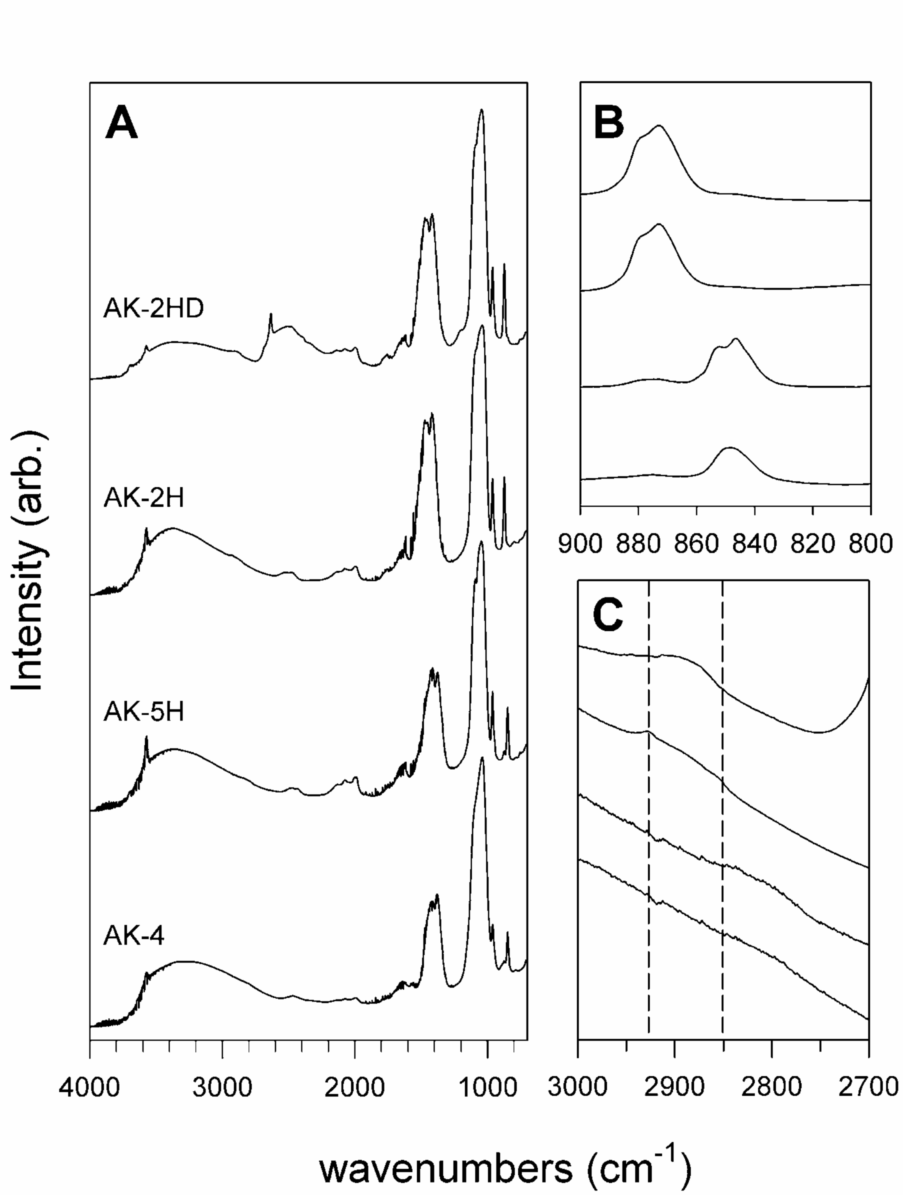

Figure 4.1. IR spectra of CAp samples from top to bottom: AK-2HD, AK-2H, AK-5H, and AK-4. **A**. Full IR spectra from 4000 to 650 cm^{-1}. **B**. Expanded view of CO_3 υ_2 region from 900 to 800 cm^{-1}. **C** Expanded view of the CO_3 $2\upsilon_3$ region from 2700 to 3000 cm^{-1}. Dashed lines correspond to the positions of the peaks at 2928 and 2850 cm^{-1} present in the spectrum taken of the sample AK-2H sample.

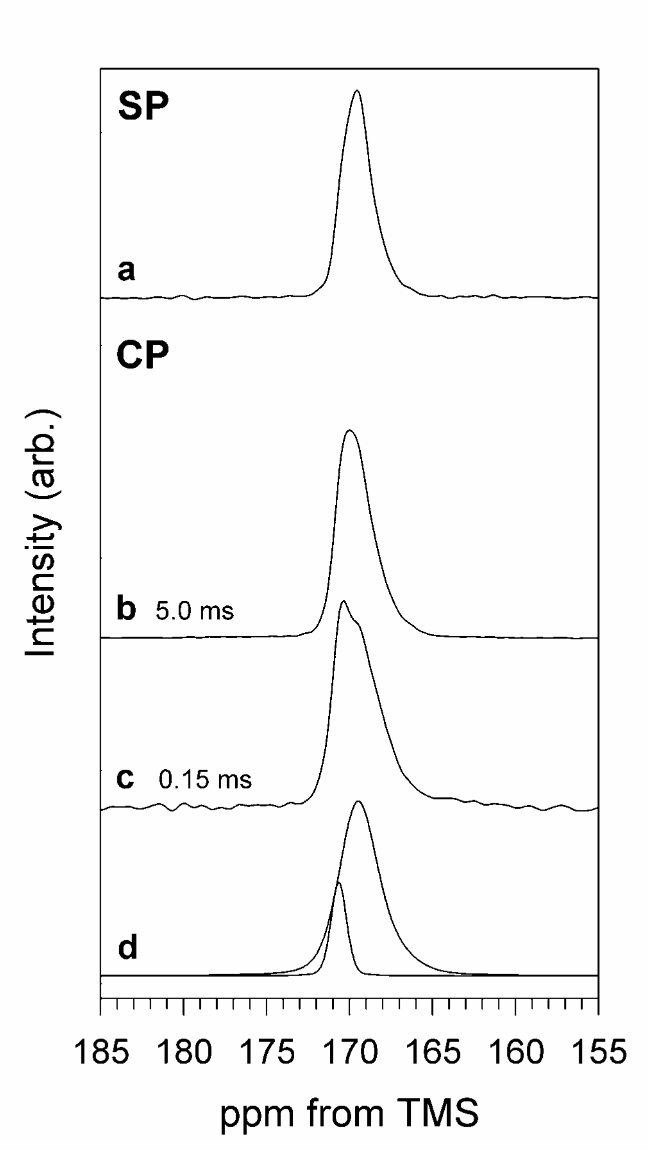

Figure 4.2. ^{13}C NMR spectra of CHAp sample AK-5H. **a)** ^{13}C SP/MAS; 120 s relaxation delay, 32 acquisitions. **b)** ^{13}C{^{1}H} CP/MAS; 5 ms contact time, 2 s relaxation delay, 4160 acquisitions. **c)** ^{13}C{^{1}H} CP/MAS; 0.15 ms contact time, 2 s relaxation delay, 4160 acquisitions. **d)** Spectral fit to **c)** corresponding to peaks at 170.8 and an asymmetric peak at 169.8 ppm. All spectra were collected at a spinning rate of 3.0 kHz.

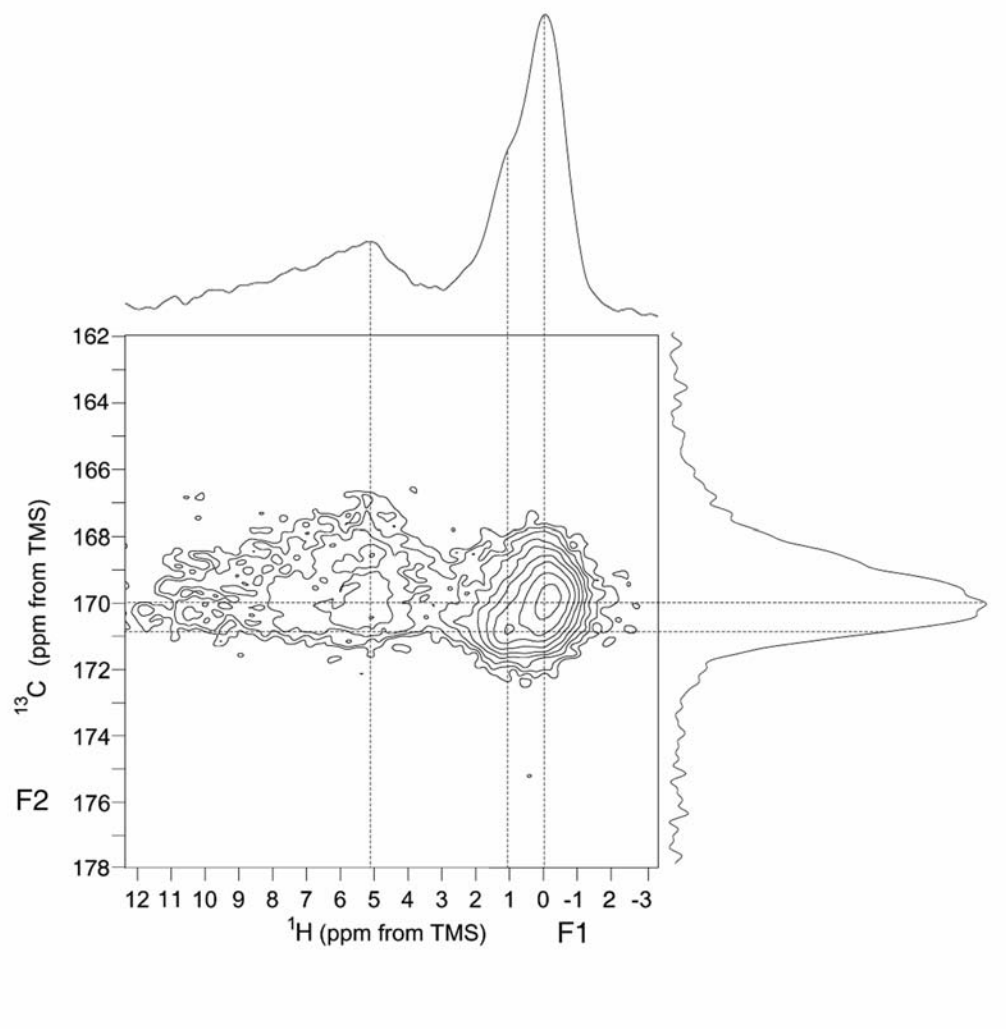

Figure 4.3. 2-dimensional ^{13}C{^{1}H} HetCor spectrum of AK-5H collected at a contact time of 3 ms and a spinning rate of 10 kHz. Spectra at top and side are summed projections over the centerband intensity

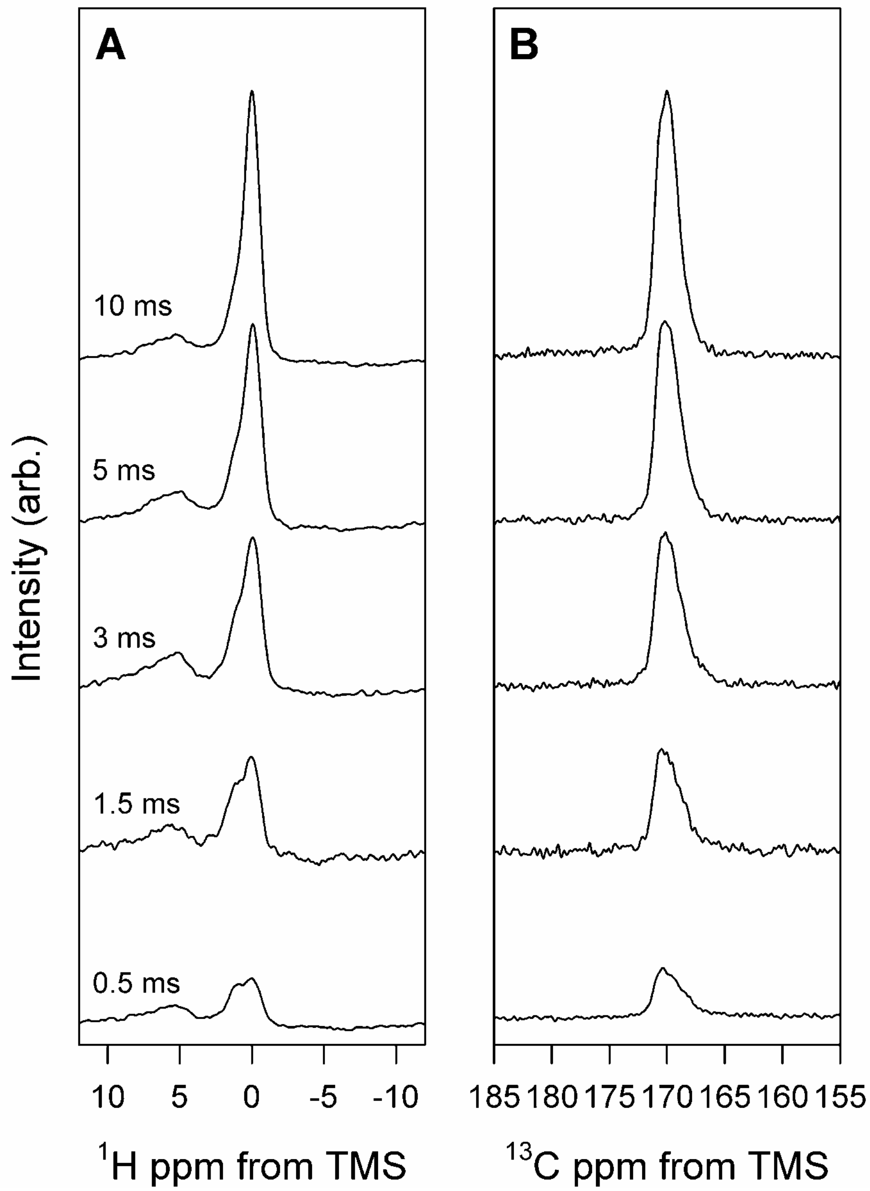

Figure 4.4. ^{13}C{^{1}H} HetCor NMR spectra of sample AK-5H. **A)** Indirectly detected ^{1}H spectra summed over the ^{13}C centerband. **B)** ^{13}C spectra summed over the ^{1}H dimension collected at a variety of contact times. A total of 128 hypercomplex increments in t1 were collected at a spinning rate of 10 kHz and a pulse delay of 1 s. Spectra are scaled to reflect absolute intensities.

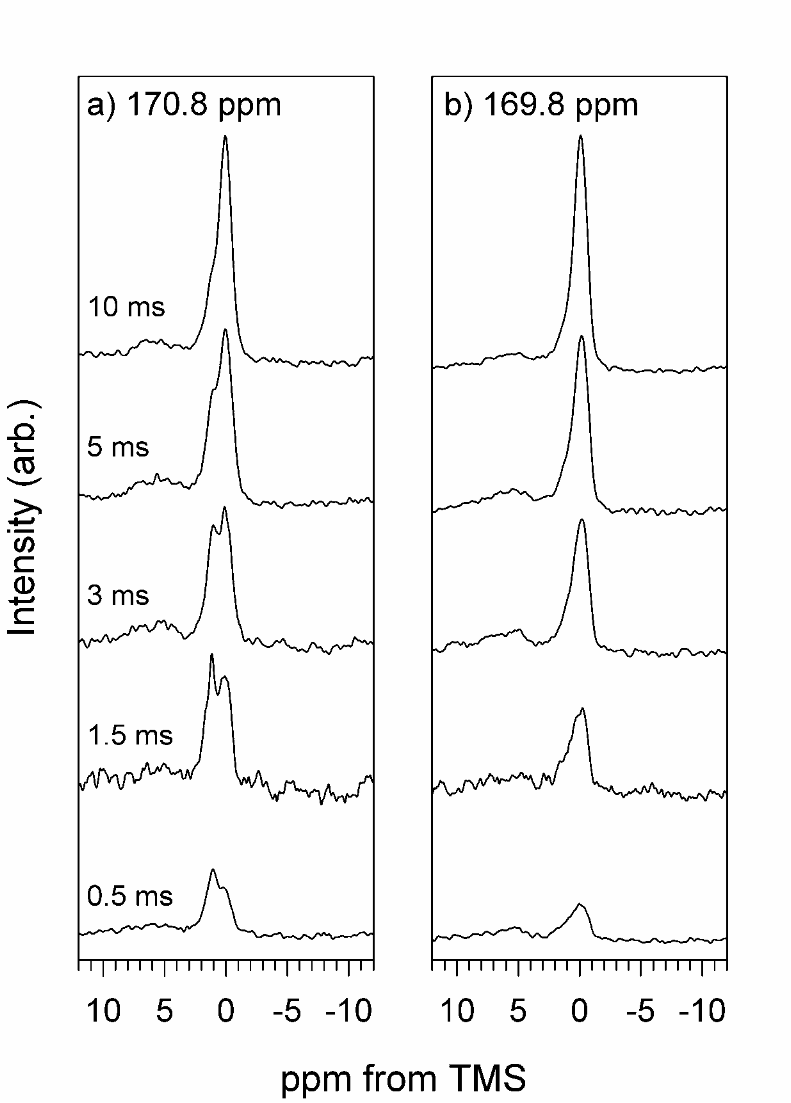

Figure 4.5. ^{1}H Traces (F1) from 2-dimensional ^{13}C{^{1}H} HetCor spectra of AK-5H taken at the indicated contact times, corresponding to the cross sections at the main ^{13}C peak positions in F1 at **a)** $\delta_{C\text{-}13}$ = 170.8 ppm, and **b)** 169.8 ppm. Spectra are scaled to reflect absolute intensity per scan.

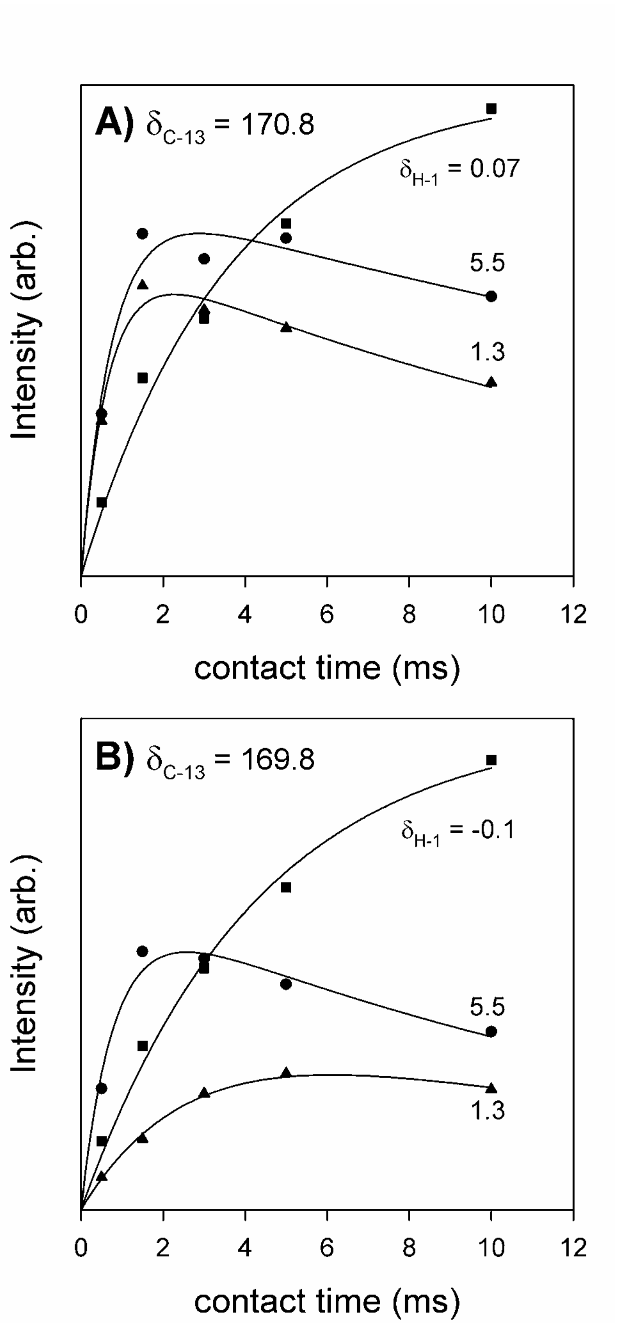

Figure 4.6. Variation in the cross-peak intensity of the $^{13}C\{^{1}H\}$HetCor NMR spectra taken of sample AK-5H for ^{1}H slices taken at **A)** $\delta_{13\text{-}C}$ = 170.8 ppm and **B)** 169.8ppm Symbols represent the integrated intensity for the ^{1}H sites at $\delta_{1\text{-}H}$ = 0.07 and -0.1 ppm (■), 1.3 ppm (▲) and 5.5 ppm (●). Lines represent a least-squares fit to classical CP dynamics.[25]

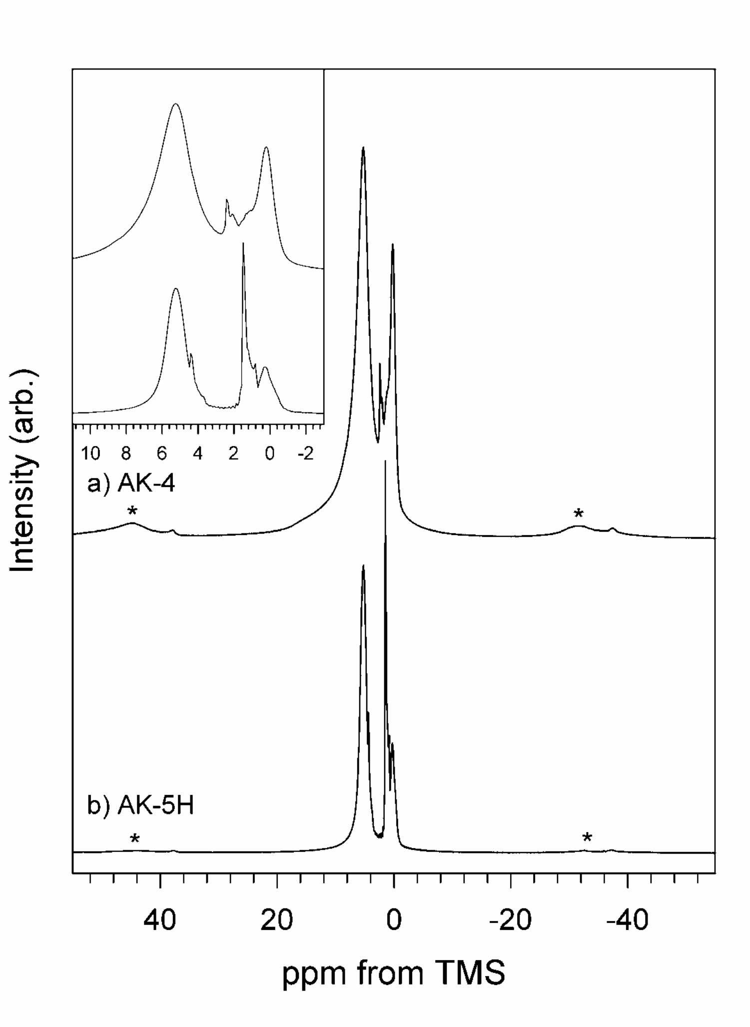

Figure 4.7. ^{1}H SP/MAS NMR spectra of CHAp samples **a)** AK-4 and **b)** AK-5H. Inset: Expanded view of the centerband region (11 to -3 ppm) of each spectrum. Each spectrum was collected with a 1 s relaxation delay at a spinning rate of 15 kHz for 128 and 512 acquisitions respectively. Asterisks denote spinning sidebands.

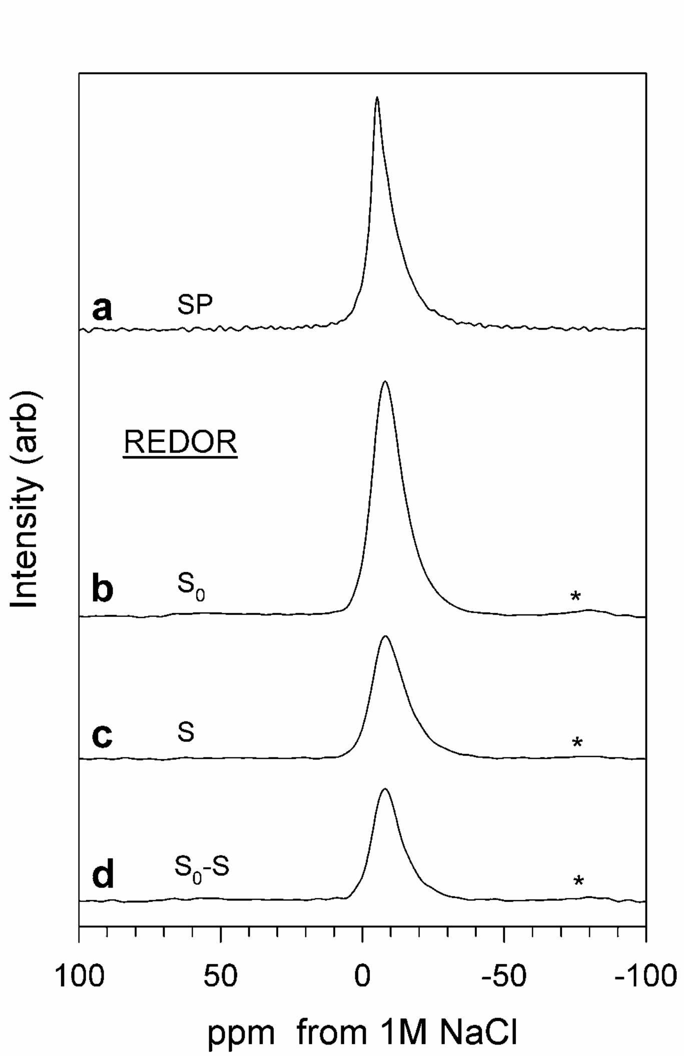

Figure 4.8. ^{23}Na NMR spectra of sample AK-5H **a)** ^{23}Na SP MAS NMR spectrum collected at a spinning rate of 18 kHz and pulse delay of 0.5 s. **b-d)** ^{23}Na{^{31}P} REDOR spectra set collected at 7 rotor-cycle echo delay using a spinning rate of 10 kHz and a pulse delay of 0.5 s. **b)** ^{23}Na Echo control spectrum, S_0. **c)** ^{23}Na{^{31}P} REDOR spectrum, S. **d)** Difference Spectrum, S_0-S. Spectra are scaled to reflect the absolute intensities. Asterisks denote spinning sidebands.

10. Supporting Information

Table SI-4.1. CP kinetic values obtained for the ^{1}H HetCor cross peaks. $T_{1\rho,H}$ values reported are apparent values. *value fixed to obtain valid fit.

δ_{C-13}	δ_{H-1}	I_0 (%)	T_{CH} (ms)	$T_{1\rho,H}$ (ms)
169.8	-0.1	0.42(1)	4.3(1)	>100*
	1.3	0.22(3)	2.7(3)	18(2)
	5.5	0.31(2)	0.8(2)	17(1)
170.8	0.07	0.53(1)	4.3(1)	>100*
	1.3	0.24(1)	0.7(1)	18(1)
	5.5	0.23(3)	0.8(3)	12(2)

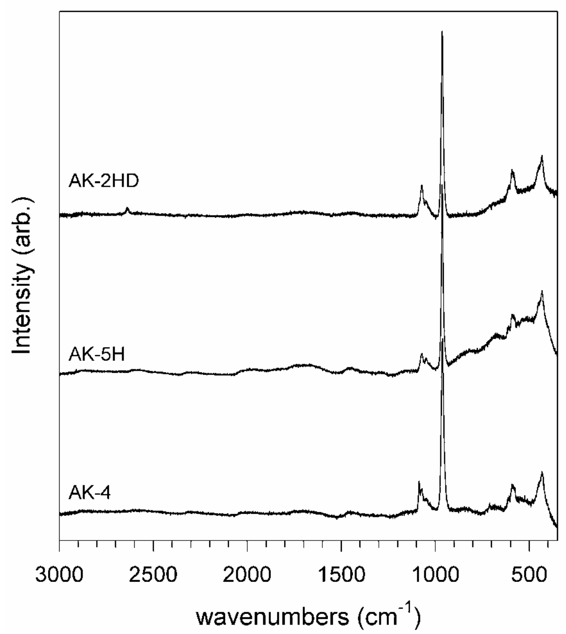

Figure SI-4.1. Raman Spectra of CHAp samples from top to bottom: AK2HD, AK-5H, and AK4.

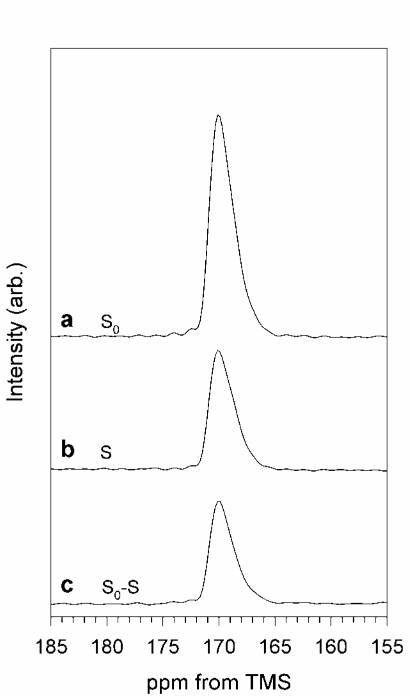

Figure SI-4.2. ^{1}H→ ^{13}C{^{31}P} CP/REDOR spectra set collected at 10 rotor-cycle echo delay using a spinning rate of 5 kHz and a pulse delay of 2 s. **a)** ^{13}C CP/echo control spectrum, S_0. **d)** ^{13}C{^{31}P} CP/REDOR spectrum, *S*. **d)** Difference Spectrum, S_0-S. Spectra **c-d** are scaled to reflect the absolute intensities.

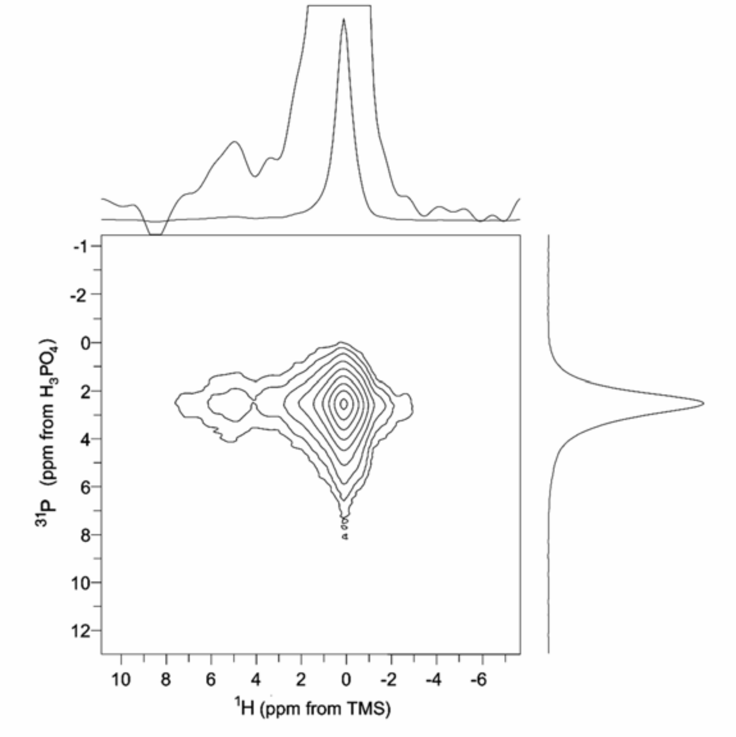

Figure SI-4.3. 2-dimensional $^{31}P\{^{1}H\}$ HetCor spectrum of AK-5H sample at a contact time of 7 ms and a spinning rate of 10 kHz. Spectra at top and side are summed projections. Top trace is shown at 10 times vertical scaling.

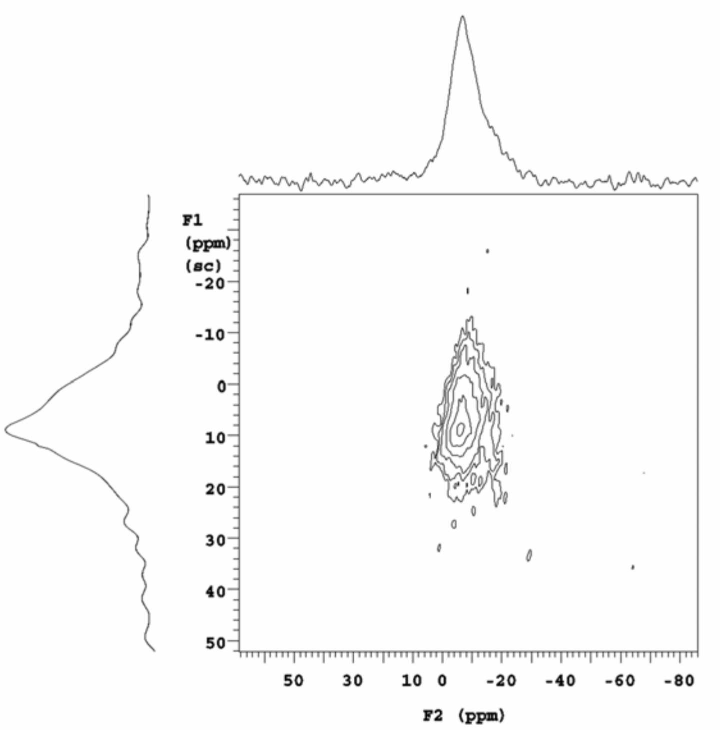

Figure SI-4.4. 2-dimensional ^{23}Na MQMAS spectrum of AK-5H sample at a spinning rate of 15 kHz. F2 corresponds to the normal MAS dimension where F1 corresponds to the isotropic dimension. Spectra at top and side are summed projections.

V. Solid-State NMR and IR spectroscopic investigation of the role of structural water and F in carbonate-rich fluorapatite

Reproduced with permission from American Mineralogist
Harris E. Mason[1,2,], Francis M. McCubbin[1], Alexander Smirnov[3], Brian L. Phillips[1,2], . Solid-State NMR and IR spectroscopic investigation of the role of structural water and F in carbonate-rich fluorapatite, Am. Mineral. 94(2009) 507-516, doi: 10.2138/am.2009.3095*

[1]*Department of Geosciences, State University of New York, Stony Brook, NY 11794-2100*
[2]*Center for Environmental Molecular Science, State University of New York, Stony Brook, NY 11794-2100*
[3]*Geophysical Laboratory, Carnegie Institution for Science, 5251 Broad Branch Rd. NW, Washington, DC 20015; current address: Department of Geosciences, State University of New York, Stony Brook, NY 11794-2100*

1. Abstract

We have studied the substitutions in a natural well-crystallized carbonate-containing apatite (Ca,F) (var. staffelite) using infra-red (IR) and solid-state nuclear magnetic resonance (NMR) spectroscopic techniques. Our results show the presence of both A and B-type carbonate plus a large amount of structural water (0.44 pfu). This sample also contains 0.21 per formula unit excess F, but only weak C-F dipolar coupling is observed indicating that a tetrahedral CO_3F^{3-} complex does not occur. ^{19}F NMR results indicate the presence of a second F environment in the apatite structure at a concentration similar to that of B-type carbonate but which does not differ from channel F in terms of coupling to ^{31}P or ^{1}H.

2. Keywords

Apatite (Ca,F), IR spectroscopy, NMR spectroscopy

3. Introduction

Phosphorite deposits account for less than 10% of the total budget of oceanic phosphorus deposition, but they represent a significant source of economically viable phosphorus due to phosphate contents commonly exceeding 9 wt.% as PO_4^{3-} (up to 27 wt.%) [1]. Although there are many means by which phosphorite deposits form, they share a common primary mineralogy, carbonate-rich apatite (Ca,F) (CFAp). Despite CFAp being ubiquitous among phosphorite deposits, little is known about the crystal chemical relationships governing the incorporation of the carbonate ion. Carbonate contents of CFAp from phosphorite deposits can range up to but typically do not exceed 6 wt.% as CO_3^{2-} [2]. Adding to its complexity, CFAp commonly contains an excess of fluorine (> 1.0 per structural formula unit [pfu]) that positively correlates with carbonate content [3, 4] in many but not all samples [5]. Because the apatite structure is very adaptive and many cationic and anionic substitutions can occur [6], the crystal chemical relationships governing carbonate incorporation into CFAp are likely complex. However, the species that accompany carbonate and their relative abundances have been suggested as key indicators for determining the petrogenetic history of the phosphorite [2]. Therefore, knowledge of the substitutions that accompany carbonate in apatite is necessary for full understanding of the process of phosphorite deposition and diagenesis.

Two primary sites for carbonate incorporation have been identified in the apatite structure [7, 8]. The carbonate ion can replace a channel anion (A-type substitution) with its plane parallel to the c-axis. Alternatively, carbonate can occupy a phosphate site (B-type substitution) by aligning its plane at 30 to 40 degree angle to the c-axis [9]. A- and B-type substitutions can exist independent of one another, or they can occur simultaneously as an AB-type substitution. These substitutions yield structural and charge imbalances which must be accommodated. For example, AB-type substitutions in apatite (Ca,OH) can be coupled in adjacent channel and phosphate sites through the incorporation of Na and hydrogen carbonate [10-12]. In apatite (Ca,F), the carbonate substitution is not well understood and has spurred debate over the role of fluorine. It is recognized that B-type carbonate content correlates with the amount of excess F in natural CFAp samples. This observation was extended to a proposed B-type substitution of a tetrahedral CO_3F^{3-} complex that replaces phosphate (e.g. [3, 13]). Regnier et al [14] suggested that the CO_3F^{3-} complex could not occur in CFAp based on comparisons of solid-state ^{13}C nuclear magnetic resonance (NMR) spectra of natural and synthetic CFAp to calculated NMR lineshapes for CO_3 with F at differing distances. The calculated static lineshape for a tetrahedral CO_3F^{3-} complex would differ significantly from that of a planer CO_3 molecule. However, Nathan [15] commented that the samples studied by Regnier et al [14] lacked excess F and, therefore, were not expected to contain CO_3F^{3-}. Little direct evidence has been found to support the existence of a tetrahedral CO_3F^{3-} complex, but it persists as a proposed substitution method in the literature (e.g., [6]). An additional B-type substitution mechanism was recently suggested by Nokhrin et al [16] based on electron paramagnetic resonance spectroscopy indicating charge balance was achieved in CFAp by the presence of vacancies in neighboring Ca, O, and F sites. Using NMR spectroscopy several recent studied have reported the occurrence of H-bearing species such as hydrogen phosphate, structural water, and bicarbonate can all substitute into the apatite structure [12, 17, 18]and it is possible that such species could also balance carbonate substitution in CFAp.

In this study we have analyzed a well-crystalline sample of CFAp (var. staffelite) from Staffel, Germany. There are no clear distinctions chemically or structurally between the staffelite and francolite varieties of apatite (Ca,F), but since the composition of CFAp varies widely (McArthur, 1985) we use the varietal term throughout to distinguish the specimens studied here. We have applied electron microprobe analysis (EMPA), Fourier Transform Infrared Spectroscopy (FTIR) and a variety of single, and double resonance solid-state NMR spectroscopic methods to determine the substitutions that accompany carbonate substitution in staffelite These results indicate that H has an integral role in the incorporation of carbonate into the apatite (Ca,F) structure through a coupling with molecular water. A second F environment is also clearly observed in NMR spectra indicating that it is related to carbonate substitution in F-rich apatite.

4. Methods

4.1 Samples and Synthesis

The natural CFAp sample analyzed in this study is a well-crystalline carbonate-rich apatite (Ca,F) (var. staffelite) from a phosphorite deposit in Staffel, Germany. This sample occurs as massive groups of apatite grains that appear to be annealed at grain boundaries (Fig. 5.1A,B). Individual grains within the massive groups are subhedral to anhedral and are typically ~100 μm in their longest dimension with typical aspect ratios of ~ 2:1; however the apatite grains decreased in size to ≤10 μm at the interface between the massive grains and the host material. The apatite had some impurity phases within, including hematite and phengite, although these impurities were not common. The apatite grains commonly contained small fluid inclusions, which were avoided during micro-FTIR analysis. Published carbonate contents for samples from this locality range from 4 to 7 wt% CO_3 [19-21].

A carbonate-bearing apatite (sCFAp) was synthesized following a method first developed for synthesis of carbonate-bearing apatite (Ca,OH) by Nelson and Featherstone [7] and later adapted and described by Mason et al. [12]. Briefly, a solution containing 0.2 M $(NH_4)_3PO_4$, 0.06 M $NaHCO_3$, and 0.06M NaF was titrated into a solution containing 0.2 M $Ca(NO_3)_2$ at a constant rate of 0.55 ml/min. The pH of the resulting solution was maintained between 8.5 and 9.0 by periodic manual additions of 10 N NaOH. The solid was then collected, centrifuged, rinsed twice in D.I. water, and transferred to a PTFE-lined hydrothermal vessel containing 0.5 M $NaHCO_3$, and 1.0 M NaF and heated at 220 ºC for a period of two days where the sample was allowed to recrystallize under autogenous pressure. The product was again collected and rinsed twice with D.I. water and characterized using X-ray powder diffraction to determine phase purity.

4.2. Analytical Methods

Powder X-ray diffraction (XRD) patterns of the samples were collected using Cu Kα radiation over the range of 20º to 80º 2θ using a 0.02º step scan on a Scintag PADX powder X-ray diffractometer. The XRD patterns were indexed, and unit cell parameters derived using the program UnitCell [22]. Fourier Transform infrared (FTIR) spectra were collected over a range of 670 to 4000 cm^{-1} on a Nicolet 670 FTIR spectrometer in adsorption mode. Samples were ground in an agate mortar with spectroscopic grade KBr in an approximate 1:300 ratio of sample to KBr and spectra were collected for 128 scans at a resolution 1 cm^{-1}. An attenuated total reflectance (ATR) FTIR spectrum was also collected from 360 to 7400 cm^{-1} on a Thermo Fisher Nicolet 6700 FTIR spectrometer equipped with a SmartOrbit ATR accessory with a Type IIa diamond ATR element.

Infrared spectroscopic measurements were also conducted at room-temperature in transmittance mode on a Thermo Nicolet Nexus 670 FTIR spectrometer attached to a Thermo Nicolet Continuum IR microscope located in the Department of Earth and Planetary Sciences at the American Museum of Natural History. Both the spectrometer and the IR objective were purged with dry nitrogen gas at a rate of 15 l/min. Transmittance IR spectra were collected from a doubly polished wafer of the staffelite sample over the mid-IR (1400-4000 cm^{-1}) to near-IR regions (3700-7500 cm^{-1}) using a KBr beam splitter, MCT/A detector, and globar source. Approximately 400 scans were performed for each IR spectrum acquired at a resolution of 4 cm^{-1}. The wafer was measured in 8 spots with a spot size of ~50 μm^2. All spots were first assessed optically to ensure the absence of impurity phases and fluid inclusions.

Thermogravimetric (TG) analyses were conducted using a Netzch STA 449 C Jupiter thermo-microbalance. 9.8 mg of powdered sample was loaded into an alumina crucible and heated at a rate of 20 °C/min. The analyses ramped from room temperature to 250 °C and cooled twice before collecting the full TG curve out to 1400 °C to ensure surface adsorbed water and fluid inclusions were removed prior to the full analysis. A background of the empty crucible was also collected following the same procedure prior to collection of the staffelite TG curve which was subtracted from the final data.

Electron Probe Microanalyses (EPMA) of the staffelite was performed at the Geophysical Laboratory of the Carnegie Institution for Science in Washington DC using a JEOL JXA-8800L microprobe equipped with five wavelength dispersive spectrometers and a liquid N_2-cooled Sapphire Si(Li) EDS detector (EDAX). An accelerating voltage of 15 kV and a nominal beam current of 20 nA were used for all analyses. A basaltic glass (Basalt-812) was used as a standard for magnesium and sodium. Durango-apatite was used as a standard for calcium, phosphorus, and fluorine. Because anisotropic diffusion of fluorine can occur during EPMA analyses down the c-axis of apatite ([23], care was taken to standardize along the a-axis of the Durango apatite; counts/s^2 were also monitored to ensure that count "acceleration" did not occur during standardization (after[24]). Analyses were conducted using a defocused beam with spot sizes of ~20 μm^2. Because identification of the crystallographic axes was not possible for the staffelite apatite, the fluorine numbers presented in Table 5.1 should be considered upper limits.

^{1}H, ^{31}P, and ^{13}C NMR spectra were collected on a 400 MHz Varian Inova spectrometer at operating frequencies of 399.76, 161.83, and 100.57 MHz, respectively. The ^{1}H Single Pulse magic angle spinning (SP/MAS) NMR spectra were collected at a spinning rate of 15 kHz on a Chemagnetics probe configured for 4 mm (o.d.) rotors and modified to yield a very low ^{1}H background signal; this background is insignificant compared to signal from the samples and was not subtracted from the spectrum. ^{13}C SP and ^{13}C{^{1}H} Cross-polarization (CP) MAS spectra were acquired with a Varian/Chemagnetics probe configured for 7.5 mm (o.d.) rotors. For ^{31}P{^{1}H} 2-dimensional (2-d) Heteronuclear Correlation (HetCor) spectra, a total of 50 hypercomplex points in *t*1 were collected with a 10 μs increment, corresponding to a 100 kHz F1 spectral window, using a 10 kHz spinning rate and a Varian/Chemagnetics 3.2 mm T3 probe assembly. The ^{1}H spectra were referenced to tetramethylsilane (TMS) by setting the hydroxyl resonance in reagent grade apatite (Ca,OH) to $\delta_H = 0.2$ ppm [25]. ^{13}C spectra were referenced to TMS using adamantane as an external reference set to $\delta_C = 38.6$ ppm [26]. The ^{1}H dimension in the ^{31}P{^{1}H} HetCor were referenced to ^{31}P{^{1}H} HetCor spectrum of apatite (Ca,OH) obtained using the same F1 acquisition and processing parameters.

^{19}F SP/MAS, ^{19}F{^{31}P} REDOR, ^{31}P{^{19}F} HetCor and ^{13}C{^{19}F} CP/MAS NMR spectra were collected on a 500 MHz Infinity Plus spectrometer at operating frequencies of 125.70, 202.32, and 470.21 MHz for ^{13}C, ^{31}P, and ^{19}F respectively using a Varian/Chemagnetics probe configured for 3.2 mm (o.d.) rotors and to give a very low ^{19}F background. ^{19}F{^{31}P} REDOR spectra were collected at a variety of dephasing periods using spinning rates of 20 and 25 kHz and spin-echo pulses for ^{19}F ($\pi = 12$ μs) and 12 μs re-coupling pulses for ^{31}P. For ^{31}P{^{19}F} HetCor spectra a total of 100 hypercomplex points in *t1* were collected at a 10 μs increment, corresponding to a 100 kHz spectral window in F1 at a spinning rate of 13 kHz. ^{13}C{^{19}F} CP/MAS spectra were collected at a spinning rate of 10 kHz using a variable a amplitude linear ramp to optimize signal intensity. ^{19}F{^{1}H} REDOR

NMR spectra were collected at the Keck NMR Center for Structural Biology in Stony Brook University using a 4mm H/F/X probe on a Bruker Advance 600 MHz spectrometer operating at frequencies of 600.13 and 564.63 MHz for ^1H and ^{19}F respectively. ^{19}F spectra were referenced with respect to $\delta_F = 0$ for $CFCl_3$ or 142 ppm for C_6F_6.

5. Results

5.1. XRD

X-ray powder diffraction patterns taken of both the staffelite and sCFAp samples indicate that pure apatite phases are present in both samples with no major impurity phases (Fig. 5.2). Additionally, both patterns can be indexed to the space group $P6_3/m$ with unit cell parameters of a = 9.35493(41) Å, c = 6.88659(39) Å and a = 9.36715(41) Å, c = 6.88289(39) Å for the staffelite and sCFAp samples respectively. These values indicate a contraction of the a-axis with respect to pure apatite (Ca,F) with carbonate substitution similar to that reported previously for apatite (Ca,OH) (eg. [27, 28]).

5.2. Elemental Analysis

The EPMA results of the staffelite are summarized in Table 5.1. Before EPMA analysis, the staffelite sample was inspected by electron dispersive spectroscopy (EDS) in order to identify which elements should be included in the analytical setup. This was executed to ensure that the low sums obtained could be attributed only to the presence of C- and H-species (and some matrix effects), which could not be detected by EDS. Mg and Na were the only minor structural constituents detected, and they represent a very minor structural component (Na + Mg < 0.05 pfu). The paucity of Na in the staffelite indicates that unlike carbonate-rich apatite (Ca,OH), Na does not play an important role in the carbonate incorporation of this sample (cf. Fleet and Liu, 2007a; Mason et al., 2008). All of the analyses from Table 5.1 have F-contents in excess of 1 pfu (> ~3.79 wt.% F), however this may be an artifact of the analytical technique [23].

5.3. Vibrational Spectroscopy

The powder FTIR spectrum (Fig. 5.3) of the staffelite contains peaks characteristic of carbonate-bearing apatite [7, 8, 12, 29]. Compared with more-studied carbonate-rich apatite (Ca,OH), some difference the CO_3 modes are observed that can be attributed to the influence of F. No significant difference in the positions of the B-type CO_3 ν_2 peaks from CHAp are observed, however, there are changes in the A-type ν_2 region where a slight down-frequency shift of the A-type CO_3 ν_2 peak from 872 cm^{-1} to 865 cm^{-1} is observed. In the CO_3 ν_3 region peaks are observed at 1451 cm^{-1} and 1426 cm^{-1} for staffelite, very similar to those observed for carbonate-rich apatite (Ca,OH). These results agree well with previous studies that indicated a shift to lower wavenumbers of the CO_3 ν_2 peaks with increasing F-content while no significant changes are observed for other modes [14, 30-33]. The ATR spectrum of this sample (not shown) exhibits the same features observed in the powder FTIR spectrum, but since it was collected from over a greater frequency range it was possible to measure the intensity of the CO_3 mode at 565 cm^{-1} from which an estimate for the total CO_3 content of 4.6 wt% was obtained using the method of Krajewski et al., [27].

Micro-IR measurements (Fig. 5.3) were obtained to further characterize the water modes from the staffelite, the presence of which was suggested from the NMR data (see below). Following the assignments of Mandeville et al. [34] we assigned three peaks, at 5168 cm^{-1} (not shown in Fig. 5.3), 3380 cm^{-1}, and 1630 cm^{-1} to various water modes. Those at 1630 cm^{-1} (Fig. 5.3c.) are assigned to HOH bending modes typical for molecular H_2O and those at 5168 cm^{-1} and 3380 cm^{-1} is assigned to OH-stretching and HOH-bending overtones. However, the characteristic narrow peak at 3570 cm^{-1} typically assigned to OH contained in the apatite channels is notably absent from this spectrum. Therefore, it appears that the modes associated with H in this structure are dominated by the presence of molecular H_2O with little contribution from hydroxyl in the channels. Because care was taken to analyze areas free of inclusions, these results suggest that the molecular H_2O species are in the apatite structure and not associated with impurities. This interpretation is further supported by the $^{31}P/^{1}H$ double resonance NMR results discussed in subsequent sections. We observe a strong set of peaks at 2936 cm^{-1} and 2887 cm^{-1} which have previously been attributed to hydrogen carbonate groups [12]. $^{13}C/^{1}H$ NMR results discussed below suggest hydrogen carbonate is absent, but $^{31}P/^{1}H$ NMR experiments show the presence of hydrogen phosphate groups. Therefore, we infer that these peaks could arise from protonated phosphate

5.4. Thermogravimetric analysis

The initial portion of the TG curve from 250 to 360 °C is flat after the initial ramped heating indicating the complete removal of surface water and fluid inclusions. Three gradual weight loss events are also observed for the staffelite sample (Fig. 5.4). The first is a loss of 1.6 wt% which occurs from 360 to 808 °C which likely corresponds to the loss of structural water. This interpretation is supported by ^{1}H NMR of this sample (see below). The second, and largest weight loss is 3.39 wt% which corresponds to the loss of CO_2 from the apatite structure and corresponds to 4.62 wt% CO_3. This value agrees well with that derived from the ATR spectrum. The final weight loss corresponds to only 0.77% and appears to continue beyond the range of the collected data. It is unclear what this loss corresponds to but NMR data collected for similarly treated material indicate partial decomposition.

5.5. ^{31}P MAS NMR

The ^{31}P SP/MAS NMR spectrum of the staffelite sample exhibits only a single narrow peak at $\delta_P = 2.6$ ppm (Fig. 5.5a). This result agrees with earlier studies that place the chemical shift for apatite within the range of 2.5 to 2.8 ppm with no systematic variation with channel anion [35, 36]. $^{31}P\{^{1}H\}$ CP/MAS experiments (Fig. 5.5b) produce a lineshape consisting of three main components: a shoulder at 0.6 ppm (1.2 ppm full-width at half-maximum; FWHM), a sharp component at 2.6 ppm (1.2 ppm FWHM), and a broad component at 3.0 ppm (5.9 ppm FWHM). The existence of the broad component is supported by variable contact time experiments in which an increased sharpening of the overall lineshape with increasing contact time can be simulated by changes in the relative intensities of a narrow and broad component. Detailed examination of the CP dynamics (intensity variation as a function of contact time) reveals that the broad peak at 3.0 ppm and the shoulder at 0.6 ppm exhibit short T_{PH} values of 0.5 and 0.9 ms respectively and decay with $T_{1\rho,H}$ values of 27 and 7 ms respectively. The peak at 2.6 ppm, however, has a T_{PH} value greater than 2 ms and continues to intensify with increasing contact time beyond 20 ms, indication a very long $T_{1\rho,H}$. This result indicates that the peak at 2.6 ppm represents bulk phosphate groups far removed from H, and the peaks at 0.5 and 3.0 ppm correspond to phosphate closely associated with H in the structure, possibly either in the form of hydrogen phosphate or structurally bound H_2O.

5.6. ^{1}H MAS NMR

The ^{1}H SP/MAS spectrum of the staffelite (Fig. 5.6a) contains a broad peak at δ_H = 5.6 ppm (3.6 ppm FWHM), a narrow peak at 1.6 ppm (1.6 ppm FWHM), plus a set of spinning sidebands (SSB) centered at δ_H = 6.4 ppm (obtained by averaging the positions of the n = ±1, ±2 SSB). The peaks at 5.6 ppm and the broad SSB pattern at 6.4 ppm correspond to distinct H species although both chemical shifts are consistent with molecular water [37, 38]. The broad SSB pattern indicates that the water species represented by the peak at 6.4 ppm is rigid and, therefore, likely bound in the apatite. The peak at 5.6 ppm lacks significant SSB intensity and is assigned to water contained in fluid inclusions. The chemical shift of the narrow peak, 1.6 ppm, corresponds well to that reported previously for hydroxyl groups in hydroxyl-rich apatite (Ca,F) [39]. Spectral integration indicates that hydroxyl account for only 6% of the H in this sample.

^{1}H NMR spectra of heat-treated portions of the staffelite support the assignment of the first weight loss in the TG curve to evolution of the structural water. The ^{1}H spectra collected for a sample heated to 200 ºC for an excess of 8 hrs (Fig. 5.7b) displays the peaks at δ_H = 5.6, 6.4 and 1.6 ppm observed for untreated staffelite. A sharpening of the structural water peaks is observed for this sample which could be due to mobilization of the H_2O. This treatment was similar to that used to achieve a flat initial baseline in the TG curve. Comparison of spectra before and after heating is consistent with loss of only surface sorbed water, intergranular water, and fluid inclusions over this temperature range, retaining the structural water. A sample heated to 600 ºC to correspond with the middle of the first TG weight loss produces a spectrum (Fig. 5.7c) in which the broad water peaks at δ_H = 5.6 and 6.4 ppm are decreased, but can still be observed clearly in the spinning sidebands indicating incomplete dehydration. The peaks for hydroxyl at 1.6 ppm and hydrogen phosphate at 10 ppm remain unaltered. A small peak at 4.7 ppm is observed but likely results from water quickly sorbed to the surface during rotor packing. Spectra of a sample heated to the end point of the first weight loss (800 ºC; not shown) is similar but shows evidence of partial decomposition and a shift of the hydroxyl peak suggests rearrangement of the channel.

5.7. $^{31}P\{^{1}H\}$ HetCor NMR

We used $^{31}P\{^{1}H\}$ HetCor NMR to determine which H species are associated with P in the staffelite. In this experiment the ^{1}H spectra are acquired indirectly through ^{31}P observation and correspond to H from which magnetization was transferred during CP, either through direct ^{1}H-^{31}P dipolar coupling or subsequent ^{1}H-^{1}H spin diffusion. A representative 2-d contour map with summed projections is shown in Figure 5.8. The ^{1}H slices and summed projections (Fig. 5.6b-e) indicate that two principal H environments are associated with P, represented by broad peaks at δ_H = 9.2 ppm (4.5 ppm FWHM) and 6.4 ppm (8.7 ppm FWHM). The spectra also appear to contain a feature corresponding to the hydroxyls near δ_H =1.6 ppm, but it is poorly resolved due to low intensity and overlap with broad peaks. The SSB pattern corresponds only to the peak at 6.4 ppm and is characteristic of rigid water molecules remote from other H [38]. Its occurrence in the ^{31}P-detected spectra shows that these water molecules are structural water in the apatite. The peak at 9.2 ppm is enhanced relative to that at 6.4 ppm at short contact times (cf. Fig. 5.5b and 5.5e) suggesting shorter distances to P and is resolved in spectra of the heat treated samples (Fig. 5.7b). It is similar in both position and width to that observed for HPO_4 defects in nano-crystalline apatite (Ca,OH) ([18, 40]. This chemical shift indicates a moderately strong hydrogen bond.

The ^{31}P sum projection over the ^{1}H centerband (Fig. 5.5c) shows a complex lineshape similar to that observed in variable contact time $^{31}P\{^{1}H\}$ CP/MAS spectra. A ^{31}P slice taken at δ_H = 9.2 ppm clearly resolves three peaks (Fig. 5.5d), including a sharp peak at δ_P = 5.0 ppm (1.0 ppm FWHM) and a shoulder at 0.6 ppm (0.9 ppm FWHM) in addition to the peak at 2.7 ppm (3.7 ppm FWHM). A ^{1}H slice taken at δ_P = 0.6 ppm shows similar spectral features as that of the ^{1}H sum projection (Fig. 5.6c), but the ^{1}H slice at δ_P = 5.0 ppm clearly shows the peak at δ_H = 9.2 ppm for HPO_4 is enhanced relative to the water peak at 6.4 ppm (Fig. 5.6d). These data allow us to assign the $^{31}P(5.0)/^{1}H(9.4)$ cross-peak to moderately hydrogen bonded HPO_4 defects in the apatite.

5.8. ^{19}F MAS NMR

The ^{19}F SP/MAS NMR spectrum of the staffelite (Fig. 5.9a) contains two distinct isotropic peaks, at δ_F = -86.6 ppm (5.3 ppm FWHM) and -99.8 ppm (4.0 ppm FWHM), each with broad spinning sideband envelopes. The peak at -99.8 ppm is similar to those reported previously for fluorine-containing apatite [41-43] and contains most of the spectral intensity (87.7%). The chemical shift anisotropy (CSA) measured for the peak at -99.8 ppm, with a span (Ω) of 83 ppm and a skew (κ) of -0.9 (δ_{11} = -45.8 ppm, δ_{22} = -124.7 ppm, and δ_{33} = -128.9 ppm), is similar to that reported previously for a pure apatite (Ca, F) [41], but that observed for the peak at -86.6 ppm is almost an exact mirror with Ω = 82 ppm and κ = 1.0 ($\delta_{11} = \delta_{22}$ = -59.5 ppm, and δ_{33} = -141.5 ppm. Similar peaks are also observed for the sCFAp sample at -86.6 and -100.5 ppm, but with narrower linewidths (1.9 and 1.3 ppm FWHM respectively) (Fig. 5.9b) and much lower intensity for the peak at -86.8 ppm. The sCFAp sample also exhibits peaks at -106.7 and -222.8 ppm corresponding to CaF_2 and NaF impurities [44]that are present at too low an abundance to be detected by our XRD scan. Two broader shoulders also occur at -97.0 and -99.8 ppm (6.7 and 2.5 ppm FWHM respectively), but could not be assigned and would not be apparent in the spectra of the natural sample due to the broad linewidths.

5.9. ^{19}F{^{31}P} REDOR

^{19}F{^{31}P} REDOR NMR spectra were obtained for the staffelite sample to investigate the connectivity between P and distinct F-sites observed in the ^{19}F SP/MAS spectrum. This experiment produces a ^{19}F spin-echo spectrum (S_0) that contains signal from all ^{19}F and a ^{19}F{^{31}P} REDOR spectrum (S) where, due to the recoupling of ^{19}F-^{31}P dipolar coupling, any ^{19}F peaks corresponding to ^{19}F associated with ^{31}P will have lower intensity. Subtraction of these spectra produces a difference spectrum (S_0-S) containing signal only from ^{19}F in close proximity to ^{31}P (< 5 Å). A typical ^{19}F{^{31}P} REDOR spectral set is shown in Figure 5.10. The peaks at both -86.6 and -99.8 ppm are present at similar intensity ratios in the spin-echo control (S_0), REDOR (S) and difference spectra (S_0-S) indicating that both are associated with P. Therefore, the peak at -86.8 ppm must correspond to an additional F-environment in the apatite and not an impurity phase.

The REDOR dephasing curves of the two ^{19}F peaks (Fig. 5.11) appear very similar indicating similar P-F distances. Quantitative comparison can be made by approximating the F are surrounded by P arranged in a trigonal plane and fitting the dephasing curve for $(S_0-S)/S \leq 0.60$ using a second order multi-spin approximation [45]. Assuming the same P geometry for both sites we derived F-P distances of 3.5 and 3.4 ± 0.2 Å for the peaks at -86.8 and -99.8 ppm respectively. These distances are in excellent agreement with the P-F distance of 3.6 Å in apatite (Ca,F) reported from XRD [46]. A similar conclusion could be drawn from $^{31}P\{^{19}F\}$ HetCor spectra (not shown) which contained cross-peaks for both ^{19}F resonances and showed no significant differences between the ^{19}F sum projection collected at short contact time (0.5 ms) and those collected at a contact time of 2 ms. These data indicate that there is no difference between these ^{19}F peaks in terms of their coupling to P.

5.10. $^{19}F\{^1H\}$ REDOR

Hydrogen bonding can have a large effect in ^{19}F chemical shifts, so $^{19}F\{^1H\}$ REDOR experiments were undertaken to investigate whether the peak at δ_F = -86.8 ppm arises from F engaged in hydrogen bond interactions with H. However, only minor differences in the REDOR fraction, $(S_0-S)/S_0$, are observed for the spectral set collected at 0.13 ms dephasing, with the peak at -86.8 ppm showing a slightly larger REDOR effect (9 %) than the -99.8 ppm peak (7 %). This difference decreases at longer dephasing periods and eventually the two peaks exhibit the same REDOR fraction at long (2.8 ms) dephasing periods. If the peak at -86.8 ppm were due to F weakly hydrogen bonded to H_2O (d(OH···F) = 1.9 Å) we would expect to observe a large $^1H\{^{19}F\}$ REDOR effect at shorter dephasing periods. Therefore, the occurrence of the peak at -86.8 ppm cannot be explained by a closer proximity to ^1H.

5.11. ^{13}C MAS NMR

^{13}C SP/MAS NMR spectra of the staffelite sample show two distinct peaks at 170.7 ppm (2.0 ppm fwhm) and 168.6 ppm (2 ppm fwhm) representing 76% and 24% of the intensity respectively (Fig. 5.12a). Following previous work, we assign the 170.7 ppm peak to B-type substitution and that at 168.6 ppm to A-type substitution [12, 47]. These assignments agree with the IR data (see above) in which distinct peaks are observed for both

A and B-type carbonate in the CO_3 ν_2 region. These ^{13}C peaks are also present in the $^{13}C\{^1H\}$ CP/MAS NMR spectra, but that at 168.6 ppm appears to be enhanced (Fig. 5.12b). In $^{13}C\{^{19}F\}$ CP/MAS NMR spectra only the peak at 170.7 ppm is apparent (Fig. 5.12c), but due to the low signal to noise it is hard to determine if there is any contribution from the peak at 168.6 ppm.

$^{13}C\{^{19}F\}$ CP/MAS NMR spectra collected at variable contact time show that the peak at δ_C = 170.7 grows with a T_{CF} value of 4.5 ms (Fig. 5.13) indicative of only relatively long C-F distances. We can compare this value to the apparent T_{PF} (2.4 ms, from $^{31}P\{^{19}F\}$ data obtained under similar conditions) by scaling the T_{PF} by a ratio of the gyromagnetic ratios of ^{31}P and ^{13}C, resulting in a predicted $T_{CF} \approx 3.9$ ms for F in the channel and C near the P position. Since the value of T_{CF} we observe is larger than the scaled T_{PF} the peak at δ_C =170.7 ppm must correspond to a carbonate environment with an average C-F distance somewhat greater than 3.4 Å. This result is consistent with B-type carbonate cross polarizing to channel F. Shorter distances, such as for a CO_3F^{3-} tetrahedron would give much shorter T_{CF} values. For comparison, isolated bicarbonate groups give apparent T_{CH} of ~0.7 ms [48].

6. Discussion

Combining the elemental analyses with the NMR results we derive a general structural formula which includes the A and B-type carbonate abundances:

$Ca_{4.97}Mg_{0.02}Na_{0.01}[(PO_4)_{2.77}(CO_3)_{0.23}][F_{1.12}OH_{0.01}(CO_3)_{0.08}] \bullet 0.42\ (H_2O)$

The ratio of Ca-site to P-site cations equals the crystallographic ratio 5:3, indicating that any substantial vacancy concentration on the Ca-site could be balanced by P-site vacancies. This formula contains a significant amount of H_2O, which NMR results clearly show as structural water, and a channel occupancy much greater than one pfu. Carrying no formal charge, the molecular water must serve a structural role in accommodating the defects in the apatite. Presence of H_2O in the channels would explain why we observe no significant $^{13}C\{^{19}F\}$ CP signal for A-type carbonate, but an increase in relative intensity for this peak in $^{13}C\{^1H\}$ CP/MAS spectra. These observations suggests that H_2O surrounds the A-type carbonate defect and effectively isolates it from the F also contained in the channels. The B-type carbonate substitution produces an oxygen vacancy leaving the Ca underbonded and H_2O could also provide a method for structurally balancing this vacancy. If both substitution H_2O

models are adopted it would be necessary to have twice the amount of H_2O as A-type carbonate (0.08 pfu) and an equivalent amount as B-type carbonate (0.23 pfu) giving a final H_2O amount of 0.39 pfu which agrees within error with the 0.42 pfu in the structural formula. Since the HPO_4^{2-} and OH contributions are small, the role of H in staffelite is structural, whereas in carbonate-rich apatite (Ca,OH) H largely serves to charge compensate carbonate substitution via coupled substitution of hydrogen carbonate and Na (Mason et al, 2008).

The average structural formula indicates that the channel anion site is overfilled by 0.21 pfu. Since both the A-type carbonate and OH likely reside in the channel site there is potentially 0.21 pfu excess F. This amount of excess F equals within experimental error the 0.23 pfu of B-type carbonate. Previous studies have noted correlations between F and carbonate content based on weight losses from thermal decomposition of the apatite and assuming that all CO_2 effluence results from B-type substitution [3, 13]. Our results would be consistent with charge-compensation of B-type carbonate by excess F, although spectroscopic data for more samples having different composition are needed. However, the observed $^{13}C\{^{19}F\}$ CP kinetics show that F is located at a distance greater than 3.5 Å from B-type carbonate, indicating lack of direct C-F interactions and that a tetrahedral CO_3F^{3-} complex does not occur in this staffelite.

The excess F in the staffelite appears related to the ^{19}F NMR peak observed at -86.8 ppm, which accounts for 12% of the total integrated spectral intensity. Given the broad line widths and large degree of peak overlap, this value corresponds approximately to the potential excess F in this sample (18% of the total F). Consequently, this second F-environment is likely related to B-type carbonate substitution and its appearance in the spectra of the synthetic sample shows that it is not unique to the staffelite composition. Despite an isotropic chemical shift and CSA that are substantially different from those for normal channel F, this peak does not show distinct coupling to either H or P, so very little can be said at this point about its structural environment. A similar peak was observed for a Sb-doped apatite (Ca,F) where its occurrence was attributed to F interacting with lone pair electrons of SbO_3^{3-} substituting in the phosphate site [49]. More work on a variety of ^{13}C-enriched carbonate-rich apatite (Ca,F) samples with varying carbonate and F contents is needed to better understand the role of this F species in balancing B-type carbonate substitution.

7. Acknowledgements

The authors would like to thank Dr. Timothy Glotch for assisting with the ATR measurements and Dr. Martine Zilox for help with the $^{19}F\{^{1}H\}$ REDOR experiments. This research was supported by the Center for Environmental Molecular Science (NSF CHE-0221934) and instrumentation provided by NSF CHE-03-21001. HM and FM were supported through U.S Dept. of Education sponsored GAANN fellowships (P200A060248)

8. References

[1] C.R. Glenn, K.B. Follmi, S.R. Riggs, G.N. Baturin, K.A. Grimm, J. Trappe, A.M. Abed, C. Galli-Oliver, R.E. Garrison, A.V. Ilyin, C. Jehl, V. Rohrlich, R.M.Y. Sadaqah, M. Schidlowski, R.E. Sheldon, H. Siegmund, Phosphorus and phosphorites: Sedimentology and environments of formation, Ecologae Geologicae Helvetiae 87(1994) 747-788.

[2] J.M. McArthur, Francolite Geochemistry - Compositional Controls during Formation, Diagenesis, Metamorphism and Weathering, Geochimica Et Cosmochimica Acta 49(1985) 23-35.

[3] G.H. McClellan, J.R. Lehr, Crystal Chemical Investigation of Natural Apatites, American Mineralogist 54(1969) 1374-&.

[4] J.D. Schuffert, M. Kastner, G. Emanuele, R.A. Jahnke, Carbonate-Ion Substitution in Francolite - a New Equation, Geochimica Et Cosmochimica Acta 54(1990) 2323-2328.

[5] A.M. Abed, K. Fakhouri, On the chemical variability of phosphatic particles from Jordanian phosphorite deposits, Chemical Geology 131(1996) 1-13.

[6] Y.M. Pan, M.E. Fleet, Compositions of the apatite-group minerals: Substitution mechanisms and controlling factors, Phosphates: Geochemical, Geobiological, and Materials Importance 48(2002) 13-49.

[7] D.G.A. Nelson, J.D.B. Featherstone, Preparation, Analysis, and Characterization of Carbonated Apatites, Calcified Tissue International 34(1982) S69-S81.

[8] Y. Suetsugu, I. Shimoya, J. Tanaka, Configuration of carbonate ions in apatite structure determined by polarized infrared spectroscopy, Journal of the American Ceramic Society 81(1998) 746-748.

[9] R.M. Wilson, S.E.P. Dowker, J.C. Elliott, Rietveld refinements and spectroscopic structural studies of a Na-free carbonate apatite made by hydrolysis of monetite, Biomaterials 27(2006) 4682-4692.

[10] M.E. Fleet, X. Liu, Coupled substitution of type A and B carbonate in sodium-bearing apatite, Biomaterials 28(2007) 916-926.

[11] M.E. Fleet, X. Liu, Hydrogen-carbonate ion in synthetic high-pressure apatite, American Mineralogist 92(2007) 1764-1767.

[12] H.E. Mason, A. Kozlowski, B.L. Phillips, Solid-State NMR Study of the Role of H and Na in AB-type Carbonate Apatite, Chemistry of Materials 20(2008) 294-302.

[13] G. Binder, G. Troll, Coupled Anion Substitution in Natural Carbon-Bearing Apatites, Contributions to Mineralogy and Petrology 101(1989) 394-401.

[14] P. Regnier, A.C. Lasaga, R.A. Berner, O.H. Han, K.W. Zilm, Mechanism of $(CO_3)^{2-}$ Substitution in Carbonate-Fluorapatite - Evidence from FTIR Spectroscopy, ^{13}C NMR, and Quantum-Mechanical Calculations, American Mineralogist 79(1994) 809-818.

[15] Y. Nathan, Mechanism of CO_3^{2-} substitution in carbonate-fluorapatite: Evidence from FTIR spectroscopy, C-13 NMR, and quantum mechanical calculations - Discussion, American Mineralogist 81(1996) 513-514.

[16] S.M. Nokhrin, Y. Pan, M.J. Nilges, Electron paramagnetic resonance spectroscopic study of carbonate-bearing fluorapatite: New defect centers and constraints on the incorporation of carbonate ions in apatites, American Mineralogist 91(2006) 1425-1431.

[17] G.Y. Cho, Y.T. Wu, J.L. Ackerman, Detection of hydroxyl ions in bone mineral by solid-state NMR spectroscopy, Science 300(2003) 1123-1127.

[18] C. Jager, T. Welzel, W. Meyer-Zaika, M. Epple, A solid-state NMR investigation of the structure of nanocrystalline hydroxyapatite, Magnetic Resonance in Chemistry 44(2006) 573-580.

[19] G.P. Brophy, J.T. Nash, Compositional Infrared and X-Ray Analysis of Fossil Bone, American Mineralogist 53(1968) 445-&.

[20] D. McConnell, A structural investigation of the isomorphism of the apatite group, American Mineralogist 23(1938) 1-19.

[21] E.B. Sandell, M.H. Hey, D. McConnell, The Composition of Francolite, Mineralogical Magazine 25(1939) 395-401.

[22] T.J.B. Holland, S.A.T. Redfern, Unit cell refinement from powder diffraction data: The use of regression diagnostics, Mineralogical Magazine 61(1997) 65-77.

[23] J.C. Stormer, M.L. Pierson, R.C. Tacker, Variation of F-X-Ray and Cl-X-Ray Intensity Due to Anisotropic Diffusion in Apatite during Electron-Microprobe Analysis, American Mineralogist 78(1993) 641-648.

[24] F.M. McCubbin, H. Nekvasil, B.L. Jolliff, P.K. Carpenter, R.A. Zeigler, D.H. Lindsley, Apatite from Apollo samples 14161 and 12033: Analytical hurdles and implications for relative fluorine and chlorine contents in late-stage lunar magmas and melts., Proceedings of the NLSI Lunar Science Conference, Moffett Field, California. Abstract #2127(2008).

[25] J.P. Yesinowski, M.J. Mobley, ^{19}F MAS-NMR of Fluoridated Hydroxyapatite Surfaces, Journal of the American Chemical Society 105(1983) 6191-6193.

[26] W.L. Earl, D.L. Vanderhart, Measurement of ^{13}C Chemical-Shifts in Solids, Journal of Magnetic Resonance 48(1982) 35-54.

[27] A. Krajewski, M. Mazzocchi, P.L. Buldini, A. Ravaglioli, A. Tinti, P. Taddei, C. Fagnano, Synthesis of carbonated hydroxyapatites: efficiency of the substitution and critical evaluation of analytical methods, Journal of Molecular Structure 744(2005) 221-228.

[28] R. Zapanta-Legeros, Effect of Carbonate on Lattice Parameters of Apatite, Nature 206(1965) 403-404.

[29] M.E. Fleet, X.Y. Liu, P.L. King, Accommodation of the carbonate ion in apatite: An FTIR and X-ray structure study of crystals synthesized at 2-4 GPa, American Mineralogist 89(2004) 1422-1432.

[30] A. Antonakos, E. Liarokapis, T. Leventouri, Micro-Raman and FTIR studies of synthetic and natural apatites, Biomaterials 28(2007) 3043-3054.

[31] M.E. Fleet, X. Liu, Accommodation of the carbonate ion in fluorapatite synthesized at high pressure, American Mineralogist 93(2008) 1460-1469.

[32] M. Okazaki, F-CO_3^{2-} Interaction in IR-Spectra of Fluoridated CO_3-Apatites, Calcified Tissue International 35(1983) 78-81.

[33] M. Okazaki, Crystallographic Morphology of Heterogeneous Fluoridated Carbonate Apatites, Journal of Dental Research 72(1993) 1285-1290.

[34] C.W. Mandeville, J.D. Webster, M.J. Rutherford, B.E. Taylor, A. Timbal, K. Faure, Determination of molar absorptivities for infrared absorption bands of H2O in andesitic glasses, American Mineralogist 87(2002) 813-821.

[35] P.S. Belton, R.K. Harris, P.J. Wilkes, Solid-State ^{31}P NMR-Studies of Synthetic Inorganic Calcium Phosphates, Journal of Physics and Chemistry of Solids 49(1988) 21-27.

[36] W.P. Rothwell, J.S. Waugh, J.P. Yesinowski, High-Resolution Variable-Temperature ^{31}P NMR of Solid Calcium Phosphates, Journal of the American Chemical Society 102(1980) 2637-2643.

[37] S.J. Gaffey, H_2O and OH in Echinoid Calcite - a Spectroscopic Study, American Mineralogist 80(1995) 947-959.

[38] J.P. Yesinowski, H. Eckert, G.R. Rossman, Characterization of Hydrous Species in Minerals by High-Speed ^{1}H MAS NMR, Journal of the American Chemical Society 110(1988) 1367-1375.

[39] J.P. Yesinowski, H. Eckert, Hydrogen Environments in Calcium Phosphates - ^{1}H MAS NMR at High Spinning Speeds, Journal of the American Chemical Society 109(1987) 6274-6282.

[40] Y.H. Tseng, Y. Mou, P.H. Chen, T.W.T. Tsai, C.I. Hsieh, C.Y. Mou, J.C.C. Chan, Solid-state P-31NMR study of the formation of hydroxyapatite in the presence of glutaric acid, Magnetic Resonance in Chemistry 46(2008) 330-334.

[41] M. Braun, P. Hartmann, C. Jana, ^{19}F and ^{31}P NMR Spectroscopy of Calcium Apatites, Journal of Materials Science-Materials in Medicine 6(1995) 150-154.

[42] F.M. McCubbin, H.E. Mason, H. Park, B.L. Phillips, J.B. Parise, H. Nekvasil, D.H. Lindsley, Synthesis and Characterization of low-OH- fluor-chlorapatite: A single-crystal XRD and NMR spectroscopic study, American Mineralogist 93(2008) 210-216.

[43] J.P. Yesinowski, M.J. Mobley, F-19 Mas-Nmr of Fluoridated Hydroxyapatite Surfaces, Journal of the American Chemical Society 105(1983) 6191-6193.

[44] B. Bureau, G. Silly, J.Y. Buzare, J. Emery, Superposition model for F-19 isotropic chemical shift in ionic fluorides: from basic metal fluorides to transition metal fluoride glasses, Chemical Physics 249(1999) 89-104.

[45] M. Bertmer, H. Eckert, Dephasing of spin echoes by multiple heteronuclear dipolar interactions in rotational echo double resonance NMR experiments, Solid State Nuclear Magnetic Resonance 15(1999) 139-152.

[46] M.E. Fleet, Y.M. Pan, Site preference of rare earth elements in fluorapatite: Binary (LREE+HREE)-substituted crystals, American Mineralogist 82(1997) 870-877.

[47] K. Beshah, C. Rey, M.J. Glimcher, M. Schimizu, R.G. Griffin, Solid-State ^{13}C and Proton NMR-Studies of Carbonate-Containing Calcium Phosphates and Enamel, Journal of Solid State Chemistry 84(1990) 71-81.

[48] J. Feng, Y. Lee, J.D. Kubicki, R.J. Reeder, B.L. Phillips, NMR Spectroscopy of Citrate in Solids: Cross-Polarization Kinetics in Weakly Coupled Systems, Magnetic Resonance in Chemistry 46(2008) 408-407.

[49] L.B. Moran, J.K. Berkowitz, J.P. Yesinowski, F-19 and P-31 Magic-Angle Spinning Nuclear-Magnetic-Resonance of Antimony(Iii)-Doped Fluorapatite Phosphors - Dopant Sites and Spin Diffusion, Physical Review B 45(1992) 5347-5360.

9. Tables

Table 5.1. Microprobe analyses for the Staffelite Sample

Oxide	Grain 1	Grain 2	Grain 3	Grain 4
MgO	0.14	0.11	0.12	0.13
CaO	51.91	52.15	51.82	52.15
Na_2O	0.06	0.08	0.07	0.08
P_2O_5	36.53	36.07	36.80	37.59
OH[†]	0.20	0.20	0.20	0.20
F	3.75	3.94	4.03	4.17
-O = F	1.58	1.66	1.70	1.76
CO_2[*]	3.39	3.39	3.39	3.39
H_2O[*†]	1.40	1.40	1.40	1.40
Total	95.83	95.69	96.13	97.38
Structural formulae based on 5 A-site cations[**]				
Mg	0.02	0.01	0.02	0.02
Ca	4.97	4.98	4.97	4.97
Na	0.01	0.01	0.01	0.01
P	2.76	2.72	2.79	2.83
A-type C	0.07	0.02	0.09	0.13
B-type C	0.24	0.28	0.21	0.17
OH	0.01	0.01	0.01	0.01
F	1.06	1.11	1.14	1.17
H_2O	0.42	0.42	0.42	0.42

[†] The H_2O/OH ratio was calculated from single pulse ^1H MAS NMR spectra of the Staffelite sample.

[*] Analyzed by TGA

[**] While apatite structural formulae are typically calculated on an anion basis, we normalized to 5 A-site cations because of the likelihood of excess anions in the structure. Normalizing to 5 A-site cations assumes no structural vacancies occur in either the A1 or A2 sites.

10. Figures and Captions

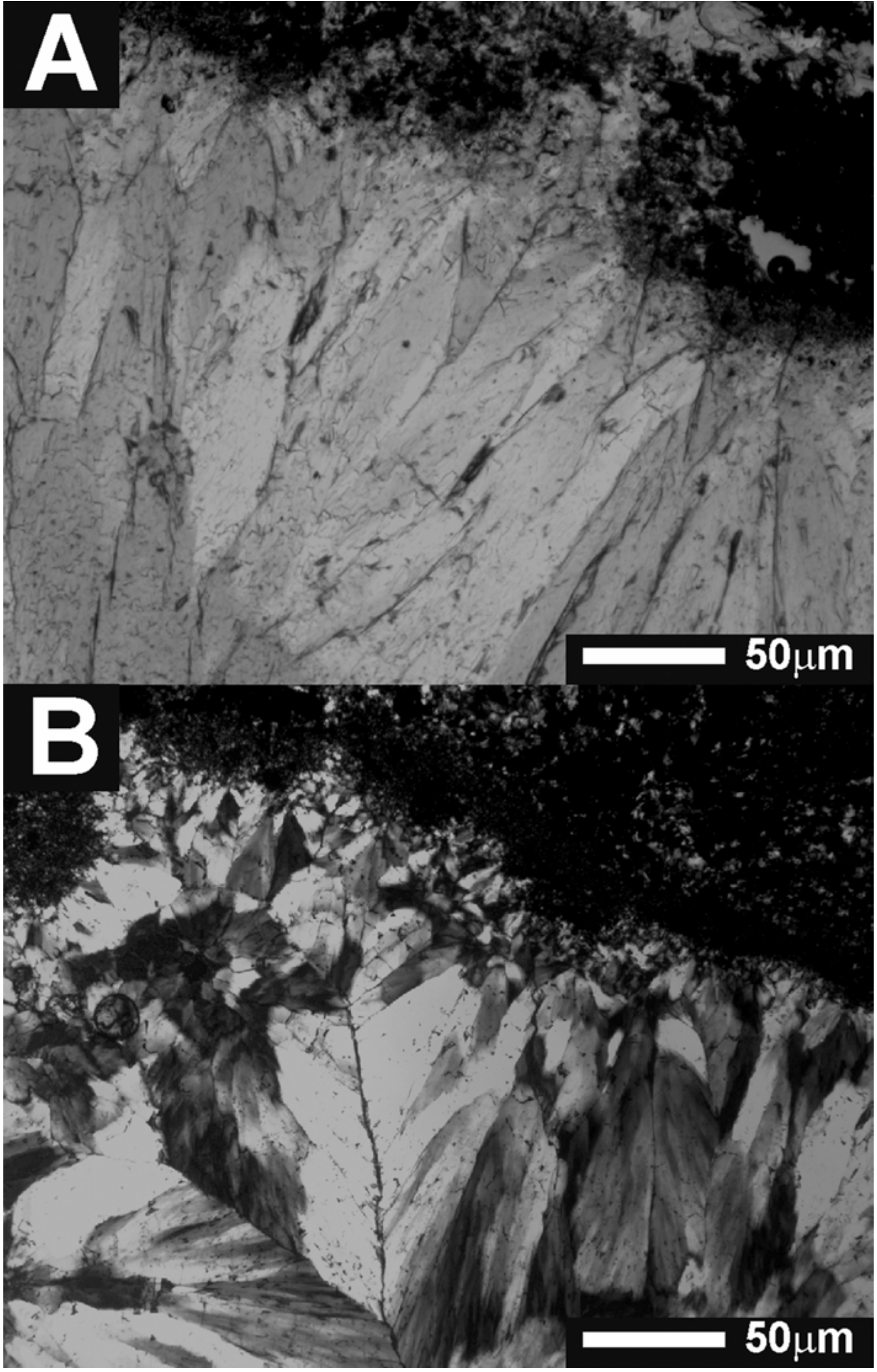

Figure 5.1. A) Plane polarized light image of a thin section of the staffelite sample along the host material interface. **B)** Cross_polarized light image of a thin section of the staffelite sample.

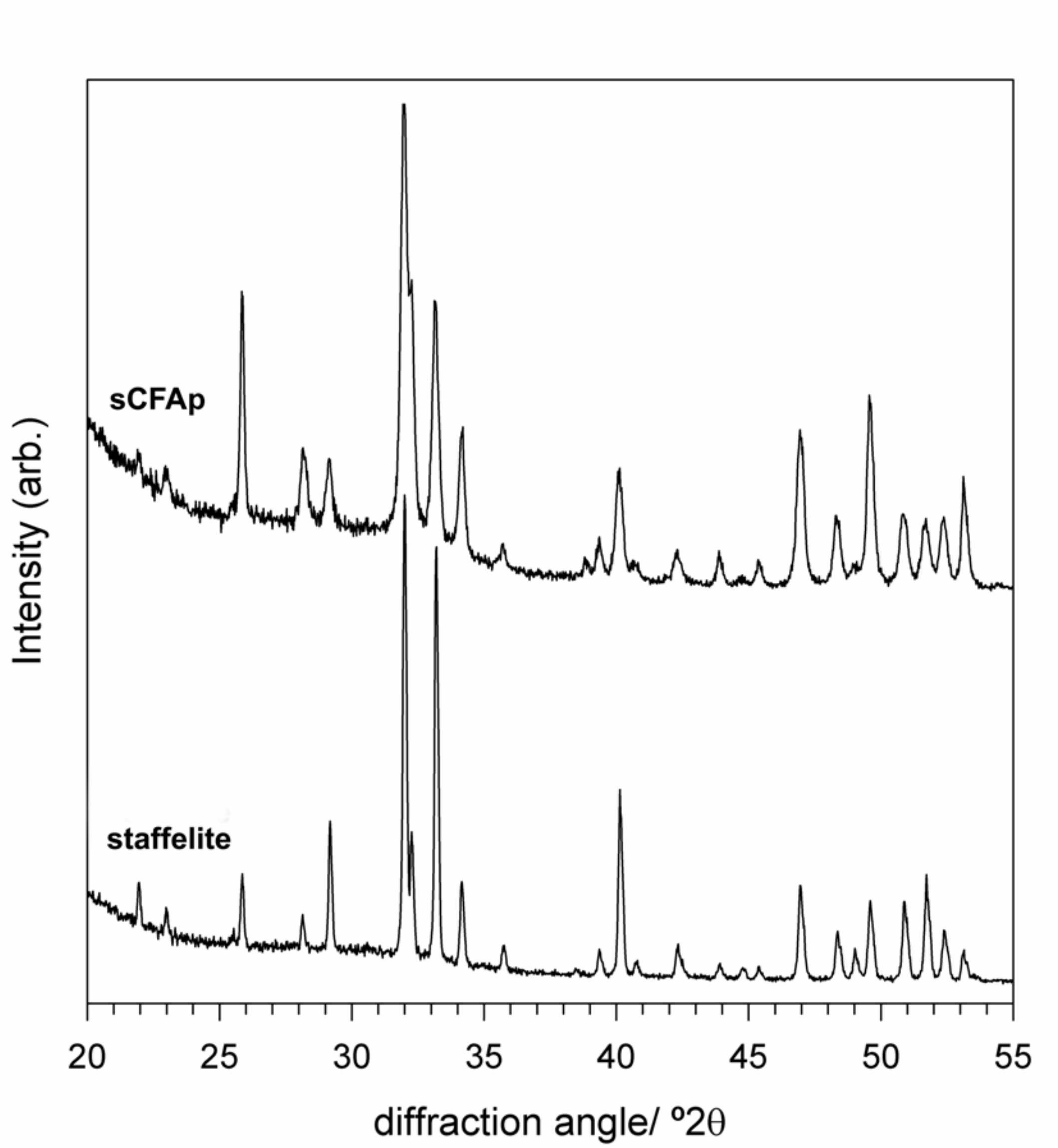

Figure 5.2. X-ray powder diffraction patterns for the synthetic sCFAp (top) and natural Staffelite (bottom) samples.

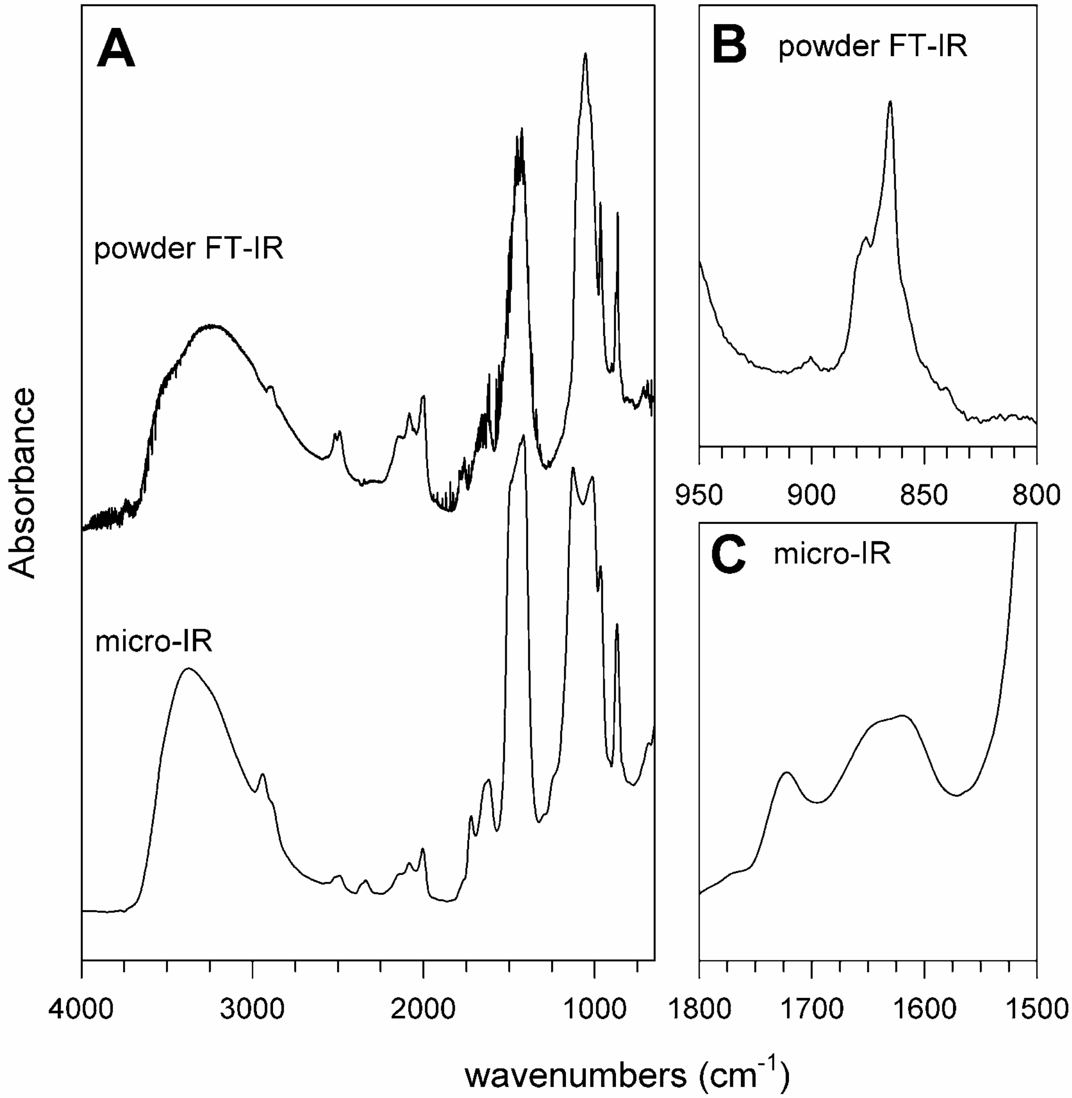

Figure 5.3. IR spectra of the natural Staffelite sample. **A.** Spectra obtained by (top) powder FT-IR and (bottom) Micro-FT-IR methods **B**. Expanded view of the CO_3 ν_3 region (powder) **C.** Expanded view of the molecular H_2O bending region (micro-FT-IR).

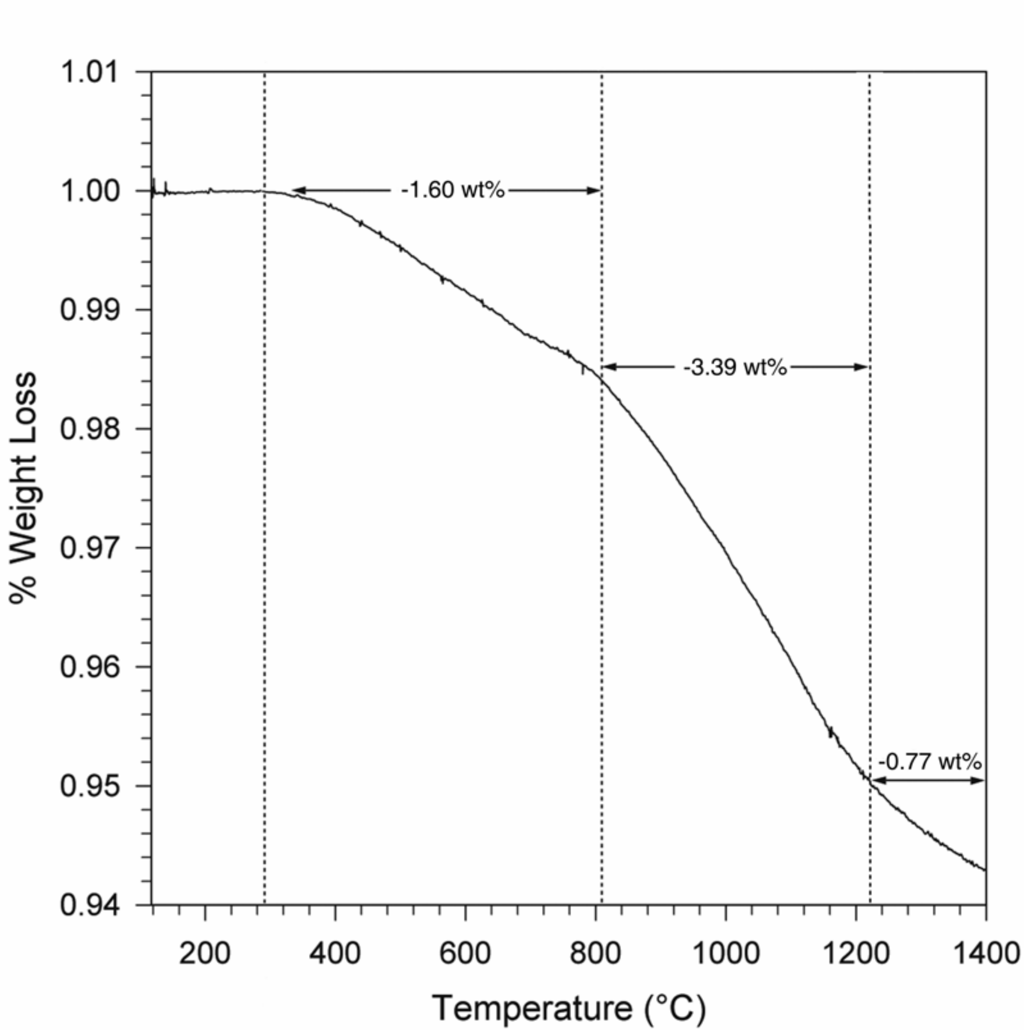

Figure 5.4. TG Curve for the staffelite sample collected at a heating rate of 20 °C/min over a range of 160 to 1400 °C. The three observed weight losses are marked at the onset with dashed lines and labeled with the corresponded weight percent loss.

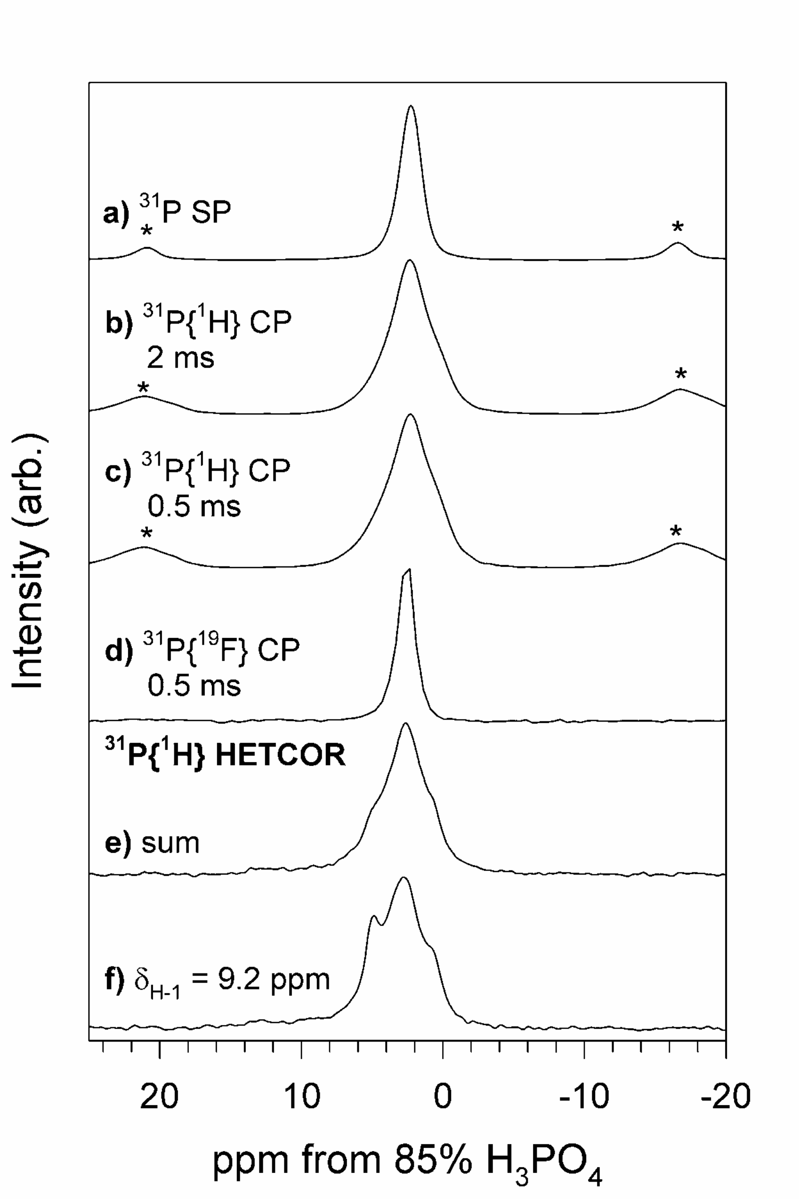

Figure 5.5. ^{31}P NMR spectra of the staffelite sample. **a)** ^{31}P SP/MAS at spinning rate of 3 kHz and a pulse delay of 120 s for 4 acquisitions; **b-c)** ^{31}P{^{1}H} CP/MAS at a spinning rate of 3 kHz and a pulse delay of 2 s for 1344 acquisitions with contact times of **b)** 2 ms and **c)** 0.5 ms; **d)** ^{31}P{^{19}F} CP/MAS NMR at a spinning rate of 13 kHz, pulse delay of 10 s, and a contact time of 0.5 ms for 64 acquisitions. **e-f)** ^{31}P{^{1}H} HetCor at a spinning rate of 10 kHz, contact time of 2 ms and a pulse delay of 2 s for a total of 168 acquisitions **e)** ^{31}P summed projection over the ^{1}H centerband. **f)** ^{31}P slice taken at $\delta_H = 9.2$ ppm.

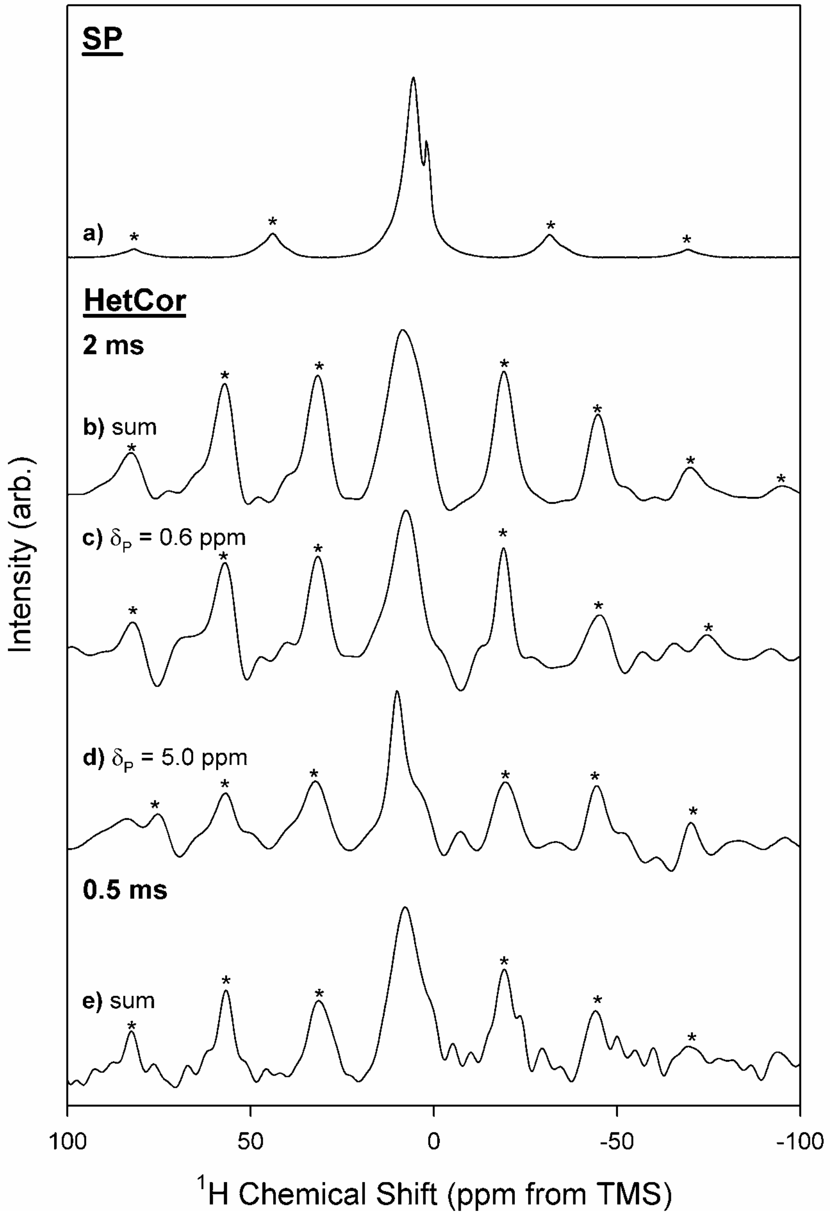

Figure 5.6. ^{1}H NMR spectra of the staffelite sample. **a)** ^{1}H SP/MAS,15 kHz spinning rate, pulse delay, 512 acquisitions; **b-e)** ^{31}P{^{1}H} HetCor indirectly detected ^{1}H spectra. **b)** Sum projection over the ^{31}P centerband, 2 ms contact time **c)** Slice from 2 ms spectrum taken at δ_P = 0.6 ppm **d)** Slice from 2 ms spectrum taken at δ_P = 5.0 ppm **e)** Sum projection over the ^{31}P centerband, 0.5 ms contact time. HetCor spectra were collected for a total of 64 hypercomplex increments in t1 at a spinning rate of 10 kHz and a pulse delay of 2 s.

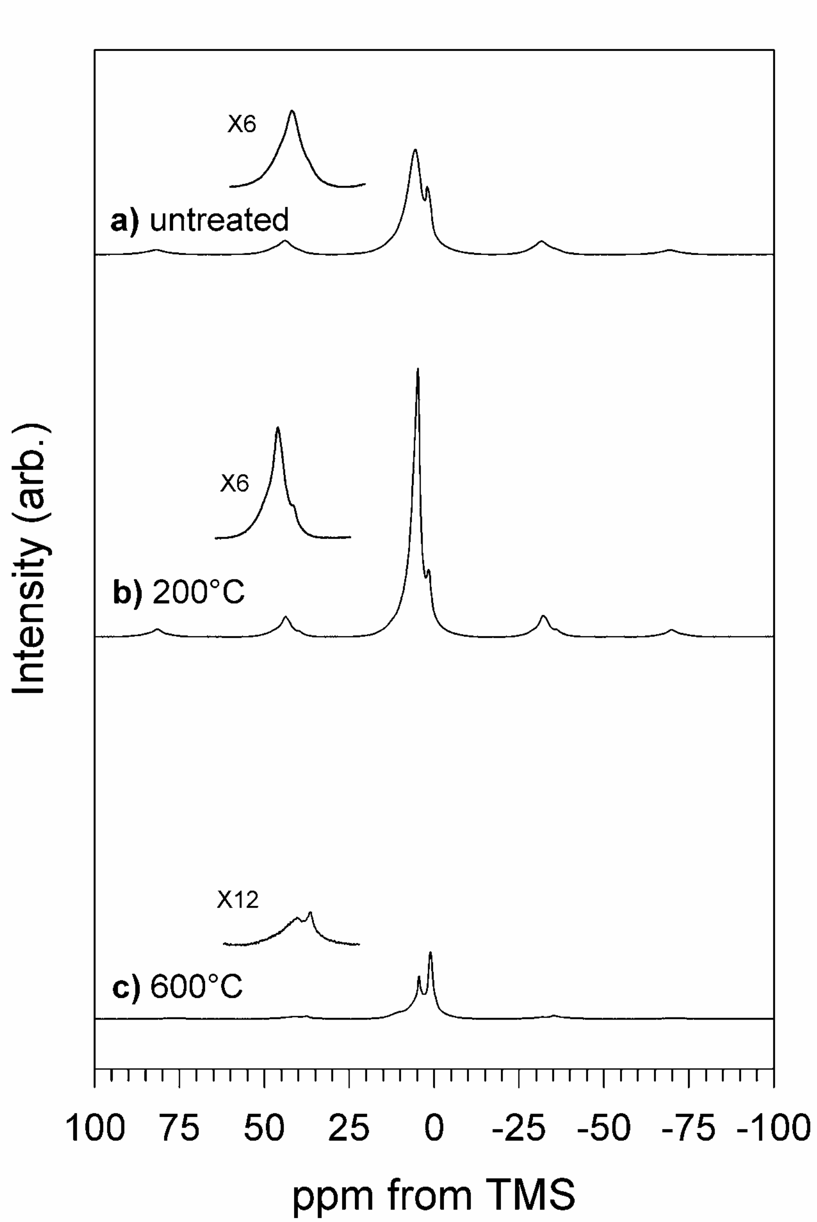

Figure 5.7. ^{1}H SP/MAS NMR spectra collected at a spinning rate of 15 kHz for staffelite **a)** no heat treatment, heat treated at **b)** 200 ºC and **c)** 600 ºC for ### and ### acquisitions, respectively. Insets are vertical expansion of the n = +1 sidebands. The spectra are scaled such that the hydroxyl peak at 1.6 ppm has the same area.

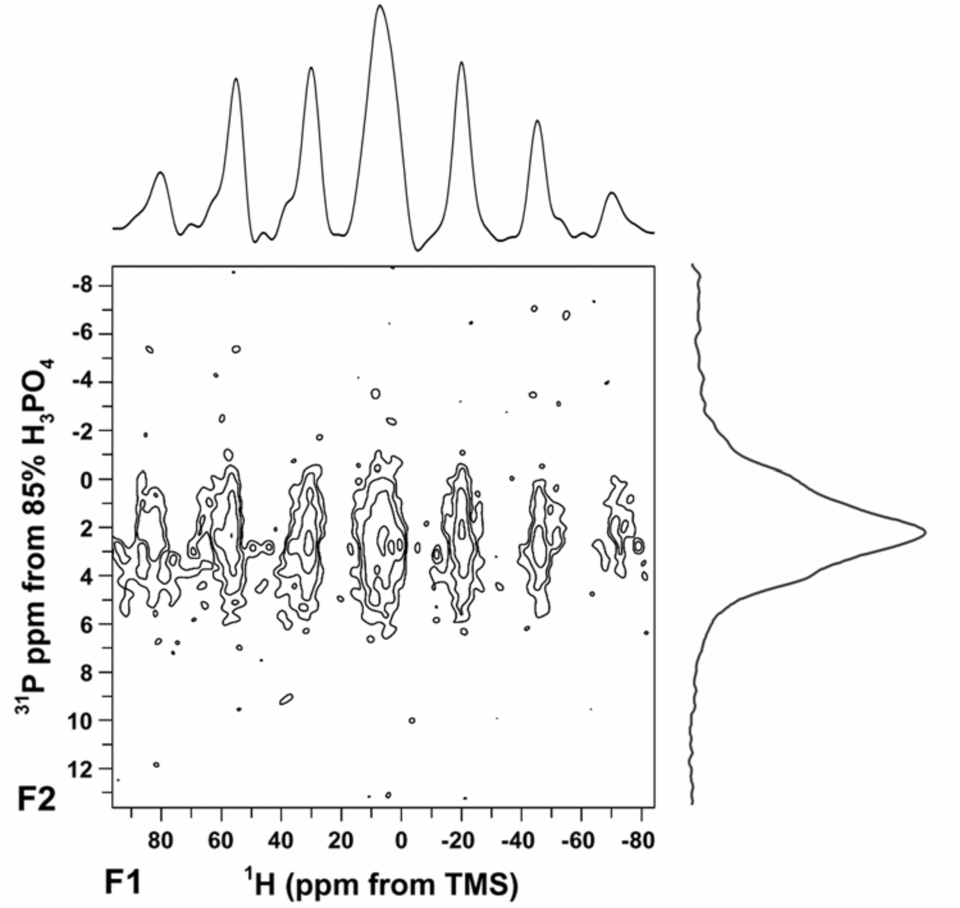

Figure 5.8. 2-dimentional ^{31}P{^{1}H} HetCor spectrum of Staffelite. Spectra acquired with 2 ms contact time, 1 s pulse delay, 10 kHz spinning rate, 168 acquisitions.

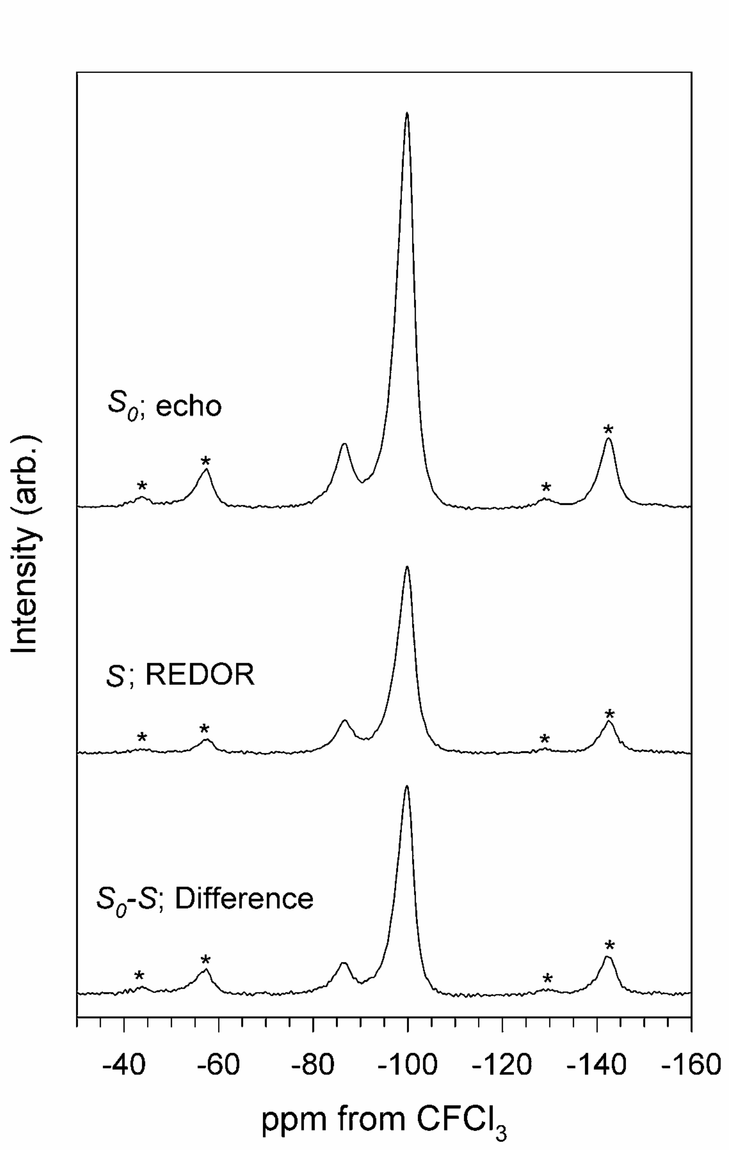

Figure 5.9. ^{19}F NMR spectra of the natural Staffelite and synthetic sCHFAp samples. **a)** ^{19}F SP/MAS NMR of Staffelite sample; 200 s pulse delay, 15 kHz spinning speed, 14 acquisitions. **b)** ^{19}F SP/MAS NMR of sCFAp sample; 20 s pulse delay, 13 kHz spinning speed, 16 acquisitions, ◆ indicates CaF_2 impurity peak. Asterisks denote spinning sidebands.

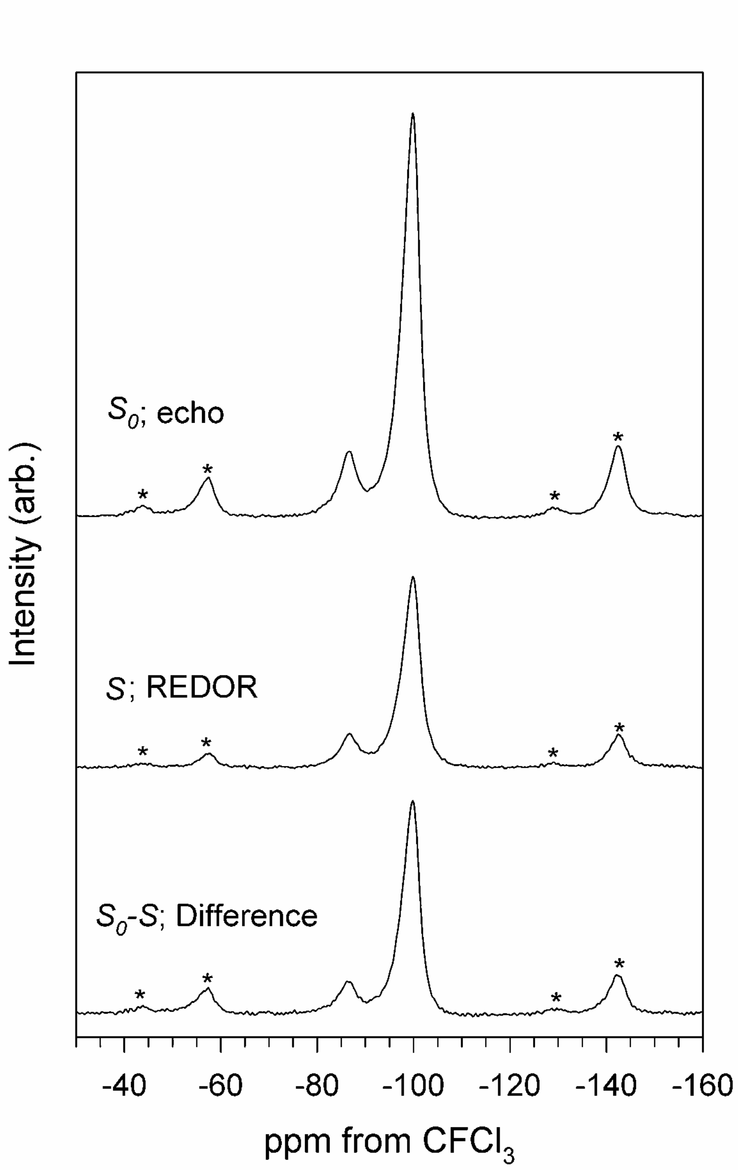

Figure 5.10. $^{19}F\{^{31}P\}$ REDOR spectra, set of the staffelite sample at 0.5 ms dephasing period using a spinning rate of 20 kHz and a pulse delay of 20 s. From top to bottom: ^{19}F Spin-echo control spectrum, S_0; $^{19}F\{^{31}P\}$ REDOR spectrum, S; difference Spectrum, S_0-S. Spectra are scaled by absolute intensities. Asterisks denote spinning sidebands.

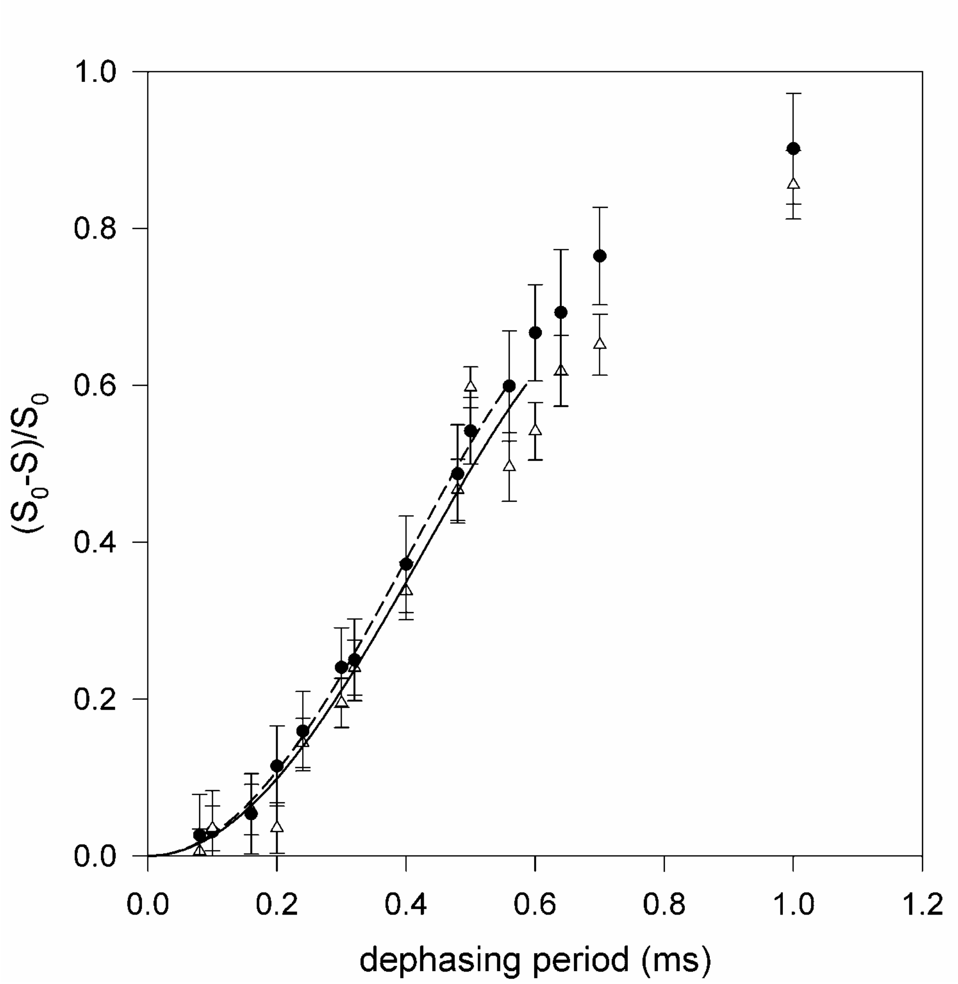

Figure 5.11. Variation of the REDOR fraction [$(S_0\text{-}S)/S_0$] with dephasing period for staffelite for peaks at -98.6 ppm (circles; top) and -86.6 ppm (triangles; bottom) collected at spinning rates of 20 kHz and 25 kHz. Dashed and solid lines represent least squares fits of the data using a three spin REDOR approximation assuming trigonal planer geometry for the -98.6 and -86.6 ppm peaks, respectively.

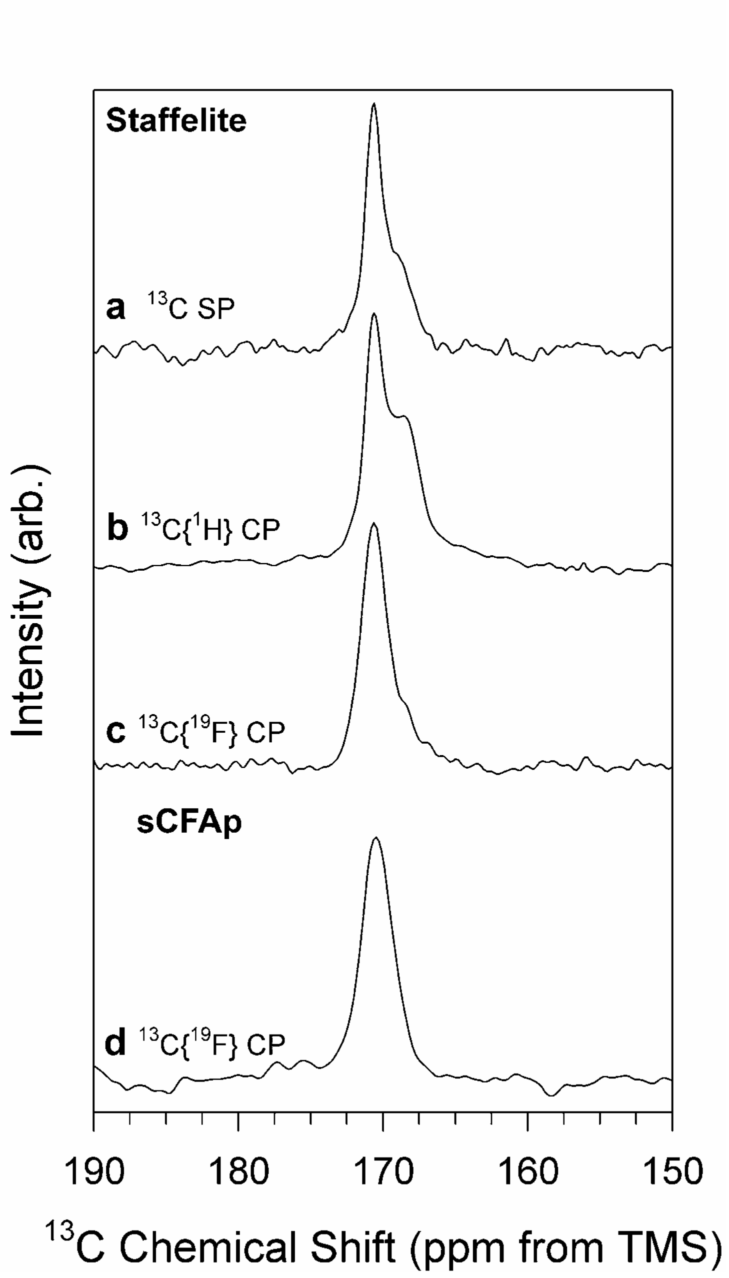

Figure 5.12. ^{13}C NMR spectra of staffelite (a-c) and synthetic sCFAp (d). **a)** ^{13}C SP/MAS; 120 s pulse delay; 543 acquisitions. **b.** ^{13}C{^{1}H} CP/MAS; 5 ms contact time, 2 s pulse delay, 84812 acquisitions. **c.** ^{13}C{^{19}F} CP/MAS; 12 ms contact time, 20 s pulse delay, 4142 acquisitions. **d.** ^{13}C{^{19}F} CP/MAS; 15 ms contact time, 20 s pulse delay, 32 acquisitions.

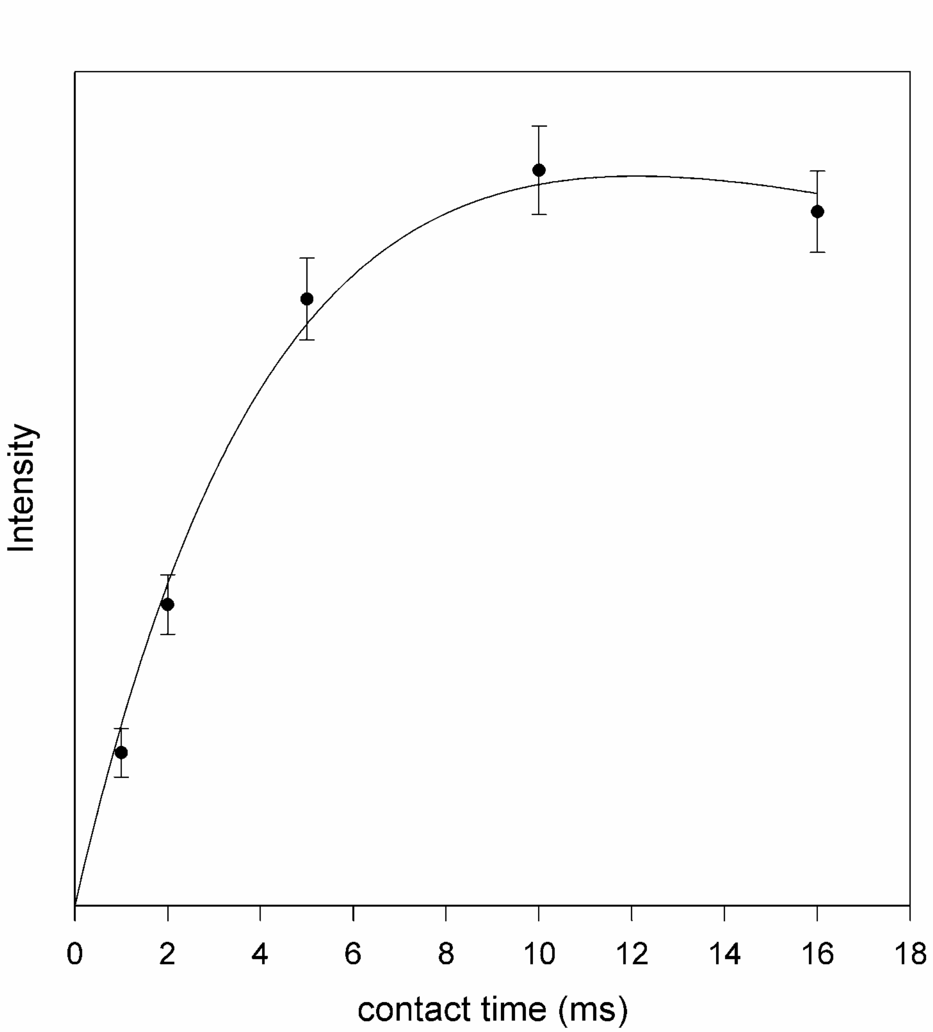

Figure 5.13. Variation in intensity of $^{13}C\{^{19}F\}$ CP/MAS spectra of staffelite with CP contact time. The solid line represents a least squares fit of the experimental data to classical CP kinetics.

VI. Implications

1. Introduction

In all the systems discussed in the previous chapters, H incorporation in concert with defect incorporation emerges as the common link. Double-resonance NMR spectroscopic experiments are demonstrated to be critical for investigating the link between H and defects. Chapters 2 and 3 focused on the coprecipitation of phosphate with calcium carbonate minerals. Chapters 4 and 5 investigated the incorporation of carbonate into apatite minerals. In each study, a range of double resonance NMR techniques were employed and identified H-bearing species associated with these defects. The H-bearing species would otherwise be difficult to identify using standard geochemical techniques. The following chapter explores this common thread among these systems, discusses briefly the difficulties in using standard geochemical methods for studying H speciation, and provides future directions in geosciences for the use of double-resonance solid-state nuclear magnetic resonance (NMR) spectroscopy.

2. H-bearing Species and Defect Identification

In each of the chapters, the primary defect species studied associated closely with H-bearing species. The major differences among the P-species identified in the phosphate/calcite (Chapter 2) and the phosphate/aragonite (Chapter 3) systems were the differences in associated H-species. In the carbonate apatites (Chapters 4 and 5) carbonate incorporation involved incorporation of differing H-bearing species. In all cases, a minor amount of H was involved in these substitutions, but the importance of these H species to the defect substitutions and to the geochemistry of these minerals is significant.

In Chapters 2 and 3 the identification of the P-species involved in the calcite/phosphate and aragonite/phosphate systems was assisted through the identification of corresponding H-species. In both cases, the majority P-species was phosphate incorporated into the carbonate structure with concomitant H-bearing defects. In the coral skeletal aragonite, the use of $^{31}P\{^{1}H\}$ HetCor methods identified structurally bound water and hydroxyls, but not aliphatic H-species. This data provides the critical geochemical insight that the source of phosphate is not organo-phosphates produced by the coral polyp. Instead, the phosphate must incorporate into the skeletal material through inorganic processes.

Both carbonate/phosphate systems also contained meaningful amounts of crystalline phosphate inclusions. Identification of these inclusions involved analyses of the associated H-species using $^{31}P\{^{1}H\}$ CP/MAS NMR. Some samples of speleothem calcite and coralline aragonite produce ^{31}P SP/MAS spectra containing a peak at or near 2.6 ppm. With this data alone, the conclusion that this peak arises from hydroxylapatite could be easily reached. However, when $^{31}P\{^{1}H\}$ CP/MAS spectra were collected this peak is absent in spectra collected of calcite samples, but only present in those collected for aragonite samples. Therefore, hydroxylapatite is present in the aragonite, but not in the calcite samples. Also, in the calcite samples additional peaks arising from the hydrous calcium phosphate phase monetite are also present. While these two systems both incorporate phosphate as defects, the difference in crystalline phases present indicates there are key differences in the phosphate incorporation mechanisms possibly linked to the differing roles of H.

H-bearing species also contribute substantially to the carbonate hydroxylapatite (CHAp) and carbonate fluorapatite (CFAp) systems studied in Chapters 4 and 5, respectively. Again examination of SP/MAS spectra proves inadequate in completely identifying not only the carbonate species targeted, but also their associate H-species. ^{13}C SP/MAS NMR spectra of CHAp samples indicate only that A and B-type carbonate substitutions are present but little else can be divined. The $^{13}C\{^{1}H\}$ CP/MAS kinetics do indicate differential association with H-species in these samples, but are insufficient to identify the ^{1}H. $^{13}C\{^{1}H\}$ HetCor spectra correctly identify peaks near $\delta_H = 1$ to 0 ppm from hydroxyl groups, and a peak at $\delta_H = 5.5$ ppm. The chemical shift of this peak at $\delta_H = 5.5$ ppm indicate weak to moderate hydrogen bonding, but the CP kinetics indicate strong coupling to ^{13}C. Therefore, isolated hydrogen carbonate groups in these samples were concluded to be the source of this peak. Not only does the presence of hydrogen carbonate allow for charge and structure balance of the carbonate substitutions, but they could significantly affect the reactivity and solubility of these materials.

H plays a similar role balancing carbonate incorporation in CFAp, but involves alternate H-species than are present in CHAp. No hydrogen carbonate species and little hydroxyl in the channels were observed in the CFAp samples. Instead, the main H-species identified in ^{1}H SP/MAS NMR spectra is structural water. The results from $^{31}P\{^{1}H\}$ HetCor indicate that this structural water is a constituent of the CHAp and not derived from an inclusion. Since this species does not carry charge, it can only serve a structural role in this system. It was postulated that due to the inability to observed the A-type carbonate peak in $^{13}C\{^{19}F\}$ CP/MAS spectra that the structural water serves to isolate the carbonate in the channels from F by incorporating above and below the defect. This incorporation method is similar to the proposed incorporation of A-type hydrogen carbonate in CHAp where the H-species relieves stresses on the channel organization induced by carbonate incorporation.

In all these systems, double resonance NMR techniques provided insight into the H-speciation that is unobtainable using other analytical techniques. X-ray powder diffraction (XRD) cannot be used to speciate H in these samples due to the low scattering profile of ^{1}H. Vibrational (Infrared (IR) and Raman) spectroscopies are sensitive to H-bending and stretching modes, and can be used successfully to speciate H. However, in the carbonate/phosphate systems, the P-bearing defects with which the H-bearing species are associated are present at 70 – 200 ppm level concentrations making vibrations due to H-species hard to ascertain from those of the carbonate mineral. The difficulty with vibrational spectra is the same for the carbonate apatites, where multiple H-species are present in addition to modes from phosphate groups which can easily obscure the vibrations of bicarbonate in CHAp. In the CFAp, the issue is the inability to confirm associations of H-species to other defect species such as carbonate or F. The ability to both speciate H and to obtain information about defect association comes from the double-resonance NMR experiments.

3. Future Directions

While the above studies show the advantage of double resonance NMR spectroscopy, other systems where H plays an important role could benefit from the use of these experiments. One of the largest potential areas of growth for NMR application is in the field of biomineralization. The processes that organisms use to form their hard mineral parts involve the formation and transformation of intermediate minerals to get the final mineral part. Organisms often mediate the precipitation and transformation of minerals by careful control of the amount of H present in the system.

The formation of hydroxylapatite (HAp) in bones and teeth is thought to begin with an amorphous calcium phosphate (ACP) precursor which transforms through octacalcium phosphate (OCP) to HAp. In these steps, the phase goes from the hydrated phase ACP to the more dehydrated HAp end product. The relative stability of the transforming phases is likely linked to H-bearing species present. It is also possible that additional metastable or stable calcium phosphate minerals may also form. Numerous NMR studies have been preformed on the intermediate products and the end product HAp [1-4], but were largely focused on gross characterization of the phases. Double resonance experiments could be used to follow the transformation of the starting material ACP to elucidate the mechanisms of transformation. $^{31}P\{^{1}H\}$ HetCor spectra of transforming ACP could track the protonation state of phosphate, and potentially detect the formation of minor amounts of adjunct minerals.

Biomineralization is only one of many fields where the solid-state NMR spectroscopic methods used in this dissertation can be applied. Problems with water transport in nominally anhydrous minerals to the deep mantle may be tackled with use CP/MAS or HetCor techniques. REDOR methods could be employed to tackle Al/Si disorder in aluminosilicates. Also with new and better access to higher field magnets (21.1 T and above) the potential to test models of trace metal incorporation into calcium carbonate with ^{25}Mg [5], ^{43}Ca [6], and even ^{87}Sr [7] double resonance experiments may soon be possible. These are only a few examples of areas in which NMR can expand within the realm of geosciences.

4. References

[1] C. Jager, T. Welzel, W. Meyer-Zaika, M. Epple, A solid-state NMR investigation of the structure of nanocrystalline hydroxyapatite, Magn. Reson. Chem. 44(2006) 573-580.

[2] Y.H. Tseng, J.H. Zhan, K.S.K. Lin, C.Y. Mou, J.C.C. Chan, High resolution ^{31}P NMR study of octacalcium phosphate, Solid State Nucl. Magn. Reson. 26(2004) 99-104.

[3] W.P. Aue, A.H. Roufosse, M.J. Glimcher, R.G. Griffin, Solid-State ^{31}P Nuclear Magnetic-Resonance Studies of Synthetic Solid-Phases of Calcium-Phosphate - Potential Models of Bone-Mineral, Biochemistry 23(1984) 6110-6114.

[4] W.P. Rothwell, J.S. Waugh, J.P. Yesinowski, High-Resolution Variable-Temperature ^{31}P NMR of Solid Calcium Phosphates, J. Am. Chem. Soc. 102(1980) 2637-2643.

[5] P.J. Sideris, U.G. Nielsen, Z.H. Gan, C.P. Grey, Mg/Al ordering in layered double hydroxides revealed by multinuclear NMR spectroscopy, Science 321(2008) 113-117.

[6] R. Dupree, A.P. Howes, S.C. Kohn, Natural abundance solid state Ca-43 NMR, Chem. Phys. Lett. 276(1997) 399-404.

[7] G.M. Bowers, R. Ravella, S. Komarneni, K.T. Mueller, NMR study of strontium binding by a micaceous mineral, Journal of Physical Chemistry B 110(2006) 7159-7164.

Bibliography

[1] A.M. Abed, K. Fakhouri, On the chemical variability of phosphatic particles from Jordanian phosphorite deposits, Chemical Geology 131(1996) 1-13.

[2] J.P. Amoureux, C. Fernandez, Triple, quintuple and higher order multiple quantum MAS NMR of quadrupolar nuclei, Solid State Nuclear Magnetic Resonance 10(1998) 211-223.

[3] E. Anagnostou, R.M. Sherrell, J.F. Adkins, A.C. Gagnon, Phosphorus, barium and boron in the deep-sea coral Desmophyllum dianthus: Preliminary calibrations, Geochim. Cosmochim. Acta 71(2007) A22.

[4] A. Antonakos, E. Liarokapis, T. Leventouri, Micro-Raman and FTIR studies of synthetic and natural apatites, Biomaterials 28(2007) 3043-3054.

[5] R. Astala, M.J. Stott, First principles investigation of mineral component of bone: CO_3 substitutions in hydroxyapatite, Chemistry of Materials 17(2005) 4125-4133.

[6] W.P. Aue, A.H. Roufosse, M.J. Glimcher, R.G. Griffin, Solid-State ^{31}P nuclear magnetic resonance studies of synthetic solid phases of calcium phosphate: Potential models of bone mineral, Biochemistry 23(1984) 6110-6114.

[7] M. Bak, J.T. Rasmussen, N.C. Nielsen, SIMPSON: A general simulation program for solid-state NMR spectroscopy, Journal of Magnetic Resonance 147(2000) 296-330.

[8] A. Baker, P.L. Smart, R.L. Edwards, D.A. Richards, Annual growth banding in a cave stalagmite, Nature 364(1993) 518-520.

[9] J.U.L. Baldini, F. McDermott, I.J. Fairchild, Structure of the 8200-year cold event revealed by a speleothem trace element record, Science 296(2002) 2203-2206.

[10] J. Barralet, S. Best, W. Bonfield, Carbonate substitution in precipitated hydroxyapatite: An investigation into the effects of reaction temperature and bicarbonate ion concentration, Journal of Biomedical Materials Research 41(1998) 79-86.

[11] M. Bertmer, H. Eckert, Dephasing of spin echoes by multiple heteronuclear dipolar interactions in rotational echo double resonance NMR experiments, Solid State Nuclear Magnetic Resonance 15(1999) 139-152.

[12] K. Beshah, C. Rey, M.J. Glimcher, M. Schimizu, R.G. Griffin, Solid-State ^{13}C and Proton NMR-Studies of Carbonate-Containing Calcium Phosphates and Enamel, Journal of Solid State Chemistry 84(1990) 71-81.

[13] P.S. Belton, R.K. Harris, P.J. Wilkes, Solid-state ^{31}P NMR studies of synthetic inorganic calcium phosphates, J. Phys. Chem. Solids 49(1988) 21-27.

[14] G. Binder, G. Troll, Coupled Anion Substitution in Natural Carbon-Bearing Apatites, Contributions to Mineralogy and Petrology 101(1989) 394-401.

[15] M. Bohner, J. Lemaitre, A.P. Legrand, J.B.D. delaCaillerie, P. Belgrand, Synthesis, X-ray diffraction and solid-state ^{31}P magic angle spinning NMR study of alpha-tricalcium orthophosphate, J. Mater. Sci.: Mater. Med. 7(1996) 457-463.

[16] G.M. Bowers, R. Ravella, S. Komarneni, K.T. Mueller, NMR study of strontium binding by a micaceous mineral, Journal of Physical Chemistry B 110(2006) 7159-7164.

[17] M. Braun, P. Hartmann, C. Jana, ^{19}F and ^{31}P NMR Spectroscopy of Calcium Apatites, Journal of Materials Science-Materials in Medicine 6(1995) 150-154.

[18] G.P. Brophy, J.T. Nash, Compositional Infrared and X-Ray Analysis of Fossil Bone, American Mineralogist 53(1968) 445-&.

[19] B. Bureau, G. Silly, J.Y. Buzare, J. Emery, Superposition model for F-19 isotropic chemical shift in ionic fluorides: from basic metal fluorides to transition metal fluoride glasses, Chemical Physics 249(1999) 89-104.

[20] E.A. Burton, L.M. Walter, The role of pH in phosphate inhibition of calcite and aragonite precipitation rates in seawater, Geochim. Cosmochim. Acta 54(1990) 797-808.

[21] B.J. Cade-Menun, Characterizing phosphorus in environmental and agricultural samples by ^{31}P nuclear magnetic resonance spectroscopy, Talanta 66(2005) 359-371.

[22] A.L. Cohen, T.A. McConnaughey, Geochemical perspectives on coral mineralization, Biomineralization 54(2003) 151-187.

[23] D. Coster, A.L. Blumenfeld, J.J. Fripiat, Lewis-Acid Sites and Surface Aluminum in Aluminas and Zeolites - a High-Resolution Nmr-Study, Journal of Physical Chemistry 98(1994) 6201-6211.

[24] V.G.R. Chada, D.B. Hausner, D.R. Strongin, A.A. Rouff, R.J. Reeder, Divalent Cd and Pb uptake on calcite $\{10\bar{1}4\}$ cleavage faces: An XPS and AFM study, J. Colloid Interface Sci. 288(2005) 350-360.

[25] G.Y. Cho, Y.T. Wu, J.L. Ackerman, Detection of hydroxyl ions in bone mineral by solid-state NMR spectroscopy, Science 300(2003) 1123-1127.

[26] L.L. Clark, E.D. Ingall, R. Benner, Marine phosphorus is selectively remineralized, Nature 393(1998) 426-426.

[27] J.L. Conca, J. Wright, An Apatite II permeable reactive barrier to remediate groundwater containing Zn, Pb and Cd, Applied Geochemistry 21(2006) 1288-1300.

[28] E. Curti, Coprecipitation of radionuclides with calcite: estimation of partition coefficients based on a review of laboratory investigations and geochemical data, Appl.Geochem. 14(1999) 433-445.

[29] J. deKanel, J.W. Morse, Chemistry of orthohosphate uptake from seawater onto calcite and aragonite, Geochim. Cosmochim. Acta 42(1978) 1335-1340.

[30] J.M. Desmarchelier, J.C. Hellstrom, M.T. McCulloch, Rapid trace element analysis of speleothems by ELA-ICP-MS, Chem. Geol. 231(2006) 102-117.

[31] P.M. Dove, M.F. Hochella, Calcite precipitation mechanisms and inhibition by orthophosphate: In situ observations by scanning force microscopy, Geochim. Cosmochim. Acta 57(1993) 705-714.

[32] R. Dupree, A.P. Howes, S.C. Kohn, Natural abundance solid state Ca-43 NMR, Chem. Phys. Lett. 276(1997) 399-404.

[33] W.L. Earl, D.L. Vanderhart, Measurement of C-13 Chemical-Shifts in Solids, Journal of Magnetic Resonance 48(1982) 35-54.

[34] J.C. Elliott, Calcium Phosphate Biominerals, Rev. Mineral. Geochem. 48(2002) 427-453.

[35] I.J. Fairchild, A. Baker, A. Borsato, S. Frisia, R.W. Hinton, F. McDermott, A.F. Tooth, Annual to sub-annual resolution of multiple trace-element trends in speleothems, J. Geol. Soc. London 158(2001) 831-841.

[36] I.J. Fairchild, C.L. Smith, A. Baker, L. Fuller, C. Spotl, D. Mattey, F. McDermott, E.I.M.F., Modification and preservation of environmental signals in speleothems, Earth Sci. Rev. 75(2006) 105-153.

[37] J. Feng, Y. Lee, J.D. Kubicki, R.J. Reeder, B.L. Phillips, NMR Spectroscopy of Citrate in Solids: Cross-Polarization Kinetics in Weakly Coupled Systems, Magnetic Resonance in Chemistry Submitted(2007).

[38] J. Feng, Y. Lee, R.J. Reeder, B.L. Phillips, Observation of bicarbonate in calcite by NMR spectroscopy, Am. Mineral. 91(2006) 957-960.

[39] A.A. Finch, P.A. Shaw, G.P. Weedon, K. Holmgren, Trace element variation in speleothem aragonite: potential for palaeoenvironmental reconstruction, Earth Planet. Sci. Lett. 186(2001) 255-267.

[40] M.E. Fleet, X.Y. Liu, Carbonate apatite type A synthesized at high pressure: new space group (P(3)over-bar) and orientation of channel carbonate ion, Journal of Solid State Chemistry 174(2003) 412-417.

[41] M.E. Fleet, X.Y. Liu, Location of type B carbonate ion in type A-B carbonate apatite synthesized at high pressure, Journal of Solid State Chemistry 177(2004) 3174-3182.

[42] M.E. Fleet, X. Liu, Coupled substitution of type A and B carbonate in sodium-bearing apatite, Biomaterials 28(2007) 916-926.

[43] M.E. Fleet, X. Liu, Hydrogen-carbonate ion in synthetic high-pressure apatite, American Mineralogist 92(2007) 1764-1767.

[44] M.E. Fleet, X. Liu, Accommodation of the carbonate ion in fluorapatite synthesized at high pressure, American Mineralogist 93(2008) 1460-1469.

[45] M.E. Fleet, X.Y. Liu, P.L. King, Accommodation of the carbonate ion in apatite: An FTIR and X-ray structure study of crystals synthesized at 2-4 GPa, American Mineralogist 89(2004) 1422-1432.

[46] M.E. Fleet, Y.M. Pan, Site preference of rare earth elements in fluorapatite: Binary (LREE+HREE)-substituted crystals, American Mineralogist 82(1997) 870-877.

[47] S. Frisia, A. Borsato, I.J. Fairchild, F. McDermott, Calcite fabrics, growth mechanisms, and environments of formation in speleothems from the Italian Alps and southwestern Ireland, J. Sediment. Res. 70(2000) 1183-1196.

[48] S. Frisia, A. Borsato, I.J. Fairchild, F. McDermott, E.M. Selmo, Aragonite-calcite relationships in speleothems (Grotte de Clamouse, France): Environment, fabrics, and carbonate geochemistry, J. Sediment. Res. 72(2002) 687-699.

[49] S. Frisia, A. Borsato, I.J. Fairchild, J. Susini, Variations in atmospheric sulphate recorded in stalagmites by synchrotron micro-XU and XANES analyses, Earth Planet. Sci. Lett. 235(2005) 729-740.

[50] S. Frisia, A. Borsato, N. Preto, F. McDermott, Late Holocene annual growth in three Alpine stalagmites records the influence of solar activity and the North Atlantic Oscillation on winter climate, Earth Planet. Sci. Lett. 216(2003) 411-424.

[51] L. Frydman, J.S. Harwood, Isotropic Spectra of Half-Integer Quadrupolar Spins from Bidimensional Magic-Angle-Spinning Nmr, Journal of the American Chemical Society 117(1995) 5367-5368.

[52] G.A. Gaetani, A.L. Cohen, Element partitioning during precipitation of aragonite from seawater: A framework for understanding paleoproxies (vol 70, pg 4617, 2006), Geochim. Cosmochim. Acta 71(2007) 530-530.

[53] S.J. Gaffey, H_2O and OH in echinoid calcite: A spectroscopic study, Am. Mineral. 80(1995) 947-959.

[54] A.C. Gagnon, J.F. Adkins, D.P. Fernandez, L.F. Robinson, Sr/Ca and Mg/Ca vital effects correlated with skeletal architecture in a scleractinian deep-sea coral and the role of Rayleigh fractionation, Earth Planet. Sc. Lett. 261(2007) 280-295.

[55] M.J. Genge, A.P. Jones, G.D. Price, An Infrared and Raman-Study of Carbonate Glasses - Implications for the Structure of Carbonatite Magmas, Geochimica Et Cosmochimica Acta 59(1995) 927-937.

[56] C.R. Glenn, K.B. Follmi, S.R. Riggs, G.N. Baturin, K.A. Grimm, J. Trappe, A.M. Abed, C. Galli-Oliver, R.E. Garrison, A.V. Ilyin, C. Jehl, V. Rohrlich, R.M.Y. Sadaqah, M. Schidlowski, R.E. Sheldon, H. Siegmund, Phosphorus and phosphorites: Sedimentology and environments of formation, Ecologae Geologicae Helvetiae 87(1994) 747-788.

[57] R.A. Griffin, J.J. Jurinak, Interaction of phosphate with calcite, Soil Sci. Soc. Am. J. 37(1973) 847-850.

[58] P.O. Hall, R.C. Aller, Rapid, small-volume, flow injection analysis for ΣCO_2 and NH^{4+} in marine and fresh waters, Limnol. Oceanogr. 37(1992) 1113-1119.

[59] J. Herzfeld, A.E. Berger, Sideband Intensities in NMR-Spectra of Samples Spinning at the Magic Angle, Journal of Chemical Physics 73(1980) 6021-6030.

[60] Z.R. Hinedi, S. Goldberg, A.C. Chang, J.P. Yesinowski, A ^{31}P and ^{1}H MAS NMR study of phosphate sorption onto calcium carbonate, J. Colloid Interface Sci. 152(1992) 141-160.

[61] T.J.B. Holland, S.A.T. Redfern, Unit cell refinement from powder diffraction data: The use of regression diagnostics, Mineralogical Magazine 61(1997) 65-77.

[62] W.A. House, Inhibition of calcite crystal growth by inorganic phosphate, J. Colloid Interface Sci. 119(1987) 505-511.

[63] W.A. House, L. Donaldson, Adsorption and coprecipitation of phosphate on calcite, J. Colloid Interface Sci. 112(1986) 309-324.

[64] H.M. Huang, I.J. Fairchild, A. Borsato, S. Frisia, N.J. Cassidy, F. McDermott, C.J. Hawkesworth, Seasonal variations in Sr, Mg and P in modern speleothems (Grotta di Ernesto, Italy), Chem. Geol. 175(2001) 429-448.

[65] S. Hunger, H. Cho, J.T. Sims, D.L. Sparks, Direct speciation of phosphorus in alum-amended poultry litter: Solid-State ^{31}P NMR investigation, Environ. Sci. Technol. 38(2004) 674-681.

[66] C. Jager, T. Welzel, W. Meyer-Zaika, M. Epple, A solid-state NMR investigation of the structure of nanocrystalline hydroxyapatite, Magnetic Resonance in Chemistry 44(2006) 573-580.

[67] S.J. Joris, C.H. Amberg, Nature of Deficiency in Nonstoichiometric Hydroxyapatites .2. Spectroscopic Studies of Calcium and Strontium Hydroxyapatites, Journal of Physical Chemistry 75(1971) 3172-&.

[68] A. Kaflak, D. Chmielewski, A. Gorecki, A. Slorarczyk, W. Kolodziejski, Efficiency of $^{1}H \rightarrow ^{31}P$ cross-polarization in bone apatite and its mineral standards, Solid State Nucl. Magn. Reson. 29(2006) 345-348.

[69] A.T. Kan, G.M. Fu, M.B. Tomson, Adsorption and precipitation of an aminoalkylphosphonate onto calcite, J. Colliod Interf. Sci. 281(2005) 275-284.

[70] D. Kim, J.D. Schuffert, M. Kastner, Francolite authigenesis in California continental slope sediments and its implications for the marine P cycle, Geochim. Cosmochim. Acta 63(1999) 3477-3485.

[71] W. Kolodziejski, J. Klinowski, Kinetics of cross-polarization in solid-state NMR: A guide for chemists, Chem. Rev. 102(2002) 613-628.

[72] L.C. Kolowith, R.A. Berner, Weathering of phosphorus in black shales, Global Biogeochemical Cycles 16(2002).

[73] P.G. Koutsoukos, G.H. Nancollas, Crystal-Growth of Calcium Phosphates - Epitaxial Considerations, J. Cryst. Growth 53(1981) 10-19.

[74] A. Krajewski, M. Mazzocchi, P.L. Buldini, A. Ravaglioli, A. Tinti, P. Taddei, C. Fagnano, Synthesis of carbonated hydroxyapatites: efficiency of the substitution and critical evaluation of analytical methods, Journal of Molecular Structure 744(2005) 221-228.

[75] A. Kuczumow, D. Genty, P. Chevallier, J. Nowak, M. Florek, A. Buczynska, X-ray and electron microprobe investigation of the speleothems from Godarville tunnel, X-Ray Spectrom. 34(2005) 502-508.

[76] M. LaVinge, M.P. Field, E. Anagnostou, A.G. Grottoli, G.M. Wellington, R.M. Sherrell, Skeletal P/Ca tracks upwelling in Gulf of Panama coral: Evidence for a new seawater phosphate proxy, Geophys. Res. Lett. 35(2008) L05604.

[77] L. Li, R. Stanforth, Distinguishing adsorption and surface precipitation of phosphate on goethite (α-FeOOH), J. Colloid Interface Sci. 230(2000) 12-21.

[78] E. Libowitzky, Correlation of O-H stretching frequencies and O-H•••O hydrogen bond lengths in minerals, Monatshefte Fur Chemie 130(1999) 1047-1059.

[79] F. Lippmann, Sedimentary carbonate minerals, Springer-Verlag, Berlin, New York,, 1973, vi, 228 p. pp.

[80] R. Lookman, H. Geerts, P. Grobet, R. Merckx, K. Vlassak, Phosphate speciation in excessively fertilized soil: A ^{31}P and ^{27}Al MAS NMR spectroscopy study, Eur. J. Soil Sci. 47(1996) 125-130.

[81] C.W. Mandeville, J.D. Webster, M.J. Rutherford, B.E. Taylor, A. Timbal, K. Faure, Determination of molar absorptivities for infrared absorption bands of H2O in andesitic glasses, American Mineralogist 87(2002) 813-821.

[82] H.E. Mason, A. Kozlowski, B.L. Phillips, Solid-State NMR Study of the Role of H and Na in AB-type Carbonate Apatite, Chemistry of Materials 20(2008) 294-302.

[83] H.E. Mason, S. Frisia, Y. Tang, R.J. Reeder, B.L. Phillips, Phosphorus speciation in calcite speleothems determined from solid-state NMR spectroscopy, Earth Planet. Sc. Lett. 254(2007) 313-322.

[84] J.M. McArthur, Francolite Geochemistry - Compositional Controls during Formation, Diagenesis, Metamorphism and Weathering, Geochimica Et Cosmochimica Acta 49(1985) 23-35.

[85] G.H. McClellan, J.R. Lehr, Crystal Chemical Investigation of Natural Apatites, American Mineralogist 54(1969) 1374-&.

[86] D. McConnell, A structural investigation of the isomorphism of the apatite group, American Mineralogist 23(1938) 1-19.

[87] F.M. McCubbin, H.E. Mason, H. Park, B.L. Phillips, J.B. Parise, H. Nekvasil, D.H. Lindsley, Synthesis and Characterization of low-OH- fluor-chlorapatite: A single-crystal XRD and NMR spectroscopic study, American Mineralogist 93(2008) 210-216.

[88] F.M. McCubbin, H. Nekvasil, B.L. Jolliff, P.K. Carpenter, R.A. Zeigler, D.H. Lindsley, Apatite from Apollo samples 14161 and 12033: Analytical hurdles and

implications for relative fluorine and chlorine contents in late-stage lunar magmas and melts., Proceedings of the NLSI Lunar Science Conference, Moffett Field, California. Abstract #2127(2008).

[89] F. McDermott, S. Frisia, Y.M. Huang, A. Longinelli, B. Spiro, T.H.E. Heaton, C.J. Hawkesworth, A. Borsato, E. Keppens, I.J. Fairchild, K. van der Borg, S. Verheyden, E. Selmo, Holocene climate variability in Europe: Evidence from $\delta^{18}O$, textural and extension-rate variations in three speleothems, Quat. Sci. Rev. 18(1999) 1021-1038.

[90] F. McDermott, H.P. Schwarcz, P.J. Rowe, Isotopes in speleothems. In: Isotopes in Palaeoenvironmental Research, Springer, Dordrecht, The Netherlands, 2005 (in press).

[91] E.A. McMillan, Tests for paleoaridity in Holocene Stalagmites from SW Europe. Ph.D. Thesis (unpublished), Keele University, U.K., (2006).

[92] E.A. McMillan, I.J. Fairchild, S. Frisia, A. Borsato, F. McDermott, Annual trace element cycles in calcite-aragonite speleothems: Evidence of drought in the western Mediterranean 1200-1100 yr BP, J. Quat. Sci. 20(2005) 423-433.

[93] H.J. Meyer, The influence of impurities on the growth rate of calcite, J. Cryst. Growth 66(1984) 639-646.

[94] F. Millero, F. Huang, X.R. Zhu, X.W. Liu, J.Z. Zhang, Adsorption and desorption of phosphate on calcite and aragonite in seawater, Aquat. Geochem. 7(2001) 33-56.

[95] P. Montagna, M. McCulloch, M. Taviani, C. Mazzoli, B. Vendrell, Phosphorus in cold-water corals as a proxy for seawater nutrient chemistry, Science 312(2006) 1788-1791.

[96] L.B. Moran, J.K. Berkowitz, J.P. Yesinowski, F-19 and P-31 Magic-Angle Spinning Nuclear-Magnetic-Resonance of Antimony(Iii)-Doped Fluorapatite Phosphors - Dopant Sites and Spin Diffusion, Physical Review B 45(1992) 5347-5360.

[97] A. Mucci, Growth kinetics and composition of magnesian calcite overgrowths precipitated from seawater: Quantitative influence of orthophosphate ions, Geochim. Cosmochim. Acta 50(1986) 2255-2265.

[98] M.A. Nanny, R.A. Minear, J.A.e. Lenheer, Nuclear Magnetic Resonance Spectroscopy in Environmental Science and Technology, Oxford University Press, London, 1997.

[99] Y. Nathan, Mechanism of CO_3^{2-} substitution in carbonate-fluorapatite: Evidence from FTIR spectroscopy, C-13 NMR, and quantum mechanical calculations - Discussion, American Mineralogist 81(1996) 513-514.

[100] D.G.A. Nelson, J.D.B. Featherstone, Preparation, Analysis, and Characterization of Carbonated Apatites, Calcified Tissue International 34(1982) S69-S81.

[101] S.M. Nokhrin, Y. Pan, M.J. Nilges, Electron paramagnetic resonance spectroscopic study of carbonate-bearing fluorapatite: New defect centers and constraints on the incorporation of carbonate ions in apatites, American Mineralogist 91(2006) 1425-1431.

[102] M. Okazaki, F-CO_3^{2-} Interaction in IR-Spectra of Fluoridated CO_3-Apatites, Calcified Tissue International 35(1983) 78-81.

[103] M. Okazaki, Crystallographic Morphology of Heterogeneous Fluoridated Carbonate Apatites, Journal of Dental Research 72(1993) 1285-1290.

[104] D.L. Parkhurst, C.A.J. Appelo, User's guide to PHREEQC (Version 2) – A computer program for speciation, batch-reaction, one-dimensional transport, and inverse

geochemical calculations. , U. S. Geol. Surv. Water Res. Inv. Rept., 1999, pp. 99-4259.

[105] Y.M. Pan, M.E. Fleet, Compositions of the apatite-group minerals: Substitution mechanisms and controlling factors, Phosphates: Geochemical, Geobiological, and Materials Importance 48(2002) 13-49.

[106] S. Peroos, Z.M. Du, N.H. de Leeuw, A computer modelling study of the uptake, structure and distribution of carbonate defects in hydroxy-apatite, Biomaterials 27(2006) 2150-2161.

[107] B.L. Phillips, Y.J. Lee, R.J. Reeder, Organic coprecipitates with calcite: NMR spectroscopic evidence, Environ. Sci. Technol. 39(2005) 4533-4539.

[108] V. Plagnes, C. Causse, G. Dominique, M. Paterne, D. Blamart, A discontinuous climatic record from 187 to 74 ka from a speleothem of the Clamouse Cave (south of France), Earth Planet. Sci. Lett. 201(2002) 87-103.

[109] L.J. Plant, W.A. House, Precipitation of calcite in the presence of inorganic phosphate, Colloids Surf., A 203(2002) 143-153.

[110] D. Prochnow, A.R. Grimmer, D. Freude, Solid-state NMR studies of ^{17}O-enriched pyrophosphates, Solid State Nucl. Magn. Reson. 30(2006) 69-74.

[111] R.J. Reeder, M. Nugent, G.M. Lamble, C.D. Tait, D.E. Morris, Uranyl incorporation into calcite and aragonite: XAFS and luminescence studies, Environ. Sci. Technol. 34(2000) 638-644.

[112] M.M. Reddy, Crystallization of calcium carbonate in presence of trace concentrations of phosphorus containing anions. 1. Inhibition by phosphate and glycerophosphate ions at pH 8.8 and 25ºC, J. Cryst. Growth 41(1977) 287-295.

[113] P. Regnier, A.C. Lasaga, R.A. Berner, O.H. Han, K.W. Zilm, Mechanism of $(CO_3)^{2-}$ Substitution in Carbonate-Fluorapatite - Evidence from FTIR Spectroscopy, ^{13}C NMR, and Quantum-Mechanical Calculations, American Mineralogist 79(1994) 809-818.

[114] J.D. Rimstidt, A. Balog, J. Webb, Distribution of trace elements between carbonate minerals and aqueous solutions, Geochim. Cosmochim. Acta 62(1998) 1851-1863.

[115] M.S. Roberts, P.L. Smart, A. Baker, Annual trace element variations in a Holocene speleothem, Earth Planet. Sci. Lett. 154(1998) 237-246.

[116] W.P. Rothwell, J.S. Waugh, J.P. Yesinowski, High-resolution variable-temperature ^{31}P NMR of solid calcium phosphates, J. Am. Chem. Soc. 102(1980) 2637-2643.

[117] E.B. Sandell, M.H. Hey, D. McConnell, The Composition of Francolite, Mineralogical Magazine 25(1939) 395-401.

[118] A.T. Sanger, W.F. Kuhs, Structural Disorder in Hydroxyapatite, Zeitschrift Fur Kristallographie 199(1992) 123-148.

[119] J.D. Schuffert, M. Kastner, G. Emanuele, R.A. Jahnke, Carbonate-Ion Substitution in Francolite - a New Equation, Geochimica Et Cosmochimica Acta 54(1990) 2323-2328.

[120] P.J. Sideris, U.G. Nielsen, Z.H. Gan, C.P. Grey, Mg/Al ordering in layered double hydroxides revealed by multinuclear NMR spectroscopy, Science 321(2008) 113-117.

[121] D.J. Sinclair, M.J. Risk, A numerical model of trace-element coprecipitation in a physicochemical calcification system: Application to coral biomineralization and trace-element 'vital effects', Geochim. Cosmochim. Acta 70(2006) 3855-3868.

[122] J.C. Stormer, M.L. Pierson, R.C. Tacker, Variation of F-X-Ray and Cl-X-Ray Intensity Due to Anisotropic Diffusion in Apatite during Electron-Microprobe Analysis, American Mineralogist 78(1993) 641-648.

[123] W. Strojek, H. Eckert, Medium-range order in sodium phosphate glasses: A quantitative rotational echo double resonance solid state NMR study, Physical Chemistry Chemical Physics 8(2006) 2276-2285.

[124] D. Stueber, A.M. Orendt, J.C. Facelli, R.W. Parry, D.M. Grant, Carbonates, thiocarbonates, and the corresponding monoalkyl derivatives: III. The C-13 chemical shift tensors in potassium carbonate, bicarbonate and related monomethyl derivatives, Solid State Nuclear Magnetic Resonance 22(2002) 29-49.

[125] W. Stumm, L. Sigg, B. Sulzberger, Chemistry of the solid-water interface : processes at the mineral-water and particle-water interface in natural systems, Wiley, New York, 1992, x, 428 p. pp.

[126] Y. Suetsugu, I. Shimoya, J. Tanaka, Configuration of carbonate ions in apatite structure determined by polarized infrared spectroscopy, Journal of the American Ceramic Society 81(1998) 746-748.

[127] A. Teleman, P. Richard, M. Toivari, M. Penttilla, Identification and quantitation of phosphorus metabolites in yeast neutral pH extracts by nuclear magnetic resonance spectroscopy, Anal. Biochem. 272(1999) 71-79.

[128] A.J. Tesoriero, J.F. Pankow, Solid solution partitioning of Sr^{2+}, Ba^{2+}, and Cd^{2+} to calcite, Geochim. Cosmochim. Acta 60(1996) 1053-1063.

[129] P.C. Treble, J. Chappell, J.M.G. Shelley, Complex speleothem growth processes revealed by trace element mapping and scanning electron microscopy of annual layers, Geochim. Cosmochim. Acta 69(2005) 4855-4863.

[130] J. Tropp, N.C. Blumenthal, J.S. Waugh, Phosphorus NMR study of solid amorphous calcium phosphate, J. Am. Chem. Soc. 105(1983) 22-26.

[131] Y.H. Tseng, Y. Mou, P.H. Chen, T.W.T. Tsai, C.I. Hsieh, C.Y. Mou, J.C.C. Chan, Solid-state P-31NMR study of the formation of hydroxyapatite in the presence of glutaric acid, Magnetic Resonance in Chemistry 46(2008) 330-334.

[132] Y.H. Tseng, J.H. Zhan, K.S.K. Lin, C.Y. Mou, J.C.C. Chan, High resolution ^{31}P NMR study of octacalcium phosphate, Solid State Nucl. Magn. Reson. 26(2004) 99-104.

[133] M. Veshtort, R.G. Griffin, SPINEVOLUTION: A powerful tool for the simulation of solid and liquid state NMR experiments, J. Magn. Reson. 178(2006) 248-282.

[134] J. Vogel, C. Russel, G. Gunther, P. Hartmann, F. Vizethum, N. Bergner, Characterization of plasma-sprayed hydroxyapatite by ^{31}P-MAS-NMR and the effect of subsequent annealing, J. Mater. Sci.: Mater. Med. 7(1996) 495-499.

[135] E.B. Watson, A conceptual model for near-surface kinetic controls on the trace-element and stable isotope composition of abiogenic calcite crystals, Geochim. Cosmochim. Acta 68(2004) 1473-1488.

[136] B. Wopenka, J.D. Pasteris, A mineralogical perspective on the apatite in bone, Materials Science & Engineering C-Biomimetic and Supramolecular Systems 25(2005) 131-143.

[137] R.M. Wilson, S.E.P. Dowker, J.C. Elliott, Rietveld refinements and spectroscopic structural studies of a Na-free carbonate apatite made by hydrolysis of monetite, Biomaterials 27(2006) 4682-4692.

[138] R.M. Wilson, J.C. Elliott, S.E.P. Dowker, R.I. Smith, Rietveld structure refinement of precipitated carbonate apatite using neutron diffraction data, Biomaterials 25(2004) 2205-2213.

[139] J. Wright, K.R. Rice, B. Murphy, J. Conca, PIMS Using Apatite II^{TM}: How It Works To Remediate Soil and Water, in: R.E. Hinchee, B. Alleman, (Eds), Sustainable Range Management, Battelle Press, Columbus, OH, 2004.

[140] J.P. Yesinowski, H. Eckert, Hydrogen environments in calcium phosphates: ^{1}H MAS NMR at high spinning speeds, J. Am. Chem. Soc. 109(1987) 6274-6282.

[141] J.P. Yesinowski, H. Eckert, G.R. Rossman, Characterization of hydrous species in minerals by high-speed ^{1}H MAS-NMR, J. Am. Chem. Soc. 110(1988) 1367-1375.

[142] J.P. Yesinowski, M.J. Mobley, ^{19}F MAS-NMR of Fluoridated Hydroxyapatite Surfaces, Journal of the American Chemical Society 105(1983) 6191-6193.

[143] R. Zapanta-Legeros, Effect of Carbonate on Lattice Parameters of Apatite, Nature 206(1965) 403-404.

[144] S.J. Zhong, A. Mucci, Calcite precipitation in seawater using a constant addition technique: A new overall reaction kinetic expression, Geochim. Cosmochim. Acta 57(1993) 1409-1417.